# Development of a methodology to characterize activated carbon involved in gold recovery in ore processing (ULiège)

**Auteur :** Lazar, Benedict
**Promoteur(s) :** Pirard, Eric
**Faculté :** Faculté des Sciences appliquées
**Diplôme :** Master en ingénieur civil des mines et géologue, à finalité spécialisée en "geometallurgy (EMERALD)
**Année académique :** 2024-2025
**URI/URL :** http://hdl.handle.net/2268.2/25043

UNIVERSITÉ DE LIÈGE

FACULTÉ DES SCIENCES APPLIQUÉES

# Development of a Methodology to Characterize Activated Carbon Involved in Gold Recovery in Ore Processing

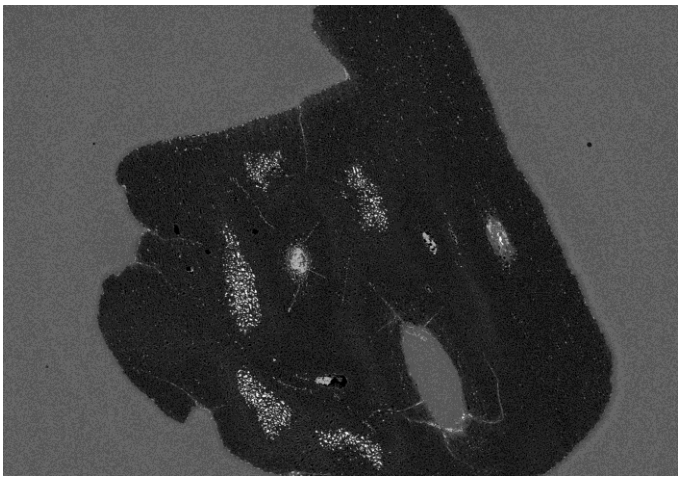

A Master's Thesis submitted by

Benedict Lazar

In Fulfillment of the Requirements for a Master's Degree in

Georesources Engineering

| | |
|---|---|
| Supervisor: | Professor Eric Pirard |
| | Professor Jean-François Boulanger |
| Peer Reviewer: | Professor Jan Rosenkranz |
| | Doctor Hassan Bouzahzah |
| | Doctor Raphaël Mermillod-Blondin |

- August 2025 -

## Acknowledgements

First and foremost, I would like to sincerely thank my supervisor, Professor Eric Pirard, for giving me the opportunity to be part of the EMerald Master's Programme. Without his support, I would not have been able to explore the fascinating world of mineral processing and geometallurgy, nor would I have had the chance to carry out this master's thesis.

I am also deeply grateful for my academic and industrial co-supervisors, Doctor Hassan Bouzahzah and Doctor Raphaël Mermillod-Blondin, for their invaluable guidance and continuous support – both during the laboratory work at ULiège and throughout internship at LaRonde in Canada. Their mentorship, the insightful discussions and hours of additional support were instrumental in bringing this project to its current stage.

I would also like to thank Agnico Eagle Mines Ltd. for providing the opportunity to visit Canada and for welcoming me to the LaRonde mine. I am especially thankful for provision of samples, test materials and the many enriching experiences I gained during those six weeks.

Finally, I would like to thank everyone who contributed their knowledge and time to this project. This includes Jean-Daniel Latour and Hamed Najari for their ongoing support during the internship, as well as Professor Jan Rosenkranz, Professor Jean-François Boulanger and Mahdi Ghobadi for their valuable input and suggestions during our online meetings.

## Abstract

Gold recovery from low-grade ores relies predominantly on cyanidation followed by adsorption onto granular activated carbon (GAC). However, inorganic fouling (IF) of GAC is believed to significantly reduce its gold adsorption capabilities and, consequently, process efficiency. This study presents a methodology to characterize inorganic fouling on activated carbon used in carbon-in-pulp (CIP) and carbon-in-leach (CIL) circuits. A systematic protocol was developed to identify, map and quantify inorganic contaminant phases on GAC at the microscale using scanning electron microscopy-based automated mineralogy (SEM-AM). This approach enables detailed assessment of inorganic fouling content and heterogeneity, while also providing crucial insights into its development and state. Furthermore, it allows for site-specific optimization of GAC regeneration strategies, promoting more sustainable resource use and ultimately contributing to improved gold recovery.

## Table of Contents

## List of Acronyms/Abbreviations

| | |
|---|---|
| AARL | Anglo American Research Laboratory |
| ADR | adsorption-desorption-recovery |
| AW | acid wash |
| BET | Brunauer-Emmett-Teller |
| BSE | backscattered electron |
| CIL | carbon-in-leach |
| CIP | carbon-in-pulp |
| GAC | granular activated carbon |
| ICP-OES | inductively coupled plasma optical emission spectroscopy |
| IF | inorganic fouling |
| MP-AES | microwave plasma-atomic emission spectroscopy |
| OM | optical microscopy |
| PB | polished block |
| PW | process water |
| RMSE | root mean square error |
| SEM-AM | scanning electron microscopy-based automated mineralogy |
| SEM-EDS | scanning electron microscopy coupled with energy-dispersive X-ray spectroscopy |
| SSA | specific surface area |
| TR | thermal regeneration |
| XRF | X-ray fluorescence |

## List of Abbreviations

## List of Tables

## List of Units

| | |
|---|---|
| % | percent |
| $ | dollar |
| ° | degree of angle |
| °C | degree Celsius |
| g | gram |
| kg | kilogram |
| M | mol per litre |
| oz | ounze |
| ppb | parts per billion |
| min | minute |
| h | hour |
| t | ton |
| rpm | revolutions per minute |

# 1. Introduction

## 1.1 Geological and Economic Perspectives on Gold

Since ancient times, the appeal of gold has fascinated humans as a symbol of power and wealth. Today, beyond adorning crowns and decorating dishes, gold is an integral part of technological advancements, its unique properties making it a key component in electronic equipment. As a result of its high atomic number and electron structure it is an excellent electric conductor, resistant to corrosion, malleable and ductile (Corti & Holliday, 2009). Gold represents 5 ppb of the earths crust and primarily occurs as native metal, often alloyed with silver to form the mineral electrum (Au[Ag]) (Marsden & House, 2006). Apart from that, gold occurs associated with characteristic minerals such as pyrite ($FeS_2$), arsenopyrite (FeAsS), pyrrhotite ($Fe_7S_8$), galena (PbS), sphalerite ([Zn,Fe]S), stibnite ($Sb_2S_3$) and chalcopyrite ($CuFeS_2$).

In 2023, global gold production amounted to 3,646.1 t worth approximately $228 USD billion at an average gold price of $1,943.0 USD per ounce (World Gold Council, 2024). Since then, the gold price experienced a drastic increase to $3,400.0 USD per ounce as of august 8$^{th}$ 2025, sparking interest and possibilities in studying mining and processing optimization (Trading Economics, 2025).

## 1.2 Gold Processing Routes and Activated Carbon

Depending on the type of gold ore, processing is primarily done using gravity separation, flotation and/or cyanide leaching, involving various routes and intermediate steps (Figure 1). Globally, around 90 % of gold ore is treated using cyanidation due to its efficiency in extracting gold from low-grade ores (*Tailings and Mine Waste '02*, 2002). Although gold recovery using wood charcoal was already patented by Johnson (1894), this step was primarily done using zinc cementation (Merrill-Crowe Process), in which gold is precipitated through the addition of zinc powder. Since the 1970s and 80s, however, gold recovery via adsorption-desorption-recovery (ADR) circuits using granular activated carbon (GAC) has become the preferred method as a result of advancements in gold elution and carbon regeneration (de Andrade Lima, 2007; Ladeira et al., 1993; Tu et al., 2019). ADR circuits offer better performance for low-grade solutions, are less affected by impurities and variations in process parameters and are often considered more economical due to the use of screening instead of solid-liquid separation (Jordi et al., 1991; Ladeira et al., 1993). Still, the economic feasibility of gold recovery using ADR circuits is highly dependent on the reusability of GAC over multiple cycles. Since the

contamination of GAC with organic and inorganic poisons negatively affects process efficiency and can lead to higher gold losses, understanding their behavior and nature is crucial for gold recovery optimization.

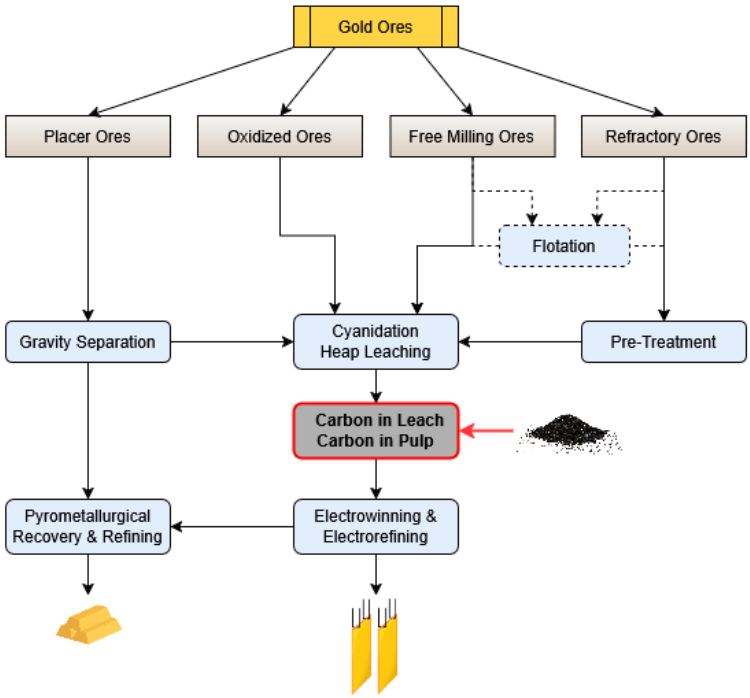


Figure 1. Simplified processing flowsheet for different types of gold-bearing ores. Information adapted from Adams (2005) and Marsden and House (2006). Carbon image adapted from Klipartz (non-commercial license), available at https://www.klipartz.com/en/sticker-png-mroca.

## 1.3 Research Aim, Objectives and Hypotheses

Goal of this study is the development of a methodology to characterize activated carbon involved in gold recovery with the objectives to: (1) design a methodology to identify and characterize inorganic contaminant phases on GAC, (2) quantify the heterogeneity of GAC and establish a minimum sample size for reliable qualitative and quantitative assessment of the inorganic contaminants and (3) evaluate the impact of the contaminants on carbon performance in gold recovery.

It is hypothesized that a combination of techniques exists that can accurately identify inorganic contaminant phases. Moreover, it is believed that inorganic contaminants significantly contribute to carbon heterogeneity and that a minimum sample size exists that enables statistically reliable qualitative and quantitative characterization at a 95 % confidence level. Lastly, it is assumed that the type and quantity of inorganic contaminant directly influences carbon adsorption efficiency of gold and, consequently, gold recovery.

# 2. Literature Review

## 2.1 Activated Carbon

### 2.1.1 Types, Sources and Properties

Whereas various types of activated carbon exist throughout the industry, e.g. powdered, extruded, bead and polymer-coated, GAC is by far the most widely used for gold recovery (Faulkner et al., 1987). Apart from gold recovery, GAC is used for a variety of purposes, e.g. the removal of organic contaminants from industrial effluents and water or the removal of contaminants in gas and gas masks (Rogans, 2017). GAC used for gold recovery commonly varies between 1–3 mm particle size and can be produced from a variety of sources such as bituminous coal, lignite, coconut shells or wood (Gönen et al., 2007). However, according to Faulkner et al. (1987), over 95 % of Au and Ag recovery is achieved using coconut shell GAC due to its superior properties relative to other carbon sources. This includes a high affinity towards gold, large surface area, uniform pore structure, high mechanical strength, good abrasive resistance, suitable density for pulp mixing and good availability (Budi et al., 2014; Ganjoo et al., 2023; Mozammel et al., 2002). In general, the performance of GAC in adsorbing gold is evaluated based on two main factors, i.e., gold loading rate (commonly known as activity) and gold loading capacity. ADR circuits generally operate under conditions favoring gold loading on the carbon far from equilibrium. Consequently, extraction efficiency is primarily based on adsorption kinetics rather than equilibrium limitations, making carbon activity a key process property (Fleming et al., 2011).

### 2.1.2 Pore Structure and Adsorption Sites

GAC production is commonly done via a two-step reaction consisting of carbonization at 600–900 °C, followed by a thermal oxidation at 600–1200 °C, leading to the formation of macro- (> 50 nm), meso- (2–50 nm) and micropores (< 2 nm). The porosity of coconut shell GAC mainly comprises micropores, hence its extended inter-particulate surface area of up to 1300 $m^2 \cdot g^{-1}$ (Heschel & Klose, 1995; Rogans, 2017).

Several authors argue that gold adsorption primarily occurs within micropores, making coconut shell GAC an ideal adsorption medium (Fleming & Nicol, 1984; Cevallos Toledo et al., 2020). Jia et al. (1998), however, noticed a significant improvement in gold adsorption after increasing the total pore volume, while allowing only marginal changes in micropore volume. The authors therefore suggested that micropores may not play a dominant role in aurocyanide adsorption.

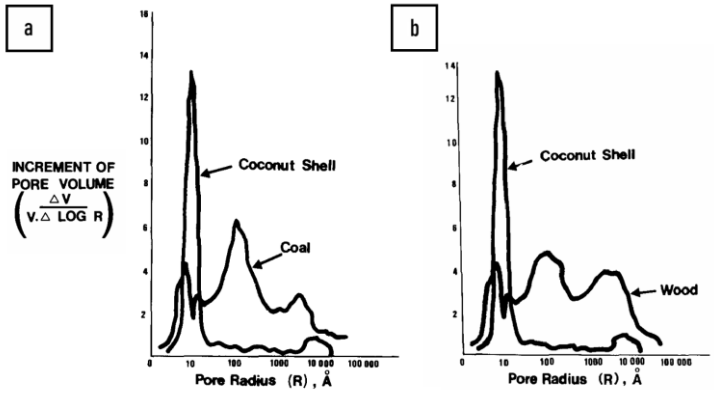


Figure 2. Typical pore size distribution for thermally activated coconut shell carbon including: (a) thermally activated coal-based carbon and (b) chemically activated wood carbon. Source: McDougall (1991).

Yin et al. (2014) observed the formation of $Au(CN)_2^-$ clusters as a result of "aurophilicity", using High Angle Annular Darkfield Scanning Transmission Electron Microscopy. Aurophilicity refers to strong metal-metal interactions between Au (I) atoms of complexes, minimizing distances between the gold molecules. Formation of gold and silver cyanide clusters was also reported by Yin et al. (2011). Xia et al. (2022) argue, that this may limit access of aurocyanide to GAC micropores and recommend a tailored pore size distribution including a high mesoporosity in order to increase gold loading capacity.

According to Jia et al. (1998), adsorption sites of GAC can be divided into two groups, i.e., hydrophobic surfaces of the graphene layers and mostly hydrophilic oxygen and nitrogen functional groups. Several authors reported that graphene layers serve as dominant adsorption sites for gold (Ibrado & Fuerstenau, 1992; Klauber, 1991). The role of functional groups, however, is still being debated. Ghasemi et al. (2022) reported an increased gold adsorption tendency for carboxylic acid (COOH) functional groups and decreased adsorption energy for hydroxyl (OH) functional groups. Moreover, adsorption promotion of oxygen functional groups is thought to be more pronounced for copper cyanide complexes, reducing the carbons selectivity towards gold. Similar observations were made several authors (Ibrado & Fuerstenau, 1992; Ofori-Sarpong et al., 2010; Souza et al., 2014). Nitrogen functional groups were also found to have no significant effect on gold adsorption (Jia et al., 1998).

### 2.1.3 Conditioning

Before using GAC in the adsorption circuit, it is commonly conditioned using wetting and pre-attrition. Wetting of GAC is performed to remove entrapped air and ensure that GAC particles do not float out of up-flow columns or concentrate in upper region of CIP tanks. Using pre-attrition, operating plants remove weak or fractured carbon components and round off sharp

corners via agitated tanks or the carbon reactivation unit. Yamak et al. (2019) observed that most carbon losses occurred during the first 8 h of agitation, concluding that pre-attrition may considerably reduce carbon fines losses during operation and hence decrease the amount of gold lost with the carbon fines.

## 2.2 Cyanidation and Gold Recovery

### 2.2.1 Elsner Reaction and Metal-Cyanide Selectivity

The chemical reactions involved in the dissolution of gold and the formation of the dicyanoaurate (I) anion $Au(CN)_2^-$ (commonly known as aurocyanide [Figure 3]) using cyanidation were first described by Elsner (1846), as follows:

$$4Au + 8CN^- + O_2 + 2H_2O \rightarrow 4Au(CN)_2^- + 4OH^- \quad (1)$$

Bodländer (1896) further reported the formation of hydrogen peroxide as an intermediate product according to Eq. (2) and its importance as oxidizing agent in Eq. (3):

$$2Au + 4CN^- + O_2 + 2H_2O \rightarrow 2Au(CN)_2^- + 2OH^- + H_2O_2 \quad (2)$$

$$2Au + 4CN^- + H_2O_2 \rightarrow 2Au(CN)_2^- + 2OH^- \quad (3)$$

Since cyanidation targets not only gold but also base metals like Cu, Ni, Co, Fe and Zn, the formation of other metal-cyanide complexes is common. It is widely recognized that GAC exhibits a preference in the adsorption of metal-cyanide complexes, which, according to Marsden & House (2006), follows the order:

$$Au(CN)_2^- > Hg(CN)_2^0 > Ag(CN)_2^- > Cu(CN)_3^{2-} > Zn(CN)_4^{2-} > Ni(CN)_4^{2-} \gg Fe(CN)_6^{4-}$$

Studies conducted by Yin et al. (2011) and Ghasemi et al. (2018) observed a strong relation between the hydration number of a metal-cyanide complex and its adsorption onto GAC. The authors argued that an increase in complex diameter, as a result of increased hydration, hinders the complex from entering micropores. Due to its lower degree of hydration, GAC shows a

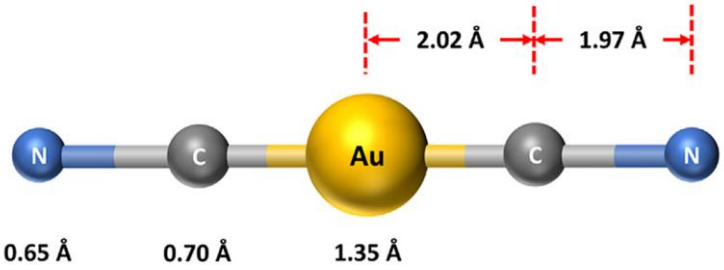


Figure 3. Atomic structure of the aurocyanide anion. Source: Xia et al. (2022).

higher selectivity towards adsorbing the aurocyanide complex over other metal-cyanide anions. Nevertheless, the presence of co-existing metal-cyanide complexes inevitably leads to competition for active sites on the GAC surface and thus influences adsorption efficiency.

### 2.2.2 Carbon-in-Leach vs. Carbon-in-Pulp

ADR circuits use the adsorption of $Au(CN)_2^-$ onto adsorbents like GAC or ion exchange resins in order to separate the aurocyanide complex from the pregnant leach solution. Adsorption typically takes place in large, agitated tanks, serving as the heart of the carbon-in-leach (CIL) or carbon-in-pulp (CIP) processes. Whereas adsorption occurs simultaneously with leaching in the former, these processes happen in separate tanks in the latter. During both processes, GAC is transferred in counter-current flow with the pulp, ensuring a consistently high concentration gradient of gold between the GAC and the pulp (Fleming et al., 2011).

CIL is primarily used for preg-robbing ores. Preg-robbing refers to the removal of aurocyanide by ore constituents, e.g., carbonaceous matter, minerals or other impurities such as elemental carbon, decreasing overall gold recovery (Rees & van Deventer, 2000a). The use of CIL circuits for preg-robbing ores results from the fact that aurocyanide adsorbs more selectively onto GAC when competing with preg-robbing ore constituents (Rees & van Deventer, 2000b). Apart from its ability to mitigate preg-robbing, CIL further requires lower capital costs and has a smaller footprint compared to CIP. Nevertheless, according to Nicol et al. (1984), the contact of GAC with abrasive ore particles leads to higher GAC losses and requires a greater GAC inventory for CIL. While demanding higher capital costs and a larger footprint, CIP circuits, on the other hand, allow for higher gold loading on the GAC and enhanced recovery (Yamak et al., 2019).

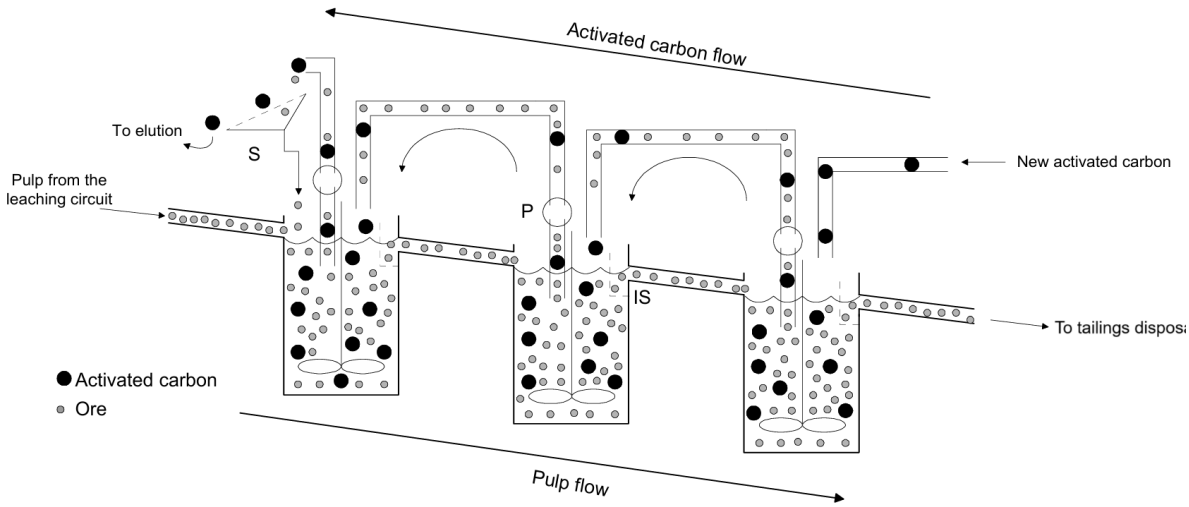


Figure 4. Schematic representation of the counter-current flow of activated carbon and pulp in the adsorption tanks including interstage screens (IS), carbon transfer pumps (P) and the loaded carbon screen (S) at the exit of the last adsorption tank. Source: de Andrade Lima (2007).

### 2.2.3 Adsorption Mechanisms

Whereas the actual adsorption mechanism is still not fully understood, several theories exist with the most prominent ones being the electrostatic attraction theory, ion-pair theory (Adams, 1989; G. McDougall et al., 1981) and the non-ion pair theory (Ibrado & Fuerstenau, 1995).

According to the electrostatic attraction theory, aurocyanide adsorbs at least partially irreversibly onto highly active, polar surface sites as an unpaired $Au(CN)_2^-$ anion (Lagerge et al., 1999). Based on the adsorption sites presented by Jia et al. (1998), the authors proposed two main possibilities of adsorption, i.e., ion exchange mechanisms with functional groups and interaction between p orbitals of the graphene layers and $Au(CN)_2^-$ anions. Using X-ray photoelectron and infrared spectroscopy, Ibrado & Fuerstenau (1995) observed a weak donation of π-electrons from the π orbitals of GAC to gold, suggesting adsorption of the unpaired $Au(CN)_2^-$ complex without chemical change. The authors further stated that they did not find evidence supporting the ion-pair adsorption theory.

However, in the presence of $Ca^{2+}$ and $Mg^{2+}$ and absence of free $CN^-$, Smith et al. (1984) observed an improve in kinetic activity of GAC. Similar findings were reported by Davidson (1974), who first referred to them as "spectator" cations. Fleming and Nicol (1984) observed that higher ionic strength increased both gold adsorption rate and loading capacity, with a much greater effect on the capacity compared to the rate. Conversely, a high cation concentration during elution suppressed aurocyanide desorption, slowing down the diffusion of gold from the GAC surface into the eluant solution (Davidson, 1974; van Deventer & van der Merwe, 1994). These cations enhance gold adsorption due to the formation of $M^{n+}[Au(CN)_2^-]_n$ ion pairs, which adsorb onto less active sites of the carbon through van der Waals forces (Lagerge et al., 1999). Accordingly, the stability of aurocyanide complexes is highest with calcium, while the adsorption onto GAC follows the series:

$$Ca^{2+} > Mg^{2+} > H^+ > Li^+ > Na^+ > K^+$$

While exact mechanisms strongly depend on process conditions, the proposed theories are not necessarily mutually exclusive and the topic is still debated among scientists (Tsuchida & Muir, 1986).

### 2.2.4 Diffusion Controls

In general, three diffusion mechanisms are believed to control adsorption kinetics of aurocyanide onto GAC, i.e., film diffusion, pore diffusion and surface diffusion (Fleming et al., 1984; Jones et al., 1989; Le Roux, 1991).

Film diffusion describes the mass transport of aurocyanide from the bulk solution phase across a hydrodynamic boundary layer surrounding the GAC. Diffusion into and filling of the carbon pores is described by the pore diffusion mechanism. Finally, via surface diffusion, the molecules migrate into the internal GAC structure along internal pore walls.

Aurocyanide adsorption onto GAC is characterized by an initial high adsorption rate controlled by film diffusion at low gold loadings until reaching a pseudo-equilibrium. This is followed by a slow surface diffusion at higher gold loadings (Ahmed et al., 1992; Fleming & Nicol, 1984; Ibragimova et al., 2014; La Brooy et al., 1986; Nicol et al., 1987). Using X-ray computed microtomography, Pleysier et al. (2008) observed that gold was predominantly adsorbed at the external carbon surface at 2,500 $mg \cdot kg^{-1}$ gold loading on carbon. Similar observations were made by La Brooy et al. (1986). Pleysier et al. (2008) attributed this initial adsorption to readily accessible adsorption sites such as macro- and possibly mesopores. However, at this level of gold loading, the authors observed that gold had already diffused into the internal part of the carbon, indicating a shift toward surface diffusion. As readily accessible active sites became saturated, the adsorption rate decreased and gold diffused deeper into the internal carbon structure, as observed at a higher gold loading of 25,000 $mg \cdot kg^{-1}$ (Figure 5). The contribution of pore diffusion to the overall gold loading was considered insignificant, as gold did not accumulate around macropores but displayed an even distribution.

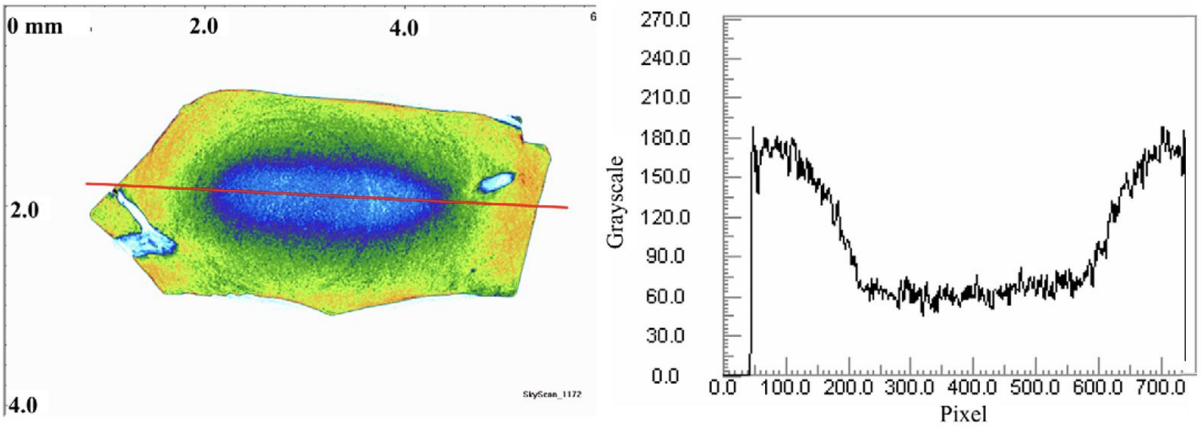


Figure 5. Microtomography image (left) and grayscale density map (right, x-axis scale: 1 pixel = 5.15 µm) of carbon loaded with 25,000 $mg \cdot kg^{-1}$ gold after 24 h. Source: Pleysier et al. (2008).

### 2.2.5 Elution and Refining

Following adsorption, the loaded GAC is removed from the circuit, separated from the slurry and transferred into the elution column. In the elution column, gold is stripped from GAC at high temperature producing a pregnant solution. Common elution methods are the Zadra and

the Anglo American Research Laboratory (AARL) elution process. Both processes rely on the addition of sodium cyanide (NaCN) and sodium hydroxide (NaOH) at varying concentrations, promoting the replacement of the $Au(CN)_2^-$ complex from the GAC surface by free cyanide ($CN^-$) and $OH^-$ (van Deventer & van der Merwe, 1994). The key difference between both processes lies in the AARL carbon pre-treatment, which is done using a hot caustic cyanide solution followed by elution using hot de-ionized water.

The resulting pregnant solution is further treated in the electrowinning plant, where an electric current is passed causing the gold to plate onto metal cathodes. The cathodes are then smelted to produce doré bars.

## 2.3 Carbon Fouling

### 2.3.1 Organic and Inorganic Fouling

Despite the selectivity of GAC regarding metal-cyanide speciation, it exhibits an unselective behavior in other respects, adsorbing most of the dissolved inorganic and organic compounds present in the leach solution (Fisher & Dunn, 2000). The accumulation of these compounds on the GAC is commonly referred to as carbon "fouling".

Organic foulants primarily include flotation reagents, oils, kerosene and surfactants, while inorganic foulants mostly depict salts, base metal precipitations and fine minerals such as silica ($SiO_2$), complex silicates, aluminates and iron particles (Marsden & House, 2006). Although both fouling mechanisms are believed to affect the adsorption process, this work will focus on the inorganic fouling (IF) of GAC.

### 2.3.2 Inorganic Fouling Mechanisms

It is widely recognized that IF affects the GAC in several ways: (1) blockage of meso- and macropores, key pathways for aurocyanide to the adsorption sites, by physically trapped solids or precipitates (Macrae et al., 1988; Rogans, 2017; Smith et al., 1984; Stange, 1999; Urbanic et al., 1985); (2) precipitation of inorganic salts on the GAC surface, blocking active sites (Macrae et al., 1988; Marsden & House, 2006); and (3) direct adsorption of inorganic species, taking up active sites (Marsden & House, 2006).

Macrae et al. (1988) observed minerals particles being wedged in cracks and pores of the GAC, however, the majority was cemented in place by calcite ($CaCO_3$). Interestingly, gold and calcite exhibited similar distribution patterns within the GAC particles, which led the authors to propose that both transport through the carbon porosity occurred in solution and that gold

adsorption takes place while calcite is precipitated. Comparing coconut shell and extruded peat carbons, they observed significantly less calcite inside extruded peat carbon particle compared to its surface, whereas in the coconut shell carbon calcite was distributed throughout the entire particle. This observation was attributed to the lower porosity of extruded peat carbons. The authors further suggested that the precipitation of salts does not occur preferentially on GAC but on any solid present in the pulp.

Rogans (2017) described the occlusion of colloidal materials by scale or their adsorption onto the outer surface of GAC, blocking meso- and macropores. According to the author, these colloids include hematite ($Fe_2O_3$), goethite (FeO(OH)), prussian blue (ferric ferrocyanides) and different forms of silica such as shale and clay.

Juhola (1973) observed an increase in ash content over multiple adsorption-regeneration cycles of carbon used in wastewater treatment. The ash content refers to the mineral oxide content of GAC, which is primarily made up of silicon and aluminum. Higher ash content decreases carbon activity and reactivation effectiveness, partially resulting from the catalytic oxidation of the carbons basic structure. High levels of calcium carbonate and magnesium carbonate ($MgCO_3$) were also attributed to repeated recycling and excessive residence times in the study of Smith et al. (1984). Rogans (2017), on the other hand, stated that the scale formation does not necessarily increase with each adsorption cycle, as it is not an equilibrium adsorption process. Moreover, it depends on the "scaling index" conditions of the solution, e.g., pH, temperature and Ca concentration. According to Davidson et al. (1979), lowering of the solution pH to 8–9 considerably reduced calcite fouling. However, this approach is not viable in practice since a lower pH favors the formation of highly toxic hydrogen cyanide (HCN).

### 2.3.3 Key Inorganic Species

In a study by Smith et al. (1984), the authors observed the formation of $CaCO_3$, $MgCO_3$ as well as a gelatinous silica film. Using scanning electron microscopy coupled with energy-dispersive X-ray spectroscopy (SEM-EDS), they identified calcite as numerous crystals erupting from the carbon surface (Figure 6b). Presumably, when treated in a regeneration kiln, dissolved calcite within carbon pores was transported outward by escaping water and steam and recrystallized at the pore exit.

Macrae et al. (1988) performed a qualitative characterization of IF on coconut shell GAC and extruded peat carbons using a Cambridge S100 stereoscan SEM fitted with an EDS system. By producing sections, the authors examined not only the external but also the internal surfaces of

the carbon and identified calcite as the main contaminant in both regions. Calcite was found filling cracks and pores and covering GAC particle surfaces as either amorphous-like coatings or finely crystalline material (Figure 7). IF on external surfaces consisted of a wide variety of minerals, with calcite, silica, hematite and clay minerals being the most abundant. On the internal surfaces, however, only calcite was identified, except for few individual quartz, arsenopyrite, hematite and clay particles found trapped in larger pores and holes. The authors did not observe calcite in the form reported by Smith et al. (1984).

Several other authors also reported $CaCO_3$ as key inorganic contaminant making up the majority of the IF (Cevallos Toledo et al., 2020; Rogans, 2017). Calcium is introduced due to the use of quicklime (CaO) and slaked lime ($Ca(OH)_2$) as pH controller but can also arise from soluble ore constituents (e.g., limestone ($CaCO_3$), dolomite ($CaMg(CO_3)_2$)). Calcite formation further requires the presence of carbonate ions ($CO_3^{2-}$), which are believed to originate from the dissolution and dissociation of atmospheric carbon dioxide ($CO_2$) into $CO_3^{2-}$ as well as the catalytic oxidation of $CN^-$ at the carbon surface. The oxidation reaction yields ammonia ($NH_3$) and bicarbonate ($HCO_3^-$), which further reacts with $Ca^{2+}$ according to Eq. (4)–(6) as reported by Smith et al. (1984) and van Vliet (1991):

$$CN^- + \frac{1}{2} O_2 \rightleftharpoons CNO^- \quad (4)$$

$$CNO^- + 2\, H_2O \rightleftharpoons NH_3 + HCO_3^- \quad (5)$$

$$CO_3^{2-} + Ca^{2+} \rightarrow CaCO_3 \quad (6)$$

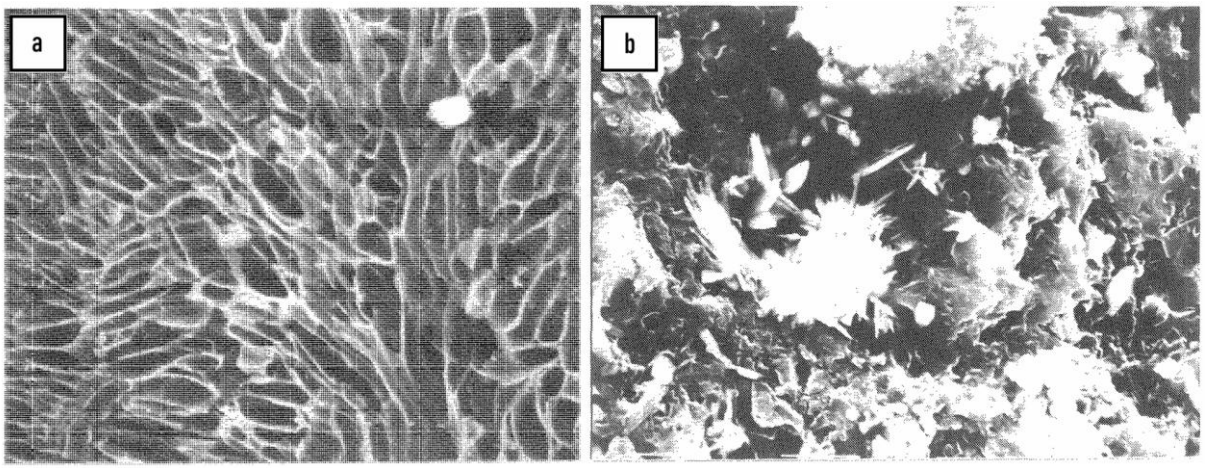


Figure 6. SEM-EDS images of: (a) Kintal activated coconut carbon containing a presumed silica particle (top right; magnification: ×320) and (b) peat pellets activated carbon with presumed $CaCO_3$ crystals (magnification: ×1250). Abbreviation: SEM-EDS = scanning electron microscopy coupled with energy-dispersive X-ray spectroscopy. Source: Smith et al. (1984).

Via similar mechanisms, calcium sulfate ($CaSO_4$) and magnesium scales can form, however, to a lesser extent (Rogans, 2017). Macrae et al. (1988) suggest that a thin calcite film may form through these reactions, but the thick calcite layers observed in their study likely resulted from continued growt.h at sites where calcite formation was initiated.

Smith et al. (1984) reported improved carbon performance when $Ca(OH)_2$ was replaced by soda ash ($Na_2CO_3$) and pH was decreased from 10 to 8. While Rogans (2017) argues that a higher pH stabilizes anions present in the solution, favoring the reactions in Eq. (4)–(6), Smith et al. (1984) attributed the improvement to losses in free $CN^-$ at lower pH.

As a result of higher residence times, free $CN^-$ concentrations and pH, Smith et al. (1984) assumed that carbon fouling occurs to a greater extent in CIL compared to CIP circuits.

### 2.3.4 Impact on Adsorption

Scientists generally agree on OF being the major factor over IF in preventing gold loading, decreasing both the loading rate and capacity, although the extend of its impact on the latter is still being debated (Fleming & Nicol, 1984; La Brooy et al., 1986; Petersen & van Deventer, 1991; Pleysier et al., 2008; Salarirad & Behnamfard, 2010, 2011). Thus, few studies exist that directly investigate the impact of IF on GAC performance in a gold processing circuit.

Marsden & House (2006) stated that the "buildup of organic and inorganic substances on carbon [...] results in a decrease in the kinetics and equilibrium loading of gold" without differentiating the effects of different fouling types. Smith et al. (1984) noted a decrease in the adsorption rate, which was attributed to micro- and macropore blocking by the precipitated material. Crystal deposition on the carbon surface, however, did not severely affect the activity of thermally

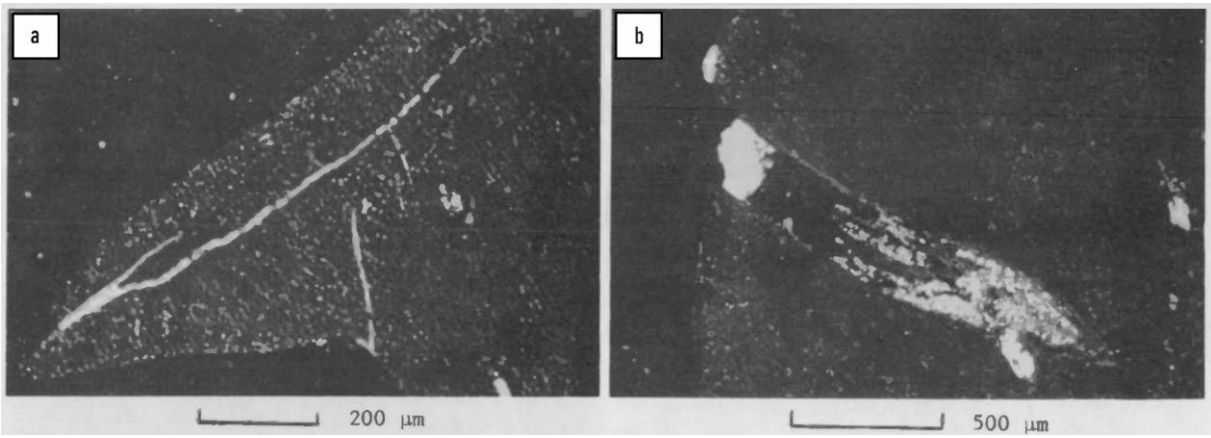


Figure 7. Coconut shell activated carbon (Calgon GRC-22) showing: (a) calcite filling cracks and pores; (b) calcite blocking the entrance of a macropore, filled with clay and hematite at the bottom of the pore. Source: Macrae et al. (1988).

reactivated carbon. Davidson & Schmidt (1986), on the other hand, reported that carbon surface passivation by calcite could result in decreased gold adsorption. Davidson and Sole (2007) stated that calcium loadings below 20 $kg \cdot t^{-1}$ carbon have minimal impact on carbon kinetics, whereas loadings of 40–60 $kg \cdot t^{-1}$ considerably reduce gold adsorption.

With an increase in ash content, Juhola (1973) observed a reduction in adsorptive capacity of carbon used in wastewater treatment due to the catalytic oxidation of the carbon's basic structure. According to van Vliet (1991), micropores become more congested than meso- and macropores by inorganic adsorbates during wastewater treatment. Although unrelated to gold adsorption, a similar effect in CIP/CIL processing could considerably impact adsorption efficiency due to the importance of micropores. Furthermore, by potentially blocking eluant access during elution, IF may adversely affect desorption efficiency (Marsden & House, 2006). Additionally, Macrae et al. (1988) observed preferential breakage of GAC particles along calcite coatings, suggesting reduced carbon strength and increased mechanical degradation, which indirectly influences gold recovery.

## 2.4 Carbon Replacement and Reactivation

### 2.4.1 Carbon Make-up

With respect to environmental and economic considerations, the GAC is removed from the elution column and recycled to be reused possibly over 100 times before leaving the circuit (Fisher & Dunn, 2000; „Gold Recovery", n.d.). The primary route of carbon loss is mechanical degradation as a result of fracturing, abrasion and attrition. Consequently, GAC particles break down into fines, which can bypass carbon screens until they are captured by carbon safety screens (McDougall, 1991). Since these lost carbon fines often remain loaded with gold, they are typically recovered, stockpiled and ashed to recover the gold from the resulting ash (Lin et al., 2003). To offset these carbon losses, companies periodically replenish the circuit with fresh, virgin carbon.

### 2.4.2 Thermal Regeneration

Several procedures exist to reactivate GAC, e.g., acid wash (AW), thermal regeneration (TR), treatment using supercritical fluids, electrochemical processes and microwave reactivation. Removal of the buildup of IF and OF is commonly done via a combination of AW and TR, respectively (Cevallos Toledo et al., 2020).

TR depicts one of the oldest and most established techniques for GAC reactivation, removing volatile or unstable organic impurities (Fisher & Dunn, 2000; Ganjoo et al., 2023). In a multi-zone heating kiln, GAC is typically subjected to steam-controlled selective oxidation, vaporizing organic contaminants, creating new pores and regenerating surface-active sites (Cevallos Toledo et al., 2020). The number of zones in the kiln can vary but generally consist of a drying (100–200 °C), a low-temperature (up to 550 °C) and a high-temperature (up to 750 °C) zone. The subsequent steps involve removing excess moisture, burning off volatile organic compounds in an oxygen-controlled atmosphere and lastly pyrolyzing non-volatile impurities under a non-oxidizing atmosphere (Department of Education, Science and Training, Australia, 2005). Inorganics present during TR, such as Ca, Mg and Fe, are known to catalyze the steam-carbon reaction. Accordingly, they accelerate the gasification of not only pyrolyzed adsorbate residues but also base carbon and can soften its matrix (Harriott & Cheng, 1988; Prodan et al., 1988; van Vliet, 1991). Thus, in order to minimize carbon losses and maintain its hardness, Davidson and Tumility (1985) suggested to perform AW prior to TR, effectively removing the IF before sending carbon to the kiln.

Following TR, the carbon can be cooled using tube cooling, air cooling or water quenching. Urbanic et al. (1985) emphasize the use of water quenching over air cooling due to enhanced adsorption rate regeneration. Furthermore, water quenching serves as an effective method for pre-wetting the carbon before returning it to the circuit (Faulkner et al., 1987). However, if the quench water contains high levels of dissolved solids, carbon activity can be significantly reduced as impurities adsorb onto the regenerated carbon surface, effectively blocking its pores. Faulkner et al. (1987) raised similar concerns and suggested the use of clean water with low ionic strength to preserve carbon activity.

### 2.4.3 Acid Washing

AW is the chemical treatment of GAC using dilute acids like hydrochloric acid (HCl) or nitric acid ($HNO_3$), resulting in the removal of inorganic contaminants (Marsden & House, 2006). Acid strength typically varies between 3–10 % for HCl and 3.5–5 % for $HNO_3$, depending on the IF degree and washing temperature (Marsden & House, 2006; Stange, 1999; Urbanic et al., 1985). In general, AW is performed at temperatures ranging from ambient up to 90 °C (Stange, 1999).

While researchers agree that higher temperatures accelerate IF removal, Adams (1989) suggested the partial decomposition of adsorbed $Au(CN)_2^-$ into AuCN as a result of increased heating in strongly acidic conditions. AuCN is an insoluble, polymeric species that adsorbs onto

GAC considerably less reversibly compared to $Au(CN)_2^-$. Using SEM, Adams (1989) also noticed the formation of $Au^{(0)}$ after high-temperature AW and elution (Figure 8). Under typical CIP loading conditions no AuCN formation was observed. Interestingly, neither AuCN nor gold metal particles were detected on the carbon surface following AW alone. Thus, the author suggested that the alkaline conditions of the hot NaOH solution led to the decomposition of AuCN according to:

$$2\ AuCN + \ e^- \rightleftharpoons Au^0 + Au(CN)_2^- \tag{7}$$

Similarly, van Deventer and van der Merwe (1993) argue that the ratio of occurrence of AuCN to $Au(CN)_2^-$ on the carbon in the elution column is depending on the GAC type and AW conditions. At conditions of low pH and high temperature, the authors observed the reduction of both $Au(CN)_2^-$ and AuCN to metallic gold $Au^{(0)}$. Since AuCN and $Au^{(0)}$ do not take part in the equilibrium reaction between aurocyanide on the carbon and in the solution, this decomposition reduces desorption efficiency during elution and requires more $CN^-$ for reconversion to $Au(CN)_2^-$ (Adams, 1989; Cook et al., 1989; Tsuchida & Muir, 1986; van Deventer & van der Merwe, 1993).

Thus, although higher temperatures increase IF removal, less severe AW conditions favor the presence of $Au(CN)_2^-$ and consequently the performance of downstream processes like elution (van Deventer & van der Merwe, 1994).

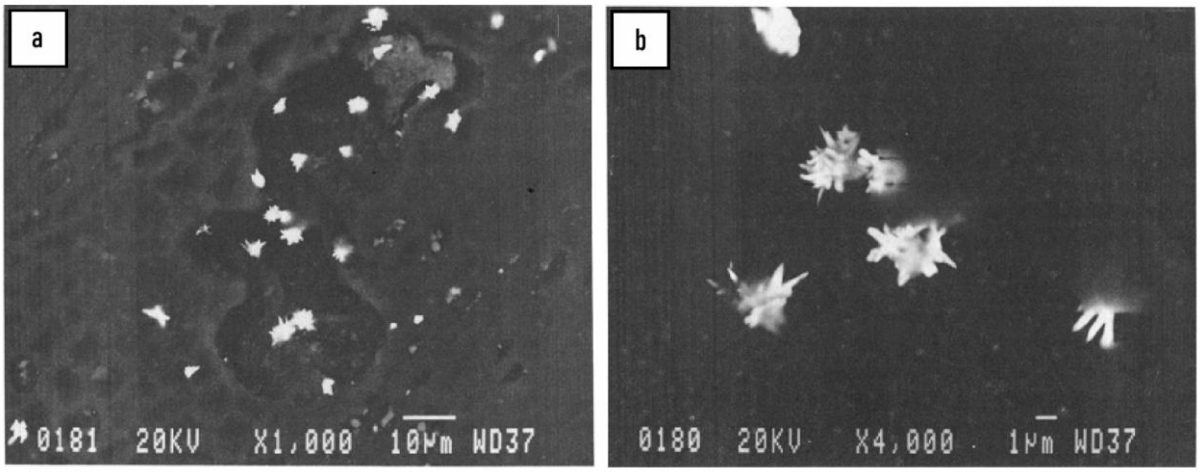


Figure 8. SEM micrographs showing: (a) crystalline gold metal particles in a macropore and (b) their dendritic structure in a magnified version of (a), after 30 min washing using 4 % HCl at 95 °C and elution using 0.1 M NaOH at 90 °C. Abbreviations: SEM = scanning electron microscopy. Source: Adams (1989).

Using acids, precipitated salts and other IF's can be dissolved and subsequently rinsed from the carbon according to:

$$MCO_3 + 2\,H^+ \rightleftharpoons M^{2+} + CO_2 + H_2O \quad (8)$$

The type of acid used determines the salt produced from $CaCO_3$ and thus the product's solubility, e.g., calcium chloride ($CaCl_2$) for HCl and calcium nitrate $Ca(NO_3)_2$ for $HNO_3$ (Rogans, 2017).

Marsden and House (2006) stated that at calcium loadings > 2 %, increasing the HCl concentration from 5 % to 7.5 % significantly improved calcium removal, whereas only a minor effect was observed at loadings < 1 %. The authors further emphasized the importance of thorough carbon-acid mixing during AW as well as a sufficiently long residence time, since dissolution of calcium salts within carbon pores depicts a diffusion-controlled mechanism. Using HCl, around 80–95 % Ca can be removed from the carbon, whereas sodium and magnesium salts are removed less efficiently (< 80 %) but also occur to a lesser extent. Moreover, HCl removes up to 50 % of Ni, Zn, Fe and Si from the carbon but does not affect Ag, Hg and Cu loadings.

In a study on coconut shell GAC, Macrae et al. (1988) found that the external surfaces of regularly acid-washed carbon were much cleaner of IF compared to unwashed carbon, but still heavily contaminated by calcite. Calcite and other minerals could be seen as individual grains inside the carbon porosity. Smith et al. (1984) observed that AW of coconut shell GAC with 5 % HCl increased carbon adsorption rate from < 100 $h^{-1}$ to 150 $h^{-1}$ prior to TR. However, even at higher concentrations of 10 % HCl, very little silica was removed. Treatment of the carbon with a mixture of 5 % hydrofluoric acid (HF) and 10 % HCl at 60–70 °C for 1 h significantly enhanced silica removal, with near-complete removal for some carbon compositions. However, improvement in carbon activity was only little and lower compared to pure HCl washing, suggesting potential deactivation effects caused by HF. Davidson and Tumility (1985) reported that the partial removal of silica using hot acid (90 °C) helps prevent the formation of refractory crystalline or sintered silicates on the surface of the carbon during TR.

A challenge associated with the use of HCl during AW prior to TR is the deposition of residual chlorides within the GAC pores (Marsden & House, 2006). If not removed through rinsing and neutralizing steps using water and sodium hydroxide, chlorides can cause major problems due to their high corrosiveness and release during TR. Likewise, if AW is performed prior to carbon elution, the release of chloride ions may affect the elution circuit, albeit to a lesser extent. Apart

from removing chlorides, rinsing and neutralization steps may also help in the removal of reprecipitated salts.

Cevallos Toledo et al. (2020) reported that calcium removal was highest (77 %) using 20 % $HNO_3$ at 50 °C for 30 min, which was attributed to the high solubility of $Ca(NO_3)_2$. Furthermore, the use of $HNO_3$ eliminates the risk of residual chlorides, however, it may deteriorate GAC through oxidation and deactivation of the carbon surface, even at concentrations below 5 % (Marsden & House, 2006). In a study by Demiral et al. (2021), increasing $HNO_3$ concentrations from 15 % to 69 % decreased the Brunauer-Emmett-Teller (BET) surface area of the carbon from 1399 $m^2 \cdot g^{-1}$ to 15.44 $m^2 \cdot g^{-1}$, clogged micropores and decreased the mesopore volume. Additionally, $HNO_3$ washing can increase the loss of silver from the GAC (Marsden & House, 2006).

Faulkner et al. (1987) reported that AW was successfully reduced the ash content of all carbons tested, improving the adsorption rate in four out of five cases. Similar findings were reported by Urbanic et al. (1985), who observed reductions in ash content for both HCl and $HNO_3$, along with slight improvements in the adsorption rate of the carbon. The authors concluded that both acids were equally efficient for AW of GAC.

AW not only removes impurities, but also introduces hydrophilic functional groups and increases the surface area by improving pore accessibility (Bouleghlimat et al., 2013). After treating GAC with $HNO_3$, Park et al. (2007) noticed a fourfold increase in acidity, a twelvefold increase in lactone groups and an enormous increase in oxygen-containing functional groups. While this enhanced copper adsorption, it may decrease the selectivity of GAC towards adsorbing gold, as discussed earlier. However, by opening carbon pores, AW allows for a more complete elution and helps restoring the adsorption rate of the carbon (Faulkner et al., 1987; Smith et al., 1984).

Since extraction efficiency of CIP and CIL circuits is generally based on carbon kinetics, reduced aurocyanide adsorption rates can considerably impact gold recovery, potentially resulting in increased gold losses over time. However, due to the precipitation and adsorption of a heterogeneous mixture of IF, chemical regeneration usually only partially restores carbon activity (van Vliet, 1982). Consequently, a suitable carbon characterization method is needed in order to investigate the type and content of IF across various stages of the operational plant.

## 2.5 Characterization Techniques for Activated Carbon

### 2.5.1 Classical Tests

Several methods and tests are commonly used to characterize GAC and its physical properties, e.g., BET surface area, activity testing, apparent density, hardness number, ash content, iodine number and pore volume, among others (Cevallos Toledo et al., 2020; Li et al., 2002; G. McDougall et al., 1981; Pleysier et al., 2008; Urbanic et al., 1985; van Deventer & van der Merwe, 1994). More advanced techniques previously used for GAC characterization are X-ray computed microtomography, X-ray diffraction (XRD), thermogravimetric analysis, Fourier transform infrared spectroscopy and SEM, including its various imaging modes (Pleysier et al., 2008; Smith et al., 1984; Unugul & Nigiz, 2020). Whereas most of these methods were used to enhance the understanding of adsorption mechanisms of gold or other adsorbates, characterization of IF was primarily done using SEM.

### 2.5.2 Scanning Electron Microscopy

SEM offers high-resolution images of the carbon surface and, when equipped with EDS detectors, can be used to identify elemental compositions of the IF. However, while providing deep insights into surface morphology and elemental composition, the characterization of IF using SEM-EDS is limited in several ways. SEM-EDS typically focuses on selected areas, restricting analysis to smaller regions and limiting the coverage of larger areas. Accordingly, heterogeneously distributed contaminants might be overlooked or their abundance underestimated. Furthermore, the selection of analysis points and the interpretation of results by the operator are prone to operator bias, while the small-scale nature of the analysis brings along a lower statistical representativeness with respect to the entire GAC particle (Han et al., 2022; Pszonka & Schulz, 2022).

SEM-based automated mineralogy (SEM-AM) has been getting more attention recently, finding increasing application across various fields (Schulz et al., 2020). SEM-AM is a combined analytical tool based on SEM-EDS equipped with a backscattered electron (BSE) detector and a computer software platform for measurement and analysis automation. First, a high-resolution BSE image is produced based on the signals generated from elastic collisions between the SEM-generated electron beam and the sample atoms. The image can be subsequently refined using a variety of processing steps like particulation and segmentation. Following, EDS spectra are collected to obtain the elemental compositions. Depending on the software provider, different classification algorithms and measurement routines, e.g., single point or EDS spectral mapping, can be used. The spectra are then compared to reference spectra

for mineral identification and a classified image with false-color mineral mapping is produced at the micrometer scale. High-quality sample preparation is crucial and for granular samples commonly done using a non-evaporating, electro-beam stable epoxy resin mixed with hardener and subsequent polishing.

A thorough search of the relevant literature suggests that SEM-AM has not been previously used for the characterization of IF on GAC. However, its capabilities in providing automated quantification, detailed mineral mapping and reproducibility through reduced operator bias, among other benefits, may position it as a useful tool (Blannin et al., 2021). Moreover, it could provide insight on both external and internal surfaces of the GAC. This work will focus on the application of SEM-AM in combination with classical tests and methods, i.e., inductively coupled plasma optical emission spectroscopy (ICP-OES), X-ray fluorescence (XRF) analysis, activity testing and specific surface area determination.

# 3. Materials and Methods

## 3.1 LaRonde Mill Circuit

GAC samples were provided by the LaRonde Mine, operated by Agnico Eagle Mines Limited and located approximately 45 km east of Rouyn-Noranda in the province of Quebec, Canada. The LaRonde Mine processes a blend of free milling ore from multiple deposits, with an average composition of 4 ppm Au, 10 ppm Ag, 0.2 % Cu, 0.15 % Zn and 0.02 % Pb. Ore processing involves crushing, grinding (d80 = 75 µm) and a flotation circuit (Rougher-Scavenger-Cleaner) to produce copper and zinc concentrates. Approximately two-thirds of the gold is found in the copper concentrate. Flotation tailings are subjected to cyanidation followed by a CIP circuit, from which the loaded carbon is subsequently treated through AW, elution and TR. The reactivated GAC is returned to the adsorption tanks, while the eluate is directed to electrowinning cells for the production of gold cathodes and ultimately doré bars. A simplified flowsheet is presented in Appendix A (Figure 30).

## 3.2 Sampling Campaign

### 3.2.1 Sampling Points

GAC samples were collected at different stages of the circuit, i.e., from all eight adsorption tanks (AC1-T1–T8), after AW (AC2), after elution (AC3) and after TR (AC4), collectively referred to as ‘process carbon’. In addition, ‘virgin carbon’ (AC5) and process water (PW) was sampled, resulting in a total of 12 solid GAC samples and 1 liquid sample (Figure 9).

Sampling points were selected to investigate the progression and removal of IF throughout the processing circuit and relate it to the gold loading. The PW sample was collected in order to investigate its purity and potential fouling effects following TR. Sampling was conducted on a single operational cycle to ensure that the analysis reflects changes occurring within that specific cycle, while minimizing variability introduced by differences between separate cycles. In contrast, AW, elution and TR are batch processes, hence their samples inherently represent multiple adsorption cycles.

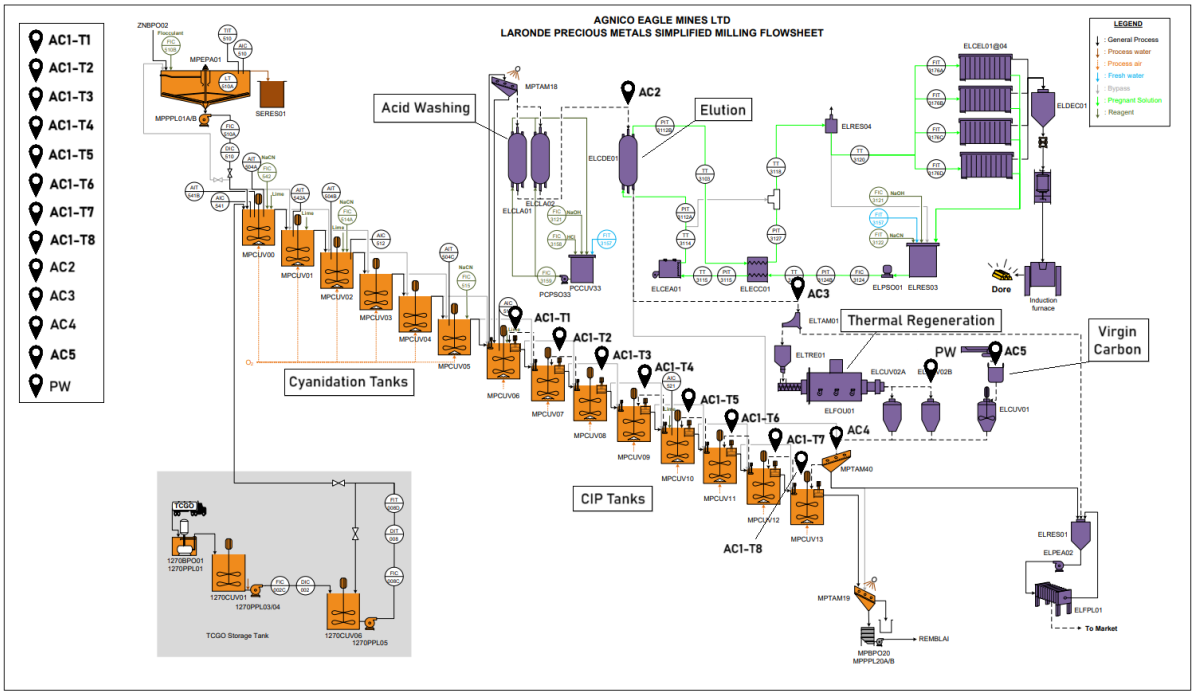


Figure 9. Simplified milling flowsheet of the LaRonde precious metals circuit including list and locations of sampling points (adapted from internal documentation provided by Ph.D. Raphaël Mermillod-Blondin, Agnico Eagle Mines Ltd., 2025).

### 3.2.2 Sample Collection

Samples AC1-T1–T8 were obtained directly during a plant visit, while samples AC2, AC3, AC4, AC5 and the PW sample were collected and provided by the operations team due to accessibility restraints of the sampling locations. Sampling of the adsorption tanks was done manually through an access hatch at the top of the adsorption tanks. As shown in Figure 10a, a dip sampler was fully submerged into the agitated pulp and filled completely with slurry containing GAC. After withdrawing the sampler, it was emptied over a 425 µm screen into a cleaned collection bucket. The sampling procedure was repeated until approximately 1 L of GAC was obtained. Subsequently, all GAC samples, except the virgin carbon, were washed over the screen using PW to remove any retained slurry, transferred into a plastic bottle and sealed airtight.

Sample AC2 was taken at the outlet of the transfer pipe between the AW and elution columns, whereas AC3 was sampled right before entering the kiln. Sample AC4 was obtained from the carbon screen MPTAM40 after TR and water quenching. Virgin Carbon (AC5) was sampled from a big storage bag, while the PW was obtained from the quench water tank.


Figure 10. (a) Manual carbon sampling of the adsorption tanks using a dip sampler; (b) close-up of the dip sampler and the carbon screen.

Upon arrival at the laboratory, all samples were placed in the oven to dry at 90 °C overnight. After drying, a white coating was observed on the tray walls and on the surface of all samples. As a result, all samples, including the samples provided by the operations team, were rinsed again at the laboratory over a 425 µm screen using demineralized water and re-dried under the same conditions to guarantee equal treatment of all samples. Following this additional step, the coating was largely eliminated (Figure 11b). Dried samples were stored in sealed plastic bags until further use.

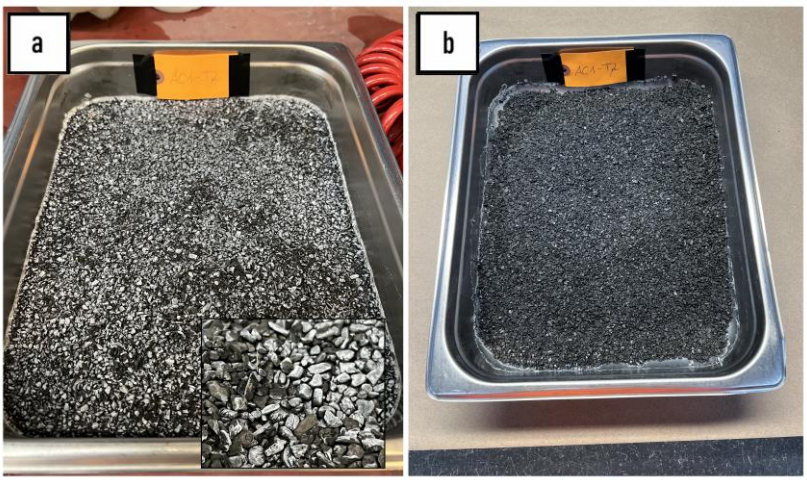


Figure 11. (a) AC1-T2 after initial drying without rinsing, showing a white surface coating; (b) the same sample after rinsing with demineralized water and re-drying, showing removal of coating.

## 3.3 Sample Preparation

### 3.3.1 Subsampling and Analytical Preparation

Sample preparation was carried out in accordance with quality assurance and quality control (QA/QC) standards and internal protocols of Agnico Eagle Mines Limited. The objective was to obtain representative subsamples across different size fractions and for various analytical methods.

Size classification was done to ensure valid comparisons between samples and minimize size-related bias, as smaller particles may behave differently in the circuit than larger particles. In order to approximate the general size distribution of the GAC present in the mill circuit and thereby establish suitable size fractions, sample AC1-T8 was sieved using a vibratory sieve shaker for 20 min with an amplitude of 2.0 mm (Analysette 3, Fritsch GmbH, Idar-Oberstein, Germany; see Figure 12). Based on this, samples were sieved to the following size fractions during sample preparation: < 1.4 mm (F2), 1.4–2 mm (F3) and > 2 mm (F4). Additionally, unsieved subsamples, representing the mixed size fraction (F1), were retained for each sampling point prior to sieving. Thus, Fraction F1 represents the native particle size distribution as it is present in the circuit. The detailed sample preparation procedure can be seen in Appendix A Figure 31.

Subsampling into 8 or 10 subsamples was done using a vibratory feeder combined with a rotary cone sample divider (Laborette 24 and 27, Fritsch GmbH, Idar-Oberstein, Germany). Sample division into 2 subsamples was done using a riffle splitter. Samples analyzed for total gold and sulfur content as well as elemental composition were pulverized to 30 µm using a planetary mill (Pulverisette 5, Fritsch GmbH, Idar-Oberstein, Germany). Pulverization was performed at 200 rpm for 20 min using 35 steel balls (¾ inch diameter) per grinding jar. After each

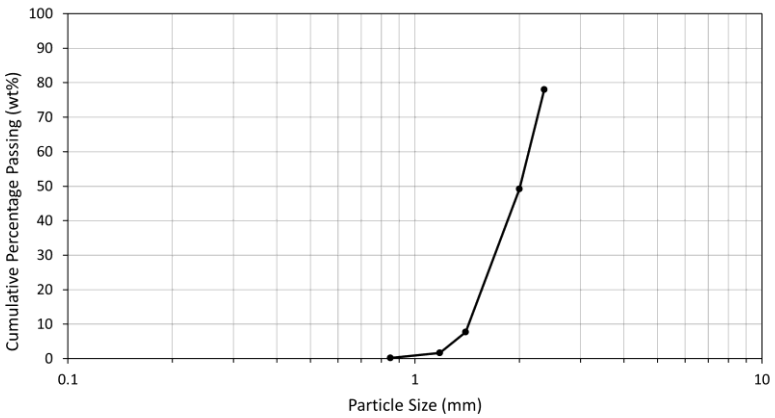


Figure 12. Cumulative particle size distribution curve of the sample AC1-T8. Note that the X-axis is logarithmic.

pulverization step, grinding jars were cleaned using silica as a cleaning medium. Pulverized samples were transferred into heat resistant plastic bottles, dried at 95 °C for 2 h and immediately sealed afterwards, creating a partial vacuum upon cooling. Particle samples were stored in sealed plastic bottles without prior drying.

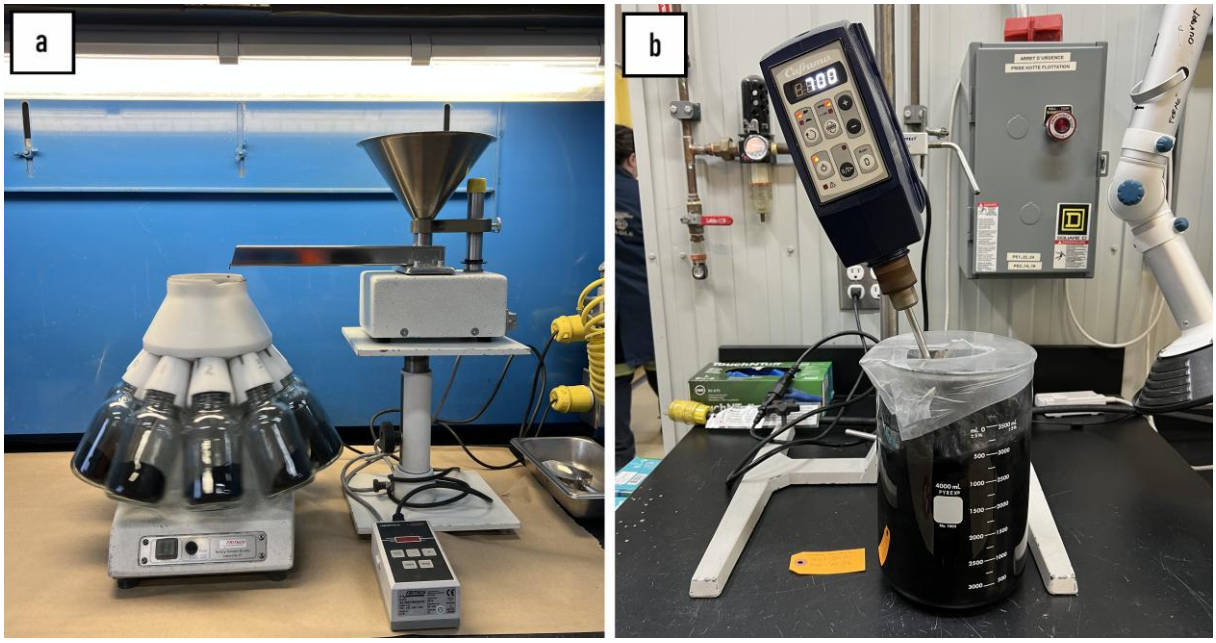


Figure 13. (a) Rotary cone sample divider and vibratory feeder; (b) attrition of virgin carbon using overhead stirrer.

### 3.3.2 Activity Test

Activity testing was done for the F3 size fraction as requested by internal laboratory protocols. Sample preparation involved attrition of the virgin carbon, which was used as a reference for gold adsorption kinetics. For the attrition, 600 g of GAC was weighed and mixed with 2.5 L demineralized water in a 4 L beaker. An overhead stirrer was placed inside the beaker at an approximate angle of 10–20° from the vertical axis. The mixture was stirred at 700 rpm for 2 h, washed over a 600 µm screen to remove fines produced during attrition and rinsed using demineralized water. After drying of the attrited carbon at 90 °C overnight, it was sieved to obtain the F3 size fraction.

Following sieving, activity test samples were rinsed using demineralized water over a 600 µm screen to remove dust accumulated on the particles during sieving and dried again at 90 °C overnight. After drying, subsamples were first divided using the rotary sample divider to approximate a target mass of 3.50 g and then adjusted to exactly 3.50 g using a precision balance (XS6002S, Mettler Toledo, Greifensee, Switzerland; readability: 0.01 g). The samples were soaked in distilled water 18 h before the activity test to ensure that micropores are already activated at the start of the test.

## 3.4 Polished Block Preparation

For a comprehensive analysis of GAC using SEM-AM, resin blocks should most importantly: (1) contain a single, uniform layer of well-separated GAC particles to allow for consistent polishing, (2) encapsulate and retain inorganic contaminants within the carbon porosity to prevent their loss during polishing and (3) be free of air bubbles or voids.

Embedding of the GAC and fabrication of the resin block was carried out in two steps: first, an initial thin resin layer holding the particles was prepared, followed by the addition of a base resin layer to form a solid block, which was then further processed into a polished block (PB).

PBs were prepared for SEM-AM analysis of the F3 size fraction, which was determined to be the primary fraction for detailed characterization (Table 1). This choice was based on the activity testing protocol, which specified the use of the 1.4–2 mm size fraction, and on its large proportion (41.5 %) in the circuit. Therefore, F3 carbon samples were homogenized by gently rolling and inverting the sample container multiple times to ensure even distribution of the particles. For each sampling point, several hundred GAC particles were poured onto a sheet of paper. From these, a subset of 200 particles were distributed on a numbered grid sheet (1–200), where one particle was placed in each cell, as shown in Figure 14a. Following, 30 unique integers between 1–200 were selected using Random.org and their corresponding particles selected for preparation and subsequent analysis.

Table 1. Selected size fractions: mixed (F1), < 1.4 mm (F2), 1.4–2 mm (F3) and > 2 mm (F4) for each analysis method and test. Abbreviations: BET = Brunauer-Emmett-Teller; ICP-OES = inductively coupled plasma optical emission spectroscopy; OM = optical microscopy; SEM-AM = scanning electron microscopy-based automated mineralogy; XRF = X-ray fluorescence.

| Sampling Point | ICP-OES Spectr. | Au content | Total S content | XRF | BET | SEM-AM | OM | Activity Test |
|---|---|---|---|---|---|---|---|---|
| AC1-T1 | F1, F2, F3, F4 | F1, F2, F3, F4 | F1, F2, F3, F4 | F3 | F3 | F3 | F3 | F3 |
| AC1-T2 | - | - | - | - | F3 | - | F3 | - |
| AC1-T3 | F1, F2, F3, F4 | F1, F2, F3, F4 | F1, F2, F3, F4 | - | F3 | F3 | F3 | - |
| AC1-T4 | - | - | - | - | F3 | - | F3 | - |
| AC1-T5 | F1, F2, F3, F4 | F1, F2, F3, F4 | F1, F2, F3, F4 | - | F3 | F3 | F3 | - |
| AC1-T6 | - | - | - | - | F3 | - | F3 | - |
| AC1-T7 | F1, F2, F3, F4 | F1, F2, F3, F4 | F1, F2, F3, F4 | F3 | F3 | F3 | F3 | - |
| AC1-T8 | F1, F2, F3, F4 | F1, F2, F3, F4 | F1, F2, F3, F4 | - | F3 | - | F3 | F3 |
| AC2 | F1, F2, F3, F4 | F1, F2, F3, F4 | F1, F2, F3, F4 | F3 | F3 | F3 | F3 | F3 |
| AC3 | F1, F2, F3, F4 | F1, F2, F3, F4 | F1, F2, F3, F4 | F3 | F3 | F3 | F3 | F3 |
| AC4 | F1, F2, F3, F4 | F1, F2, F3, F4 | F1, F2, F3, F4 | F3 | F3 | F3 | F3 | F3 |
| AC5 | F1 | - | F1 | - | F3 | - | F3 | F3 |

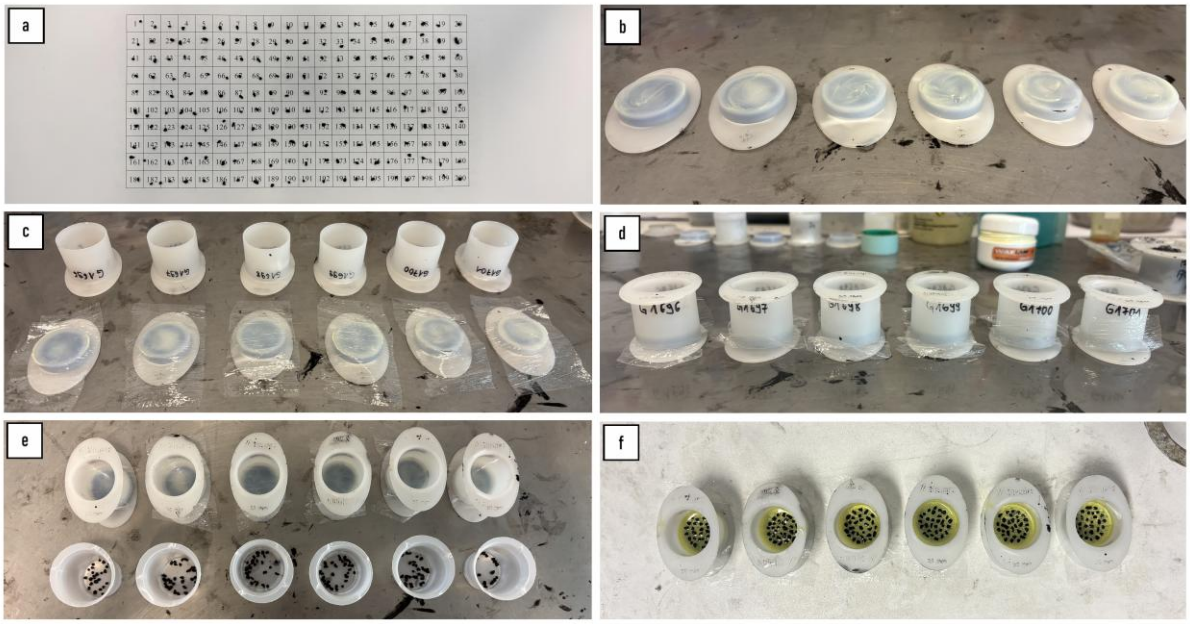


Figure 14. Steps in polished block preparation: (a) random selection of carbon particles; (b) application of demolding wax to mould; (c) placement of plastic film on mould base; (d) mould assembly; (e) prepared moulds with pre-selected particles; (f) particles embedded and arranged in first resin layer.

The mould was labeled with the corresponding sample code and demolding wax (WAXLAM, LAM PLAN, Gaillard, France) was applied to the bottom and sides of the mould (Figure 14b). Additionally, a plastic film was placed on the mould bottom to facilitate detachment of the cured resin and the mould was assembled (Figure 14c–d). For the initial resin layer, a slow curing epoxy resin was used to grant the resin more time to go inside the carbon porosity before being fully cured. A slow-curing epoxy resin was used for the initial resin layer to allow more time for the resin to penetrate into the carbon porosity before curing. To enhance contrast between carbon and epoxy resin, iodoform was added to the resin at a concentration of 15 wt.%, as recommended by Creelman & Ward (1996) and Rahfeld & Gutzmer (2017). For each 10 g of epoxy resin, 5 g of hardener was added and thoroughly mixed.

Placing the GAC particles into the mould prior to resin addition led to their adhesion to the mould walls and partial coating with demolding wax. To avoid this, a few drops of resin were first applied to the mould bottom and evenly spread, producing a thin resin layer. The particles were then placed onto this layer and more resin was added until all particles were adequately embedded and a uniform layer of approximately 1.5 mm was produced. Care was taken to avoid excessive resin addition in order to prevent the particles from sinking and floating, thereby maintaining them in a single, uniform layer. The moulds were placed in a vacuum chamber at 0.75 bar for 3 h to enhance resin penetration into the porous carbon structure and lock the inorganic contaminants. Following, due to particle movement under vacuum, the particles were

repositioned to prevent them from touching and the resin layer was left to cure for 24 h at room temperature (Figure 14f).

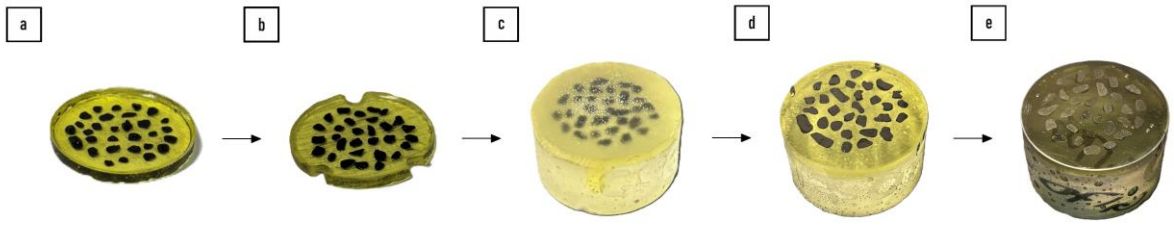


Figure 15. Stepwise preparation of the polished block: (a) cured initial resin layer with placed carbon particles; (b) keyed initial resin layer; (c) cured resin block after base resin casting; (d) resin block with polished surface; (e) silver-metallized polished block.

Once cured, the initial resin layer was retrieved from the mould and engraved on the sides (Figure 15a–b). The process of keying ensured a mechanical bond with the subsequent base resin layer, forming a single, solid resin block. Demolding wax was reapplied to the mould walls and the keyed resin layer was reinserted into the mould. For the base resin layer, 16 g of a fast-curing epoxy resin was thoroughly mixed with 2 g of hardener. The mixture was poured into the mould to a height of approximately 1.5 cm, encasing the keyed resin layer. The moulds were then placed in the vacuum chamber at 0.75 bar for 3 h in order to remove entrapped air and left to cure for 8 h at room temperature. After curing, the completed resin block was obtained from the mould (Figure 15c), engraved with the corresponding sample code and polished.

Resin blocks were first polished manually using silicon carbide abrasive paper discs. Initial manually polishing was done using P320 grit paper, exposing and sectioning the GAC particles through their approximate centers. Manual polishing was continued with progressively decreasing grit size (P400, P600 and P1200). Blocks were further polished using a semi-automatic grinding and polishing machine (Tegramin-30, Struers, Ballerup, Denmark). Initial semi-automatic grinding was performed without lubricant using a 2000 MD-Disk, followed by polishing with diamond suspensions at progressively decreasing grit sizes (9 µm, 3 µm and 1 µm). The finished PB can be seen in Figure 15d.

Finally, PB surfaces were coated with a silver layer by metallization to create an electrically conductive surface, which is necessary for SEM analysis (Figure 15e). Metallization was done for a time interval of 60 s using a sputter coater (Q150R ES, Quorum Technologies, Lewes, United Kingdom).

## 3.5 Sample Analysis

### 3.5.1 Activity Test

Activity tests were done to assess the gold adsorption performance of sampled GAC over time. Tests were conducted in three runs for the sampling points AC1-T1, AC1-T8, AC2, AC3, AC4 and AC5 (Table 1). For each sampling point except AC5, three 3.50 g samples of GAC were prepared and pre-soaked – one for each of the three determined time intervals (1, 2 and 4 h). For AC5, five 3.50 g samples were prepared, since it was used as a reference throughout all three activity test runs. During the first run, AC5 was tested for all three time intervals to serve as a reference for gold adsorption of virgin carbon. In the subsequent two test runs, AC5 was included as a reference sample in the 4 h interval in case of discrepancies or issues arising during the trial. This resulted in a total of 20 carbon samples for the activity test.

Pregnant cyanide solution from the elution circuit of the LaRonde mill was used to achieve results that more closely reflect the conditions present in the actual circuit compared to synthetic gold solutions. Based on information provided by the operations team, gold concentration of the pregnant solution was assumed to be 70 $g \cdot L^{-1}$. To achieve an approximate ratio of 10 $g \cdot L^{-1}$ of Au for 1 $g \cdot L^{-1}$ of carbon, 500 ml of pregnant solution was diluted with 500 ml of demineralized water to obtain an approximate gold concentration of 35 $g \cdot L^{-1}$. The diluted solution was transferred into a 4 L glass bottle (Figure 16a) and a 60 mL head sample was collected daily before starting the activity test to determine the initial gold concentration.

Additionally, pH, temperature and electrical conductivity were measured using a portable multiparameter meter (Orion Star™ A326, Thermo Fisher Scientific, Waltham, MA, United States). The 3.50 g pre-soaked carbon sample was added to the bottle and time measurement began upon contact with the solution. The sealed bottles were then placed on a horizontal roller table set to 40 rpm (Figure 16b).

Bottles were obtained after each respective time interval and the solution decanted using a vacuum filtration system equipped with ME25 membrane filters (0.45 µm pore size), as seen in Figure 16c. Following decantation, pH, temperature and electrical conductivity were measured and 60 mL of solution was sampled that was sent to the laboratory for gold analysis. The carbon was recovered, transferred into a pan and dried at 90 °C overnight (Figure 16d). Once dry, the carbon was weighed again and pulverized to 30 µm using the planetary mill. The pulverized carbon was transferred into heat-resistant plastic containers and dried again for

several hours. After drying, the bottles were immediately sealed and the carbon was then sent to the laboratory for gold analysis.

Carbon activity is usually described by the gold adsorption rate constant, which is calculated from the plotted change in gold solution concentration over time and the equilibrium gold concentration. However, plotting revealed that no equilibrium was reached after 4 h, thus activity was calculated according to Eq. (9):

$$activity\ \% = \frac{head\ solution\ grade - grade\ of\ sampled\ carbon\ solution}{head\ solution\ grade - grade\ of\ virgin\ carbon\ solution} \cdot 100 \quad (9)$$

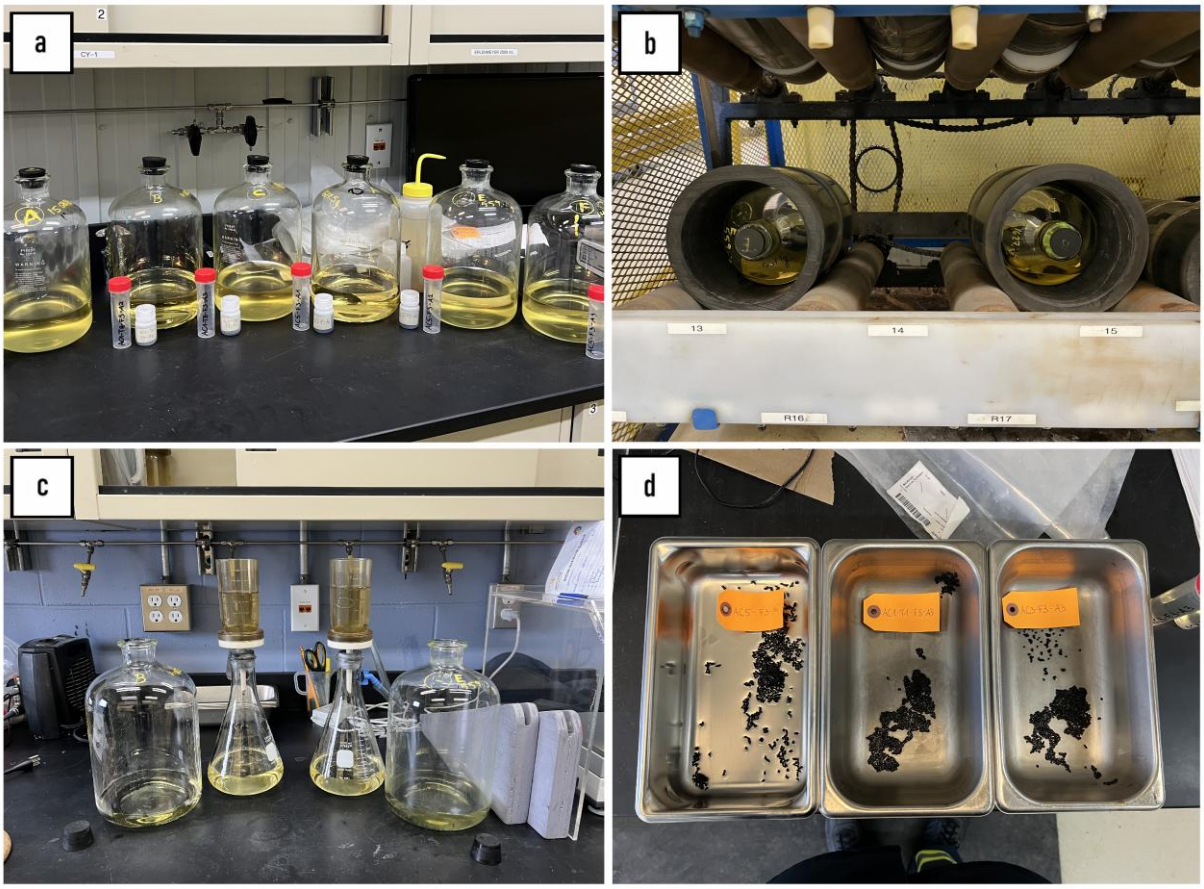


Figure 16. a) Preparation of 1 L gold cyanide test solutions; b) bottles placed on horizontal roller table for continuous mixing of carbon with solution; c) decantation of the solution using vacuum filtration systems; d) carbon samples loaded with adsorbed gold are transferred into trays for drying.

### 3.5.2 Laboratory Analysis

Samples were sent to the LaRonde laboratory for analysis of the gold content, total sulfur content and elemental composition.

Gold content was determined for all solid and liquid samples from the activity test as well as for all size fractions of the sampling points AC1-T1, -T3, -T5, -T7, -T8, AC2, AC3 and AC4, resulting in a total of 75 samples (Table 1). Regarding gold analysis of samples not belonging to the activity test, all size fractions were analyzed in order to investigate potential differences in gold adsorption as a result of particle size variation. These samples were analyzed in triplicate and the average value was used for data analysis. Gold analysis of pulverized carbon was done using fire assay followed by microwave plasma-atomic emission spectroscopy (MP-AES). For liquid samples, gold content was determined using sponge-lead preconcentration, followed by fire assay and MP-AES. For pulverized and liquid samples, analysis was done in duplicate assays with the average of the replicate measurements being used for data analysis.

Total sulfur content was determined by high-temperature combustion with infrared detection using a C-S analyzer.

Elemental composition was determined using acid digestion and ICP-OES detection. Carbon samples were analyzed for Ag, Al, As, Au, Ba, Be, Bi, Ca, Cd, Co, Cr, Cu, Fe, K, Mg, Mn, Mo, Na, Ni, P, Pb, S, Sb, Sc, Se, Sn, Sr, Te, Ti, Tl, V, Y, Zn and Zr. Similar to the gold content, ICP-OES was done in duplicate assays and the average was used for data analysis. For both methods, 33 carbon samples were analyzed, i.e., all size fractions of the sampling points AC1-T1, -T3, -T5, -T7, -T8, AC2, AC3 and AC4 as well as fraction F1 of sampling point AC5 (Table 1). As for the gold content analysis, all size fractions were analyzed in order to investigate differences in elemental compositions between different particle sizes. In addition to the GAC samples, the PW sample was analyzed for dissolved metals using ICP-OES.

In order to verify ICP-OES assays, GAC samples of the sampling points AC1-T1, AC1-T7, AC2, AC3 and AC4 were also analyzed at the laboratory in Liège using XRF.

### 3.5.3 Surface Area Determination

Surface area of the GAC was determined in using two different methods, i.e., BET nitrogen adsorption and manual polygonal segmentation, yielding the total specific surface area (SSA) ($m^2 \cdot g^{-1}$) and the projected geometric surface area ($\mu m^2$).

SSA was measured to investigate potential pore blocking as a result of increased IF. For the analysis, samples were sent to the "Unité de recherche et de service en technologie minérale" (URSTM) of the "Université du Québec en Abitibi-Témiscamingue" (UQAT). SSA determination was done using the multipoint BET method on the F3 fraction of all sampling

points to ensure consistent and comparable results in combination with SEM-AM and activity testing.

Determination of the projected or cross-sectional surface area was done to provide a reference for relating the mineralogic data from SEM-AM to the carbon surface of the PB. This enabled the quantification of changes in total IF between GAC from different sampling points by normalizing IF data to the measured carbon surface area. Manual polygonal segmentation was performed on tiled images of the PBs, obtained via optical microscope (Axio Imager M2m, Carl Zeiss AG, Oberkochen, Germany), using the ZEISS Efficient Navigation software.

### 3.5.4 SEM-Based Automated Mineralogy

SEM-AM was performed using a field emission-SEM (Sigma 300, Carl Zeiss AG, Oberkochen, Germany) equipped with two EDS spectrometers (XFlash 6|30, Bruker, Billerica, MA, United States). Before starting the analysis, calibration of the EDS detector system, having a detection limit of 1000 ppm, was done using copper as reference material. Analysis of PBs was carried out under vacuum using a probe current of 2.3 nA, an accelerating voltage of 20 kV, an aperture size of 120 µm and a working distance of 8.5 mm. The software used for automated, quantitative mineralogical analysis was ZEISS Mineralogic, which offers five analysis modes, i.e., mapping, spot centroid, feature scan, line scan and BSE only.

For this study, the spot centroid analysis mode was selected, as it offers an extremely fast measurement mode. Spot centroid analysis involves segmenting the BSE image for the identification of individual mineral grains, determining the geometric center of each grain and performing a single EDS measurement at that central point. Centroid dwell time was fixed to 0.07 s. While this mode requires fewer EDS spectra to be collected and analyzed, its accuracy is strongly dependent on the phase thresholding. Thus, to obtain reliable results, while avoiding excess measurement durations, an image processing recipe was designed.

BSE image processing commenced with the application of a median filter, reducing overall noise. Following, an upper and a lower greyscale threshold was applied to include mineral grains, while excluding resin and carbon structure from the analysis. Morphological operations included erosion, dilation and reconstruction which allowed enlarging adjacent regions of the same greyscale and merging neighboring grains into a single analytical unit, thereby reducing overall analysis time.

Following the EDS measurement, the acquired spectrum is processed to quantify the elemental composition of the grain. Based on this composition and predefined mineral classification rules,

ZEISS Mineralogic assigns the grain to a specific mineral category. Mineral classification rules were based on a combination of a variety of factors, e.g., elemental thresholds, greyscale thresholds and element presence or absence. SEM-AM was performed for the samples AC1-T1, -T3, -T5, -T7, AC2, AC3 and AC4.

## 3.6 Data Normalization and Reconciliation

### 3.6.1 Inorganic Fouling Normalization

In order to quantitatively compare IF between sampling points and perform data reconciliation, mineralogical data obtained from the SEM was normalized based on the GAC surface area of each PB. SEM-AM of the PBs provided comprehensive data sets, offering information on multiple characteristics of each analyzed grain. The parameters that were obtained from the IF data set and used for this study depict: each grains' mineral classification, area ($\mu m^2$), mass (g) and elemental composition (wt.%).

First, area and weight proportions of all minerals were calculated according to:

$$A_{SEM,m} = \frac{\sum_{i=1}^{N}(A_i \cdot \delta(M_i = m))}{\sum_{i=1}^{N} A_i} \cdot 100 \tag{10}$$

$$W_{SEM,m} = \frac{\sum_{i=1}^{N}(W_i \cdot \delta(M_i = m))}{\sum_{i=1}^{N} W_i} \cdot 100 \tag{11}$$

with the indicator function $\delta(M_i = m)$ defined as:

$$\delta(M_i = m) = \begin{cases} 1, & \text{if grain } i \text{ is classified as } m \\ 0, & \text{otherwise} \end{cases}$$

where $A_{SEM,m}$ and $W_{SEM,m}$ are the area and weight proportions (%) of each mineral $m$ within the IF data set, $A_i$ and $W_i$ are the area ($\mu m^2$) and mass (g) of grain $i$, $N$ is the total number of grains and $M_i$ is the mineral classification of grain $i$.

Using the density $\rho_m$ ($g \cdot cm^{-3}$) of each mineral $m$ (obtained from *WebMineral.com*), the average density $\bar{\rho}_{IF}$ ($g \cdot cm^{-3}$) of the entire IF (i.e., across all grains $i$=1 to $N$) was calculated according to:

$$\bar{\rho}_{IF} = \frac{1}{|S|} \sum_{m \in S} \left( \frac{A_{SEM,m} \cdot \rho_m}{W_{SEM,m}} \right) \tag{12}$$

where $S$ is the set of identified minerals in the IF data set and $|S|$ is the number of distinct minerals. This formula was adopted from previous work and involved calculating the IF density

from each mineral $m$ (expression inside summation). The resulting IF densities were consistent across all minerals (±0.01 g·cm$^{-3}$) and averaged across the mineral set $S$.

Subsequently, the normalized area of each mineral $m$, $A_{norm,m}$ (%), relative to the GAC particle, was calculated using the data obtained from manual polygonal segmentation, according to:

$$A_{norm,m} = \frac{\sum_{i=1}^{N}(A_i \cdot \delta(M_i = m))}{A_{GAC}} \cdot 100 \tag{13}$$

where $A_{GAC}$ represents the absolute surface area of the GAC particle (µm$^2$), including IF and the carbon's porosity.

In order to convert mineral area fractions into normalized weight fractions, the surface-area-weighted average density of the GAC particle $\bar{\rho}_{GAC+IF}$ (g·cm$^{-3}$) was calculated using:

$$\bar{\rho}_{GAC+IF} = \frac{A_{norm,IF} \cdot \bar{\rho}_{IF} + A_{norm,GAC} \cdot \rho_{GAC}}{100} \tag{14}$$

with:

$$A_{norm,IF} = \sum_{m \in S} A_{norm,m} \tag{15}$$

$$A_{norm,GAC} = 100 - A_{norm,IF} \tag{16}$$

where $A_{norm,IF}$ is the total area of IF relative to the GAC particle (%), $A_{norm,GAC}$ is the total area of activated carbon relative to the GAC particle (%) and $\rho_{GAC}$ is the bulk density of activated carbon (g·cm$^{-3}$) obtained from the technical data sheet provided by the carbon manufacturer.

Using $\bar{\rho}_{GAC+IF}$, it was then possible to calculate the normalized weight proportion of each mineral $m$, $W_{norm,m}$ (%), relative to the GAC particle, according to:

$$W_{norm,m} = \frac{A_{norm,m} \cdot \rho_m}{\bar{\rho}_{GAC+IF}} \tag{17}$$

Similar to $A_{norm,IF}$ and $A_{norm,GAC}$, the total normalized weight proportions of IF $W_{norm,IF}$ and activated carbon $W_{norm,GAC}$ (%) were calculated using:

$$W_{norm,IF} = \sum_{m \in S} W_{norm,m} \tag{18}$$

$$W_{norm,GAC} = 100 - W_{norm,IF} \tag{19}$$

### 3.6.2 Data Reconciliation

In order to perform data reconciliation, the raw average elemental content $\bar{E}_{m,e}^{raw}$ (wt.%) of each element *e* in each mineral *m* was calculated based on the EDS data of each grain from the IF data set using:

$$\bar{E}_{m,e}^{raw} = \frac{\sum_{i=1}^{N} \left( E_{i,e} \cdot \delta(M_i = m) \right)}{\sum_{i=1}^{N} \delta(M_i = m)} \tag{20}$$

where $E_{i,e}$ is the fraction of element *e* in grain *i* (wt.%).

The raw elemental composition was then refined using a selection matrix $\chi_{m,e}$ according to:

$$\bar{E}_{m,e}^{refined} = \frac{\bar{E}_{m,e}^{raw} \cdot \chi_{m,e}}{\sum_e \left( \bar{E}_{m,e}^{raw} \cdot \chi_{m,e} \right)} \cdot 100 \tag{21}$$

where the selection matrix $\chi_{m,e}$ is defined as:

$$\chi_{m,e} = \begin{cases} 1, & \text{if element } e \text{ is selected for mineral } m \text{ in the matrix} \\ 0, & \text{otherwise} \end{cases}$$

The selection matrix determines whether the element *e* shall be considered for the refined elemental composition of mineral *m* or disregarded. Selection matrix refinement was applied due to the occurrence of EDS noise and signal overlap.

Ultimately, the total content of element *e*, $\bar{E}_e^{total}$ (wt..%), in the GAC particle was calculated using:

$$\bar{E}_e^{total} = \sum_{m \in S} \left( W_{norm,m} \cdot \frac{\bar{E}_{m,e}^{refined}}{100} \right) \tag{22}$$

## 3.7 Approach to Carbon Heterogeneity

Since acquisition times for the PBs were between 20 and 40 h, establishing a minimum representative sample size is crucial to reduce analysis time and associated costs. The proposed approach to determine the minimum sample size for acquisition involves:

1) Simulating inter-particle variability by bootstrapping the mineralogical data from randomly selected GAC particles. Accordingly, from a data set $D$ containing $N$ GAC particles, each with associated mineralogical data, random samples $S_n$ of size $n$ (where $n \in \{1, 2, ..., N\}$) are drawn without replacement.

2) For each sample $S_n$, the root mean square error (RMSE) of both mineral proportions and mineral content is calculated between the bootstrapped subset $S_n$ and the full data set $D$, according to:

$$RMSE_n^{proportion} = \sqrt{\frac{1}{|M|}\sum_{m\in M}\left(\frac{A_m(S_n)}{A(S_n)}\cdot 100 - \frac{A_m(D)}{A(D)}\cdot 100\right)^2} \quad (23)$$

where $M$ is the set of minerals, $A_m(S_n)$ is the area of mineral $m$ (µm²) within the sample $S_n$, $A(S_n)$ it the total mineral area (µm²) within sample $S_n$, $A_m(D)$ is the total area of mineral $m$ (µm²) in the full data set $D$ and $A(D)$ is the total mineral area (µm²) in the full data set $D$.

and:

$$RMSE_n^{content} = \sqrt{\frac{1}{|M|}\sum_{m\in M}\left(\frac{A_m(S_n)}{A_{GAC}(S_n)}\cdot 100 - \frac{A_m(D)}{A_{GAC}(D)}\cdot 100\right)^2} \quad (24)$$

where $A_{GAC}(S_n)$ is the area of activated carbon and IF (µm²) in the sample $S_n$ and $A_{GAC}(D)$ is the area of activated carbon and IF (µm²) in the full data set $D$.

3) Plotting the RMSE as a function of $n$ to identify the point at which the RMSE plateaus. Beyond this point, SEM acquisition will yield diminishing returns in new information, indicating that the subset approximates the full data set.

To evaluate whether the determined sample size can statistically reliably represent the IF in terms of quality (mineral proportions) and quantity (mineral content), performing multiple bootstrap resamplings (e.g., 200 iterations) with this sample size is proposed to simulate sampling variability. From these resamplings, the mean and standard deviation can be calculated for mineral proportions and content, allowing to define 95 % confidence intervals according to:

$$Confidence\ Interval = Mean \pm 1.96 \cdot \frac{Standard\ Deviation}{\sqrt{Number\ of\ Iterations}} \quad (25)$$

Verifying whether the reference data from the full data set lies within these confidence intervals indicates if the chosen sample size is sufficient for statistical representativeness.

This approach requires the mineralogical data to be linked to the individual GAC particle, which can be managed by capturing individual GAC particles separately with the SEM and saving the corresponding data after each acquisition. Similarly, the surface area of each GAC particle needs to be determined separately in order to perform the calculations described in Section 3.6 and determine the IF quantity. Lastly, it requires the 30 GAC particles to be representative of the entire GAC of each sampling point. Thus, based on data reconciliation, the number of GAC being used to generate the reference data set would need to be increased.

In this study, acquisition of entire PBs was performed without distinguishing mineralogical data for each separate GAC particle. The resulting data limitations prohibited the quantification of inter-particle variability. As an alternative, the proposed approach is demonstrated using mineral-grain bootstrapping instead of GAC-particle bootstrapping. It is important to note that this serves as an illustrative example and does not capture the true inter-particle variability of GAC.

## 3.8 Softwares

Statistical analyses were performed using RStudio (v2025.05.0 Build 496, Posit Software, PBC) and Quarto (v1.6.42) on Windows 10. Further data processing and automation was done using Microsoft Excel (v2506 Build 18925.20050) with custom VBA macros. VBA macros used for data processing were developed with the assistance of ChatGPT (GPT-4o, OpenAI, 2024). ChatGPT was further used for grammar refinement as well as language improvements.

# 4. Results

## 4.1 Elemental Composition

### 4.1.1 Process Carbon

Comprehensive elemental composition data for all samples, as determined by ICP-OES, is presented in Appendix B (Table 7). In the F1 fraction, representing the GAC size distribution as it is present in the circuit, calcium displayed the highest average content among all analyzed elements, ranging between 1.41–1.79 % (Table 2). Noticeably lower, the second most abundant elements were sulfur and sodium ranging from 0.33–0.61 % and 0.36–0.94 %, respectively. These were followed by Fe, Ag and P, with contents ranging between 0.19–0.59 %, 900.3–3167.5 $g \cdot t^{-1}$ and 0.07–0.12 %, respectively. All remaining elements were present at average contents < 0.1 %, with contents decreasing in the following order: Zn, Cu, Mg, Al, Cr, Ni, K, Sn, Se, Sr, Pb, Cd, As and Mn. For Ba, Mo, Sb, Te and Ti, ≥ 58 % of all samples analyzed were below the detection limit. Contents of Be, Bi, Co, Sc, Tl, V, Y and Zr were below the detection limit in all samples.

Table 2. Elemental contents of the F1 fraction of the process carbon determined using: inductively coupled plasma spectroscopy for Ag, Ca, S, Na, Fe and P; fire assay for Au; C-S analyzer for total S. Values represent the average of duplicate measurements for Ag, Ca, S, Na, Fe and P and triplicate measurements for Au.

| Sample | Au $g \cdot t^{-1}$ | Ag $g \cdot t^{-1}$ | Ca % | Total S % | S % | Na % | Fe % | P % |
|---|---|---|---|---|---|---|---|---|
| AC1-T8-F1-P | 38.44 | 1003.30 | 1.41 | 0.58 | 0.58 | 0.42 | 0.22 | 0.11 |
| AC1-T7-F1-P | 109.17 | 1454.10 | 1.54 | 0.61 | 0.61 | 0.41 | 0.21 | 0.11 |
| AC1-T5-F1-P | 411.08 | 2150.20 | 1.79 | 0.60 | 0.58 | 0.42 | 0.25 | 0.11 |
| AC1-T3-F1-P | 677.53 | 2656.20 | 1.55 | 0.51 | 0.51 | 0.37 | 0.20 | 0.11 |
| AC1-T1-F1-P | 1309.99 | 3037.40 | 1.72 | 0.56 | 0.51 | 0.36 | 0.22 | 0.11 |
| AC2-F1-P | 1364.20 | 3167.50 | 1.52 | 0.64 | 0.61 | 0.37 | 0.21 | 0.12 |
| AC3-F1-P | 64.23 | 1063.10 | 1.56 | 0.31 | 0.43 | 0.94 | 0.59 | 0.07 |
| AC4-F1-P | 38.23 | 900.30 | 1.48 | 0.57 | 0.33 | 0.66 | 0.19 | 0.10 |

Average total sulfur content obtained from the C-S analyzer was slightly higher compared to the ICP-OES measurement of S, ranging between 0.31–0.64 %. Gold content determined using fire assay ranged from 38.2–1364.2 $g \cdot t^{-1}$. Elemental contents of gold and total sulfur for all samples can be seen in Appendix B, Table 9.

Comparison of elemental contents on GAC across the size fractions F2–F4 showed different accumulation behaviors of certain elements. Au, Ca, Fe, Na, Al, Mg, K and S contents were significantly higher for the smallest size fraction F2 ($p < 0.05$) compared to F3 and F4. For Ca,

Na, K and S, F4 showed lowest contents, whereas contents of Fe, Al and Mg were essentially similar for fractions F3 and F4. In contrast, Cu, P and Ni contents were significantly higher in F4 ($p < 0.05$) compared to F2 and F3. Elements not mentioned either showed no apparent distribution pattern across size fractions or their content changes were limited to the least significant digit and thus considered insignificant.

### 4.1.2 Virgin Carbon

For all elements, contents were lower in the virgin carbon compared to the average contents of the process carbon. Only iron was present at comparable levels in both carbon types (virgin and process) and was by far the most abundant element in the F1 fraction of the virgin carbon with a content of 0.26 %. This was followed by calcium and magnesium with 0.039 % and 0.038 %, respectively. Other elements detected at contents ≥ 0.01 % included P, Cr, K, Na, Al and S, in decreasing order (Table 3). Sn, Mn, Cu, Ni and Sb were also detected, each at contents < 0.01 %, in decreasing order, while all remaining elements analyzed using ICP-OES and C-S analyzer were below the detection limit (Appendix B, Table 7).

Table 3. Elemental composition of virgin carbon determined using inductively coupled plasma spectroscopy, showing elements present at contents ≥ 0.01 %. Values represent the average of duplicate measurements.

| | Fe | Ca | Mg | P | Cr | K | Na | Al | S |
|---|---|---|---|---|---|---|---|---|---|
| Sample | % | % | % | % | % | % | % | % | % |
| AC5-F1-P | 0.255 | 0.039 | 0.038 | 0.022 | 0.021 | 0.021 | 0.018 | 0.012 | 0.010 |

## 4.2 Process Water Composition

Detailed results of the chemical analysis of the PW can be seen in Table 10 and revealed a high ionic strength of the PW (Appendix B). The by far highest concentration was observed for sodium with 3500 $mg \cdot l^{-1}$, followed by sulfur with 1640 $mg \cdot l^{-1}$. Elevated concentrations were also observed for Chloride (Cl) and thiocyanate (SCN), being 299.3 and 208.6 $mg \cdot l^{-1}$, respectively. Other species present at levels above 10 $mg \cdot l^{-1}$ were Zn, thiosulfate ($S_2O_3$), K and nitrate ($NO_3$, expressed as N) with concentrations of 93.3, 37.7, 36.0 and 17.6 $mg \cdot l^{-1}$, respectively. Species detected at levels below 10 and above 0.5 $mg \cdot l^{-1}$ include nitrite ($NO_2$), Cu, Se, Ca, P, Fe and As.

## 4.3 Carbon Activity

Activity of the sampled GAC, as determined using Eq. (9, can be seen in Figure 18a. All samples showed an increase in activity over time, except for AC1-T1 and AC2, demonstrating

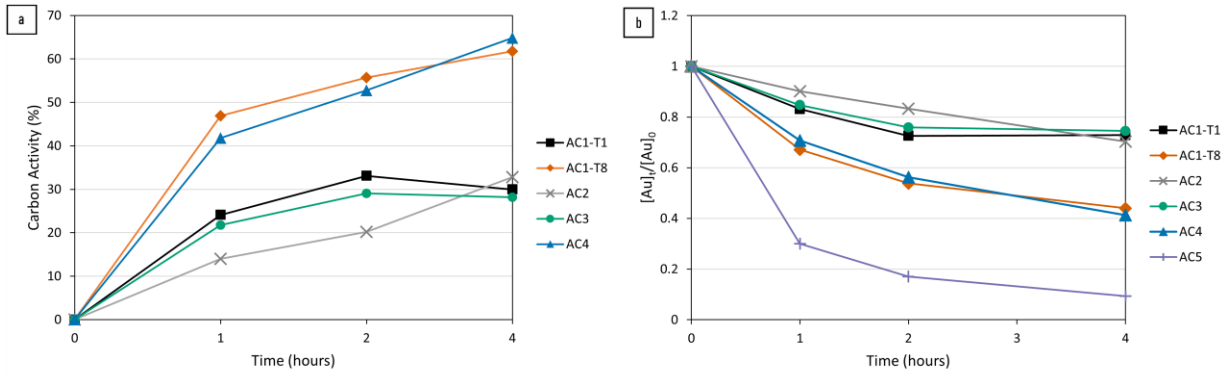


Figure 17. Activity test results: (a) carbon activity normalized against the performance of virgin carbon; (b) kinetic data of carbon adsorption, where $[Au]_t$ = gold solution concentration at time t and $[Au]_0$ = initial gold solution concentration.

a decrease in the last time interval. This was likely due to an incident that occurred during the experiment in which the rolling table stopped working for an unknown period, halting agitation inside the glass bottles. Overall, GAC from the first adsorption tank (AC1-T8) demonstrated the highest activity, increasing from 46.9 % to 61.8 % during the 4-hour time interval. Although the activity of GAC after TR (AC4) was initially lower for the first two time intervals compared to AC1-T8, it exceeded AC1-T8 after 4 hours, reaching 64.8 %. Activity of GAC from the last adsorption tank (AC1-T1) and after elution (AC3) was considerably lower. Excluding activity values of the last time interval due to the experimental incident, activity increased from 24.1 % to 33.9 % and from 21.8 % to 29.1 % for AC1-T1 and AC3, respectively, during the first 2 hours. Lowest activity was observed for GAC sampled after AW (AC2), increasing from 14.0 % to 32.8 %.

Carbon adsorption kinetic data is presented in Figure 18b, showing the gold adsorption from the solution over time. Evidently, kinetics were considerably faster for the virgin compared to the process carbon and generally slowing down over time. The continued decrease in gold concentration between 2 and 4 hours suggests that adsorption equilibrium was not yet established after 4 hours contact time.

## 4.4 Surface Area

### 4.4.1 Specific Surface Area

Data obtained from nitrogen adsorption can be seen in Figure 19. Virgin carbon demonstrated a SSA of 836.9 $m^2 \cdot g^{-1}$, considerably exceeding that of all other samples. Throughout the adsorption stage, the SSA of the process carbon showed a declining trend from the first to the last adsorption tank, decreasing from 503.9 to 373.3 $m^2 \cdot g^{-1}$, respectively. Following AW, SSA

remained unchanged compared to the last adsorption tank and increased slightly after elution. GAC after TR presented the highest SSA of the process carbon with 557.7 $m^2 \cdot g^{-1}$.

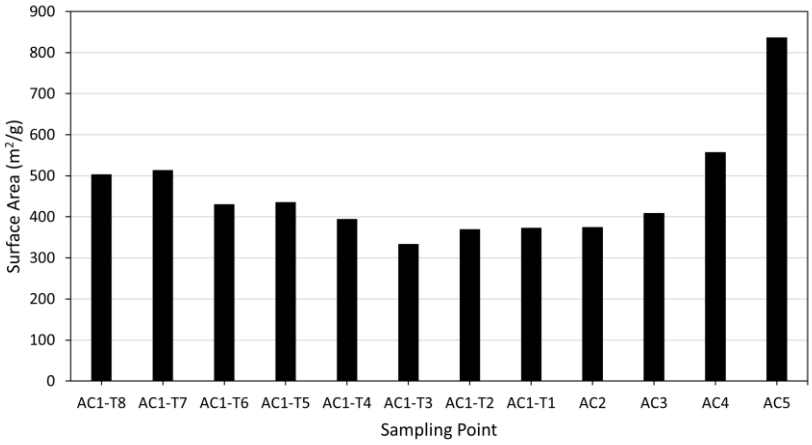


Figure 18. Specific surface area of the process and virgin activated carbon determined using nitrogen adsorption.

### 4.4.2 Cross-Sectional Surface Area

Results of the surface area estimation of GAC particles, embedded within the PBs, using manual polygonal segmentation can be seen in Table 4. Surface area obtained via manual segmentation varied between $97.0 \times 10^6$ and $143.9 \times 10^6$ $\mu m^2$.

Table 4. Surface area determination results for activated carbon particles using manual segmentation.

| Sample | Manual Segmentation ($\mu m^2$) |
|---|---|
| AC1-T1-F3 | 96 963 668 |
| AC1-T3-F3 | 108 976 352 |
| AC1-T5-F3 | 108 683 938 |
| AC1-T7-F3 | 133 983 625 |
| AC2-F3 | 143 936 263 |
| AC3-F3 | 124 935 729 |
| AC4-F3 | 134 275 382 |

## 4.5 SEM-Based Automated Mineralogy

### 4.5.1 Polished Block Preparation Method

The preparation method developed for the production of PBs provided good results for subsequent SEM-AM analysis. The use of a slow-curing resin allowed sufficient time for penetration into the carbon's porosity, as illustrated in Figure 20, effectively retaining the IF within pores and on the external carbon surface during polishing. Furthermore, the preparation method ensured equal polishing of all GAC particles, including at the resin-carbon interface, and almost no voids or bubbles were visible. Nevertheless, larger calcite accumulations

occasionally showed signs of partial removal during polishing, as observed in the BSE images. While this hindered the SEM's ability to detect these calcite grains, it suggests that polishing was too intense in some cases.

### 4.5.2 Mineralogical Composition of Inorganic Fouling

Mineral classification showed that IF was composed of a broad variety of mineral groups, including carbonates, silicates, oxides, sulfides, sulfates, phosphates, native elements, as well as mixed and non-mineral phases.

The carbonate fraction was almost entirely made up of calcite with minor ankerite [$Ca(Fe^{2+}$, Mg, Mn)$(CO_3)_2$]. The oxide group included iron oxides (not categorized further), ilmenite ($FeTiO_3$) and rutile ($TiO_2$). Apart from quartz ($SiO_2$), silicate minerals were not further differentiated, due to their complexity, and grouped under the general category "silicates". Sulfide minerals comprised pyrite, chalcopyrite, chalcocite ($Cu_2S$), arsenopyrite, pyrrhotite and sphalerite. Sulfates consisted of barite ($BaSO_4$) and gypsum ($CaSO_4 \cdot 2H_2O$), while phosphate minerals belonged to the apatite group, without further specification. Native elements and alloys present included gold and electrum. Finally, due to the occurrence of "mixels", i.e., grains composed of a mixture of signals from multiple minerals, and phases, which could not be attributed to distinct mineral species, grains were also classified into Ag-S, Ag-S-Cu > 10 %, Ag-S-Cu < 10 %, Fe > 90 % and Fe-O-Ca.

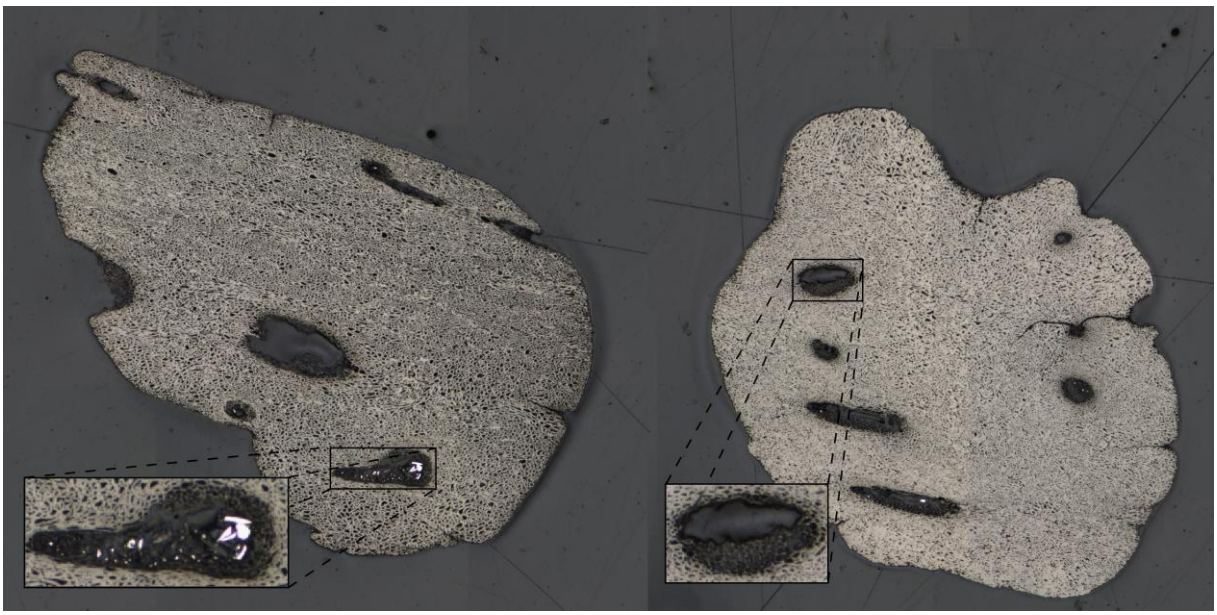

Figure 19. Optical microscopy image of activated carbon particles, showing macropores filled with resin and mineral grains.

### 4.5.3 Quantitative Variation of Inorganic Fouling

Total IF quantity was presented as the proportion of GAC particle surface area covered by mineral grains and is presented in Figure 21. Surface area was used for this comparison as it depicts a direct output from the SEM acquisition, while mass values are approximated by assigning mineral densities to each mineral category.

The number of mineral grains detected and analyzed by the SEM varied strongly between samples, ranging from 34,789 to 168,335 for the samples AC4 and AC1-T1, representing the sample after TR and the last CIP tank, respectively. Correspondingly, the amount of IF was highest in GAC from AC1-T1 (1.59 %) and lowest in GAC from AC4 (0.13 %). Similar to AC4, GAC from the first adsorption tank (AC1-T7) showed a low amount of IF with 0.16 %. IF increased drastically in AC1-T5 (3$^{rd}$ CIP tank) and continued to rise until reaching the last adsorption tank. Following AW, the amount of IF was reduced considerably to 0.21 % (AC2), increased again after elution to 0.56 % (AC3) and then dropped to its lowest level at AC4.

Exact proportions for mineral phases detected above 0.01 % relative to the total GAC surface area can be seen in Table 5. Calcite was by far the most abundant mineral in all samples, ranging between 0.05 and 1.38 %. Silicates were the second most abundant category with surface area proportions between 0.022 and 0.089 %. This was followed by Fe-O-Ca mixed phases and iron oxides, ranging from 0.011 to 0.089 % and 0.022 to 0.070 %, respectively.

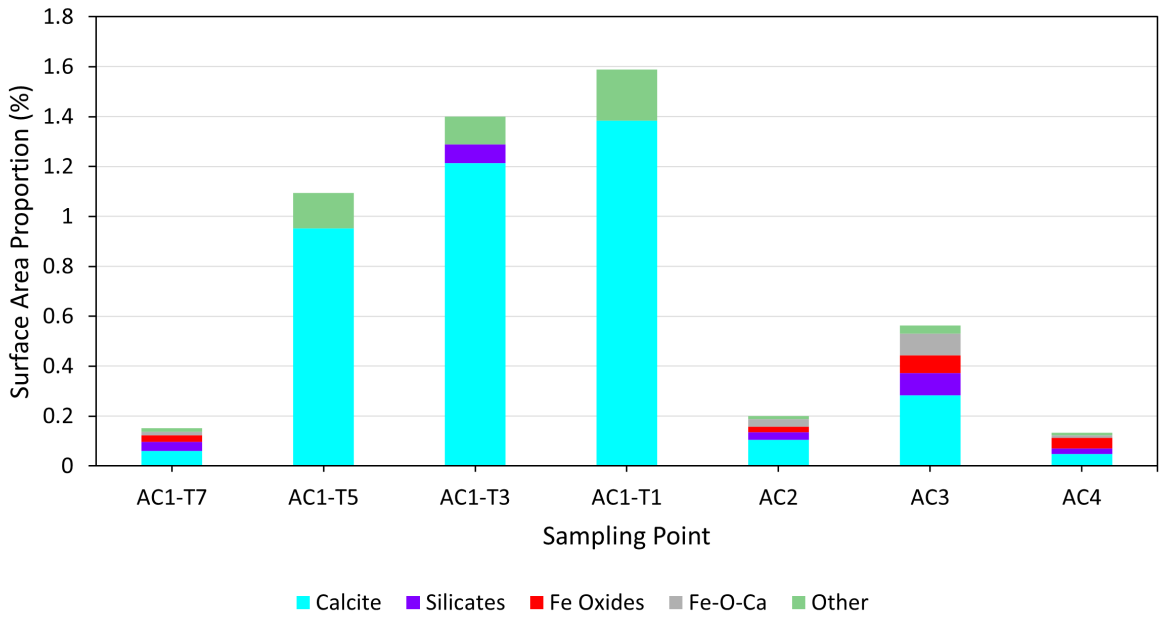


Figure 20. Inorganic fouling proportions expressed as % of the surface area of the entire carbon particle. Minerals representing < 5 % of the total inorganic fouling are grouped in "Other".

Table 5. Proportions of mineral phases by surface area relative to the total carbon particle surface area across sampling points. Minerals with proportions < 0.01 % are not shown.

| Classification category | Surface area proportions (%) across sampling points | | | | | | |
|---|---|---|---|---|---|---|---|
| | AC1-T7 | AC1-T5 | AC1-T3 | AC1-T1 | AC2 | AC3 | AC4 |
| Calcite | 0.061 | 0.952 | 1.213 | 1.383 | 0.105 | 0.283 | 0.049 |
| Silicates | 0.035 | 0.048 | 0.075 | 0.071 | 0.031 | 0.089 | 0.022 |
| Fe-O-Ca | 0.015 | 0.016 | 0.026 | 0.036 | 0.031 | 0.089 | 0.011 |
| Fe Oxides | 0.027 | 0.025 | 0.031 | 0.031 | 0.022 | 0.070 | 0.042 |
| Apatite | - | 0.024 | 0.022 | 0.020 | 0.011 | - | - |
| Quartz | 0.012 | 0.010 | 0.016 | 0.019 | - | 0.019 | - |
| Chalcocite | - | - | - | 0.012 | - | - | - |
| Pyrrhotite | - | 0.012 | 0.011 | - | - | - | - |

Apatite, quartz, chalcocite and pyrrhotite were partially detected at levels above 0.01 %, while all other mineral phases remained consistently below this threshold.

IF content was drastically reduced from 1.59 to 0.20 % after AW, indicating successful removal of IF phases from the carbon. Apart from barite, AW reduced all mineral contents on the GAC. The largest removal (> 90 %) was observed for AgS-Cu>10%, AgS, chalcocite, calcite and AgS-Cu<10%, followed by gypsum, sphalerite, pyrite and ankerite (70–88 %). Quartz and silicate contents were decreased by 62 % and 56 %, respectively, while iron oxides and Fe-O-Ca mixels showed only little removal (27 % and 16 %). Titanium oxide decreased negligibly (2 %), whereas barite content increased by 201 %.

Using SEM-AM it was possible to show the predominance of calcite as primary IF agent, as can be seen in Figure 22. Specific modes of occurrence are explained in the following section.

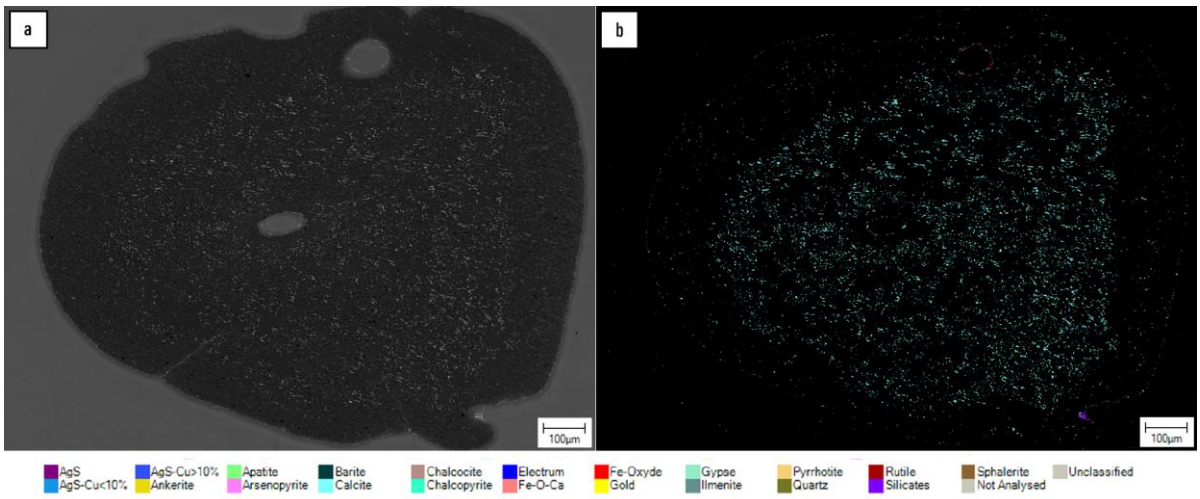


Figure 21. Backscattered electron (a) and false-color mineral classification (b) images of a carbon particle from sample AC1-T1, showing calcite as dominating inorganic contaminant.

### 4.5.4 Inorganic Fouling Types

SEM-AM revealed different types of IF on the GAC particles. To better characterize the IF within the GAC porosity, macropores are distinguished as macropores type A (50 nm – 30 µm) and B (> 30 µm). The majority of calcite, the most abundant foulant, was present as finely-crystalline particles filling macropores type A, as seen in Figure 32a–b in Appendix A. Apart from that, calcite was also found filling cracks within the GAC particles (Figure 32c–d), coating the external surfaces of GAC particles (Figure 32e–f) and occluding other mineral grains (Figure 32g–h).

In addition to calcite, the external surfaces of GAC particles were also found to be coated with either a heterogeneous mixture of minerals of varying grain sizes (1 – 40 µm) or with a fine-grained (< 5 µm) homogeneous layer of iron oxides (Figure 23).

Macropores type B also showed minor accumulations of calcite but were mostly filled with a heterogeneous mixture of all other mineral groups, mostly silicates and iron oxides, in two modes of occurrence. Correspondingly, mineral mixtures either completely filled out the carbon pore or were attached to the pore walls (Figure 24).

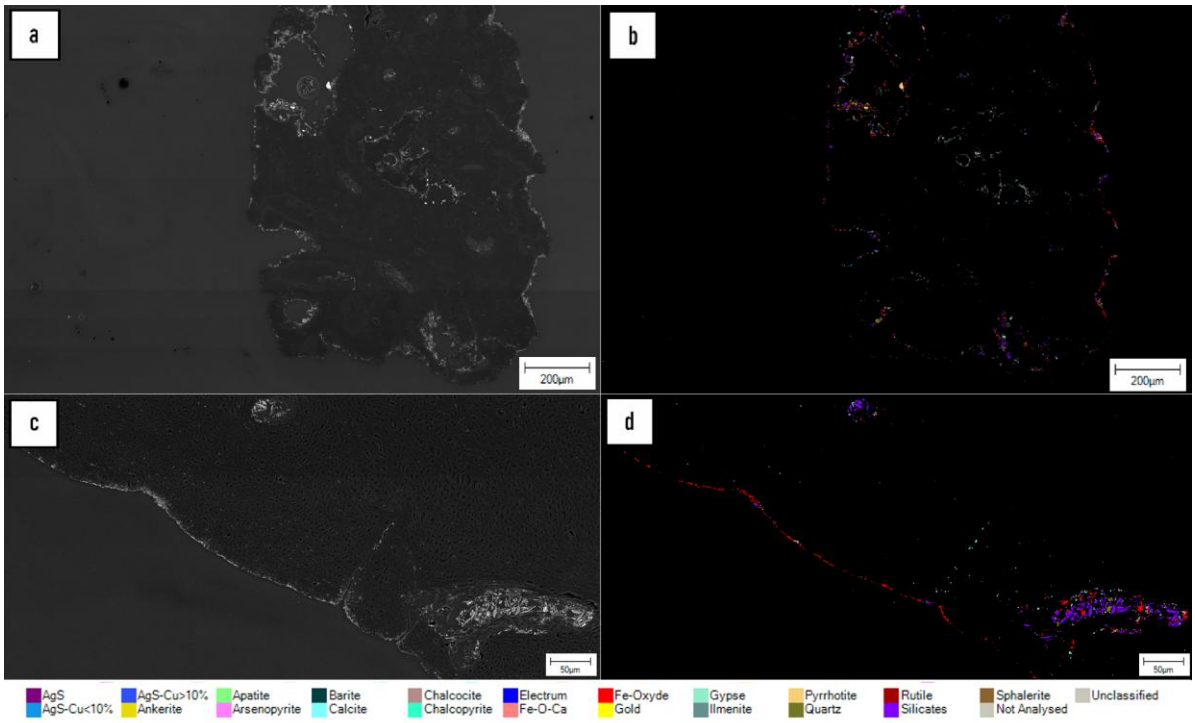


Figure 22. Backscattered electron and false-color mineral classification images showing mineral grains on the external surface of carbon particles from sample AC3: (a) a heterogeneous assemblage of various minerals, (b) a mostly homogeneous layer of iron oxide.

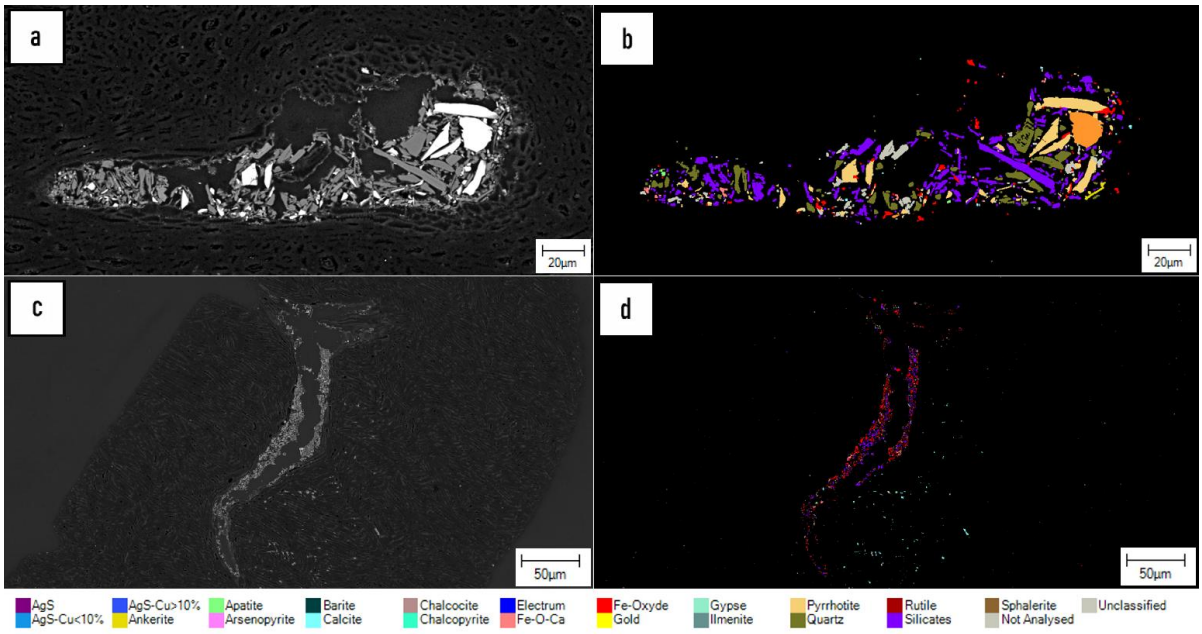


Figure 23. Backscattered electron and false-color mineral classification images of a mixture of minerals within macropores type B (> 30 µm) in two modes of occurrence: (a-b) either completely filling the pore (sample AC1-T7), or (c-d) being attached to the pore walls (sample AC4).

## 4.6 Data Reconciliation

### 4.6.1 Element Grouping for Reconciliation

Data reconciliation was done using the calculated wt.% of elements from the mineralogical data provided by the SEM as well as elemental data from ICP-OES. Elements used for data reconciliation depict Ca, S, Na, Fe, Zn, Mg and Al, since these were the main elements detected by chemical assay and therefore presumably constitute the majority of IF. Element contents were compared based on two criteria: quantitatively and in terms of variation trends between sampling points.

*Element Grouping Based on Quantitative Discrepancy*

Comparing chemical assays obtained by ICP-OES with elemental backcalculations from SEM generally revealed substantial discrepancies in measured contents. Accordingly, ICP-OES values exceeded those from SEM backcalculation in almost all samples and for most elements. For the interpretation of the reconciliation discrepancy, elements were first categorized into two groups based on the magnitude of the discrepancy.

Group 1 elements included Ca, Fe, Mg and Al and showed moderate discrepancies, with ICP-OES contents being between 0.3 to 6 times higher than backcalculated values from SEM (Figure 25). In contrast, elements of group 2 (Na, S and Zn) exhibited large discrepancies,

where ICP-OES contents exceeded SEM backcalculated values by more than a factor of 6 and in some cases even more than 100. For sodium in particular, discrepancies were orders of magnitude across all sampling points, with ICP-OES values reaching up to 465 times those backcalculated from SEM.

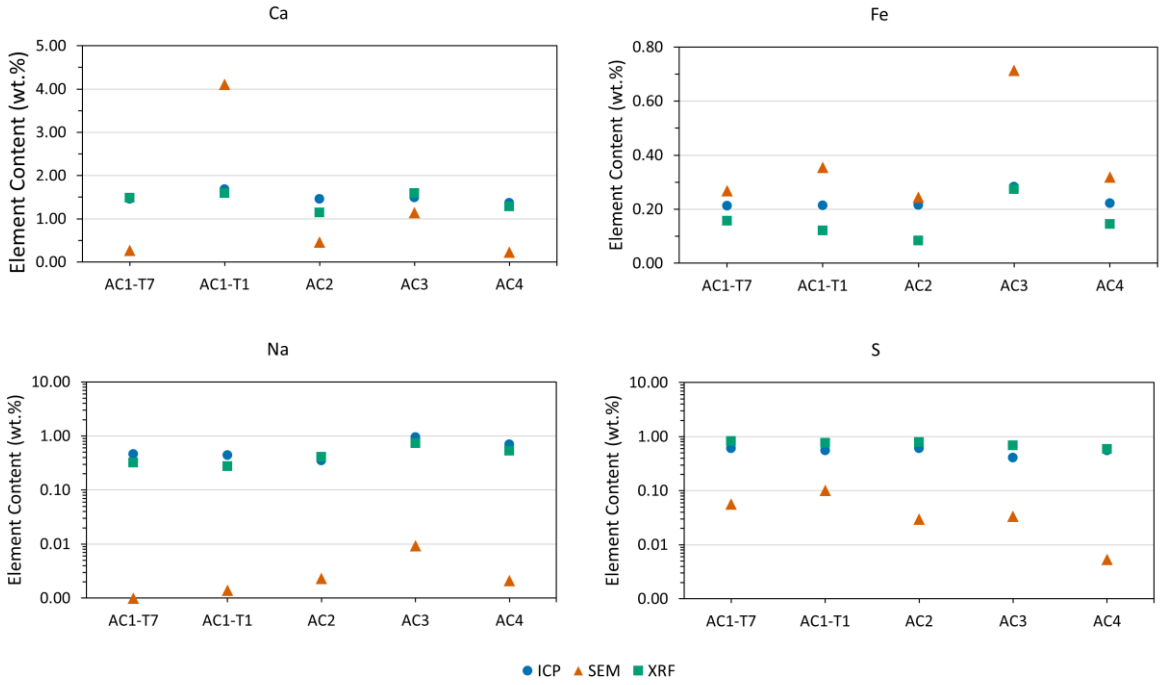


Figure 24. Ca, Fe, Na and S contents (wt.%) of activated carbon from several sampling points as determined by ICP-OES, XRF and SEM backcalculation. Note that the y-axis for Na and S is logarithmic. Abbreviations: ICP-OES = inductively coupled plasma optical emission spectroscopy; SEM = scanning electron microscopy; XRF = X-ray fluorescence.

*Element Grouping Based on Correlation*

To evaluate whether the ICP-OES and SEM measurements captured similar spatial trends across sampling points, Pearson correlation coefficients were calculated for each element, resulting in two general correlation patterns. Elements of the first group included Ca, Fe, Mg, Al and Na and revealed a strong positive Pearson correlation with $r > 0.85$ with the exception of Al ($r = 0.73$). Correlations were especially strong for Ca and Fe ($r > 0.95$), suggesting that ICP-OES and SEM measurements captured the same spatial variation of these elements. However, elements of the second group (S and Zn) showed weak correlations with $r < 0.2$, indicating inconsistent trends between both methods.

Finally, based on the two criteria, elements were separated into two groups: (1) Ca, Fe, Mg and Al, showing moderate discrepancies and good Pearson correlation; (2) Na, S and Zn, demonstrating high discrepancies and weak Pearson correlation. Despite sodium showing a

strong Pearson correlation (r = 0.85), it was grouped with sulfur and zinc as a result of its extreme quantitative discrepancies. In fact, the magnitude of discrepancy was prioritized over Pearson correlation during grouping, as it was considered to be more relevant for data reconciliation than the correlation.

### 4.6.2 ICP-OES Validation

Overall, ICP-OES values were well above the detection limit for the main elements investigated. To verify the validity of the ICP-OES assays, samples also underwent XRF analysis. Table 6 shows a comparison between ICP-OES and XRF assays (wt.%) for major elements present across sampling points. Although some variation between the two data sets can be seen, especially for aluminum, general trends and magnitudes of contents are shared between the two assaying methods. Accordingly, calcium as the main contaminant phase shows generally good agreement ranging from 1.14 to 1.68 % for both methods across all sampling points. Similarly, all other elements show relatively small discrepancies, when compared to the SEM backcalculation, suggesting that XRF confirms the observations by ICP-OES. Consequently, ICP-OES values will be further used for data reconciliation.

Table 6. Comparison of major element contents present in activated carbon samples obtained by ICP-OES and XRF across sampling points. Abbreviations: ICP-OES = inductively coupled plasma optical emission spectroscopy; XRF = X-ray fluorescence.

| Sample ID | AC1-T7 | | AC1-T1 | | AC2 | | AC3 | | AC4 | |
|---|---|---|---|---|---|---|---|---|---|---|
| Element (wt.%) | ICP-OES | XRF | ICP-OES | XRF | ICP-OES | XRF | ICP-OES | XRF | ICP-OES | XRF |
| Al | 0.019 | 0.064 | 0.024 | 0.052 | 0.021 | 0.059 | 0.022 | 0.073 | 0.017 | 0.044 |
| Ca | 1.460 | 1.480 | 1.680 | 1.590 | 1.460 | 1.140 | 1.490 | 1.590 | 1.370 | 1.280 |
| Fe | 0.213 | 0.158 | 0.214 | 0.121 | 0.217 | 0.085 | 0.283 | 0.274 | 0.222 | 0.146 |
| Mg | 0.024 | 0.035 | 0.032 | 0.031 | 0.021 | - | 0.041 | 0.051 | 0.030 | 0.044 |
| Na | 0.465 | 0.322 | 0.438 | 0.274 | 0.353 | 0.407 | 0.953 | 0.727 | 0.701 | 0.533 |
| S | 0.610 | 0.824 | 0.550 | 0.765 | 0.610 | 0.788 | 0.410 | 0.684 | 0.550 | 0.589 |
| Zn | 0.066 | 0.093 | 0.054 | 0.094 | 0.050 | 0.051 | 0.048 | 0.082 | 0.051 | 0.071 |

## 4.7 Illustration of Heterogeneity Approach

As described earlier, data limitations arising from the acquisition of all PBs in a single run without isolating mineralogical data for each GAC particle prevented implementation of the proposed theoretical approach for the determination of a minimum sample size. However, based on the data available, mineral-grain bootstrapping instead of GAC-particle bootstrapping was performed. While this does not capture the inter-particle variability between GAC particles, it provides an illustrative example for the proposed approach.

Results of the $RMSE_n^{proportion}$ calculations are provided in Figure 26, showing the RMSE as a function of the number of bootstrapped mineral grains, starting from 5,000 grains and increasing incrementally by 5 grains until the maximum number of grains is reached.

The data trends in the plots demonstrate a general decrease of the RMSE with increasing number of mineral grains, beginning to plateau at approximately 20,000 to 25,000 grains. The initial steep decline indicates that each additional grain adds a lot of new information to the bootstrapped subset. As the sample size increases further, the curves start to plateau, suggesting diminishing returns in new data. The resulting inflection point of the curve thus serves as a good indicator for the optimal minimum sample size, enabling the reduction of analysis time and costs while maintaining statistical accuracy – if confirmed using the confidence intervals.

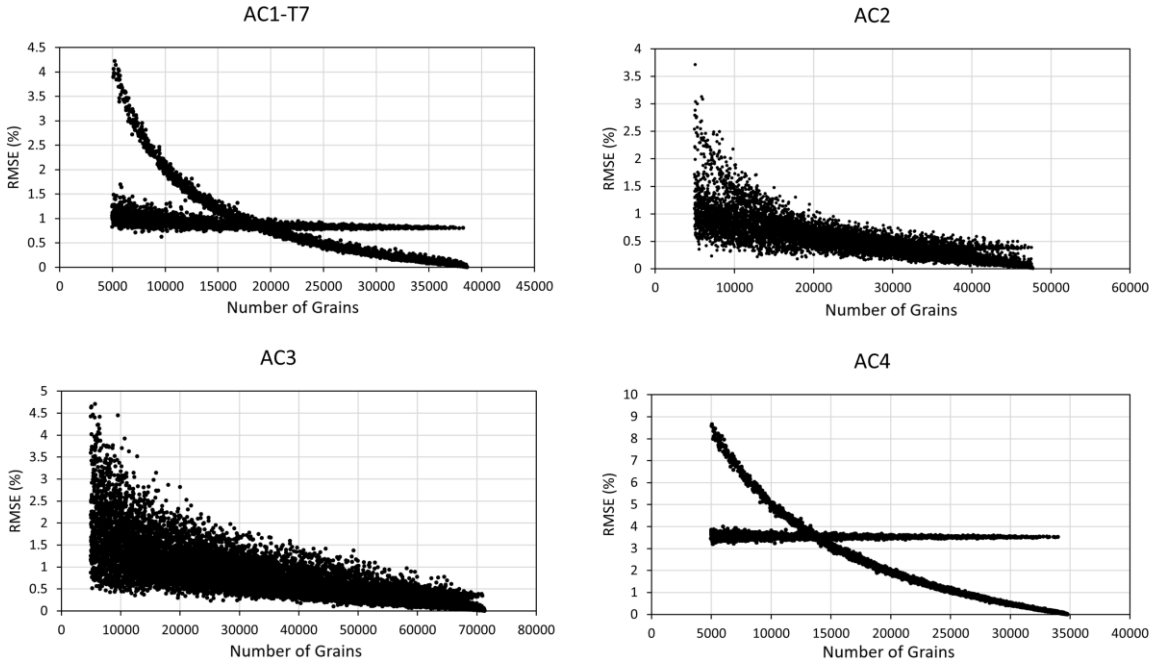


Figure 25. Root mean square error of mineral proportions between the bootstrapped subsets and reference data as a function of the number of bootstrapped mineral grains for the samples AC1 -T7, AC2, AC3 and AC4. The plots serve as illustrative examples for the methodological determination of a minimum sample size. Note: For true inter-particle heterogeneity, the x-axis should display the number of bootstrapped carbon particles, each with their respective mineralogical data.

# 5. Discussion

## 5.1 Inorganic Fouling Nature and Extent

### 5.1.1 Mineral Sources

*Carbonate and Sulfate Precipitates*

Calcite was by far the most common contaminant and made up the majority of IF across all sampling points, which is in general agreement with the literature (Davidson et al., 1979; Davidson & Sole, 2007; Macrae et al., 1988; Marsden & House, 2006). The formation of calcite in CIP gold recovery circuits is almost exclusively linked to the use of lime, as described in Eq. (4)–(6). At the LaRonde mill, lime is used in the CIP tanks to elevate the pH to 10.75, favoring the formation of calcite as described by the equations. Other salt precipitates and sulfates found in the literature include gypsum, magnesium and sodium salts (Macrae et al., 1988; Marsden & House, 2006). However, apart from gypsum, ankerite as well as barite, none of the mentioned phases could be classified in this study due to a lack of mineral classification categories.

*Silicates and Quartz*

Silicates were the second most abundant inorganic foulants, however, occurring to a far lesser extent than calcite. Several sources state, that fine silica particles, complex silicates, quartz, clays as well as clay-forming minerals may be physically trapped inside the carbon porosity, occluded or adsorbed on the GAC surface (Davidson & Tumility, 1985; Department of Education, Science and Training, Australia, 2005; Marsden & House, 2006; Rogans, 2017). Other sources state that silica found on GAC often depicts a mixture of quartz derived from the ore and silica precipitated from the solution (Macrae et al., 1988; Rogans, 2017; Smith et al., 1984). According to the technical report of the LaRonde mill, quartz is present in the ore mineralogy as well as host rocks (e.g., in felsic porphyritic rhyodacite to rhyolitic flows, breccias, tuffs and quartz-tourmaline-pyrite-pyrrhotite veins). Furthermore, host rocks and mineralization zones are partially silicified or sericitized, introducing the silicates into the circuit (Pitre et al., 2023).

*Iron and Iron Oxides*

Being the third most abundant mineral found constituting the IF, iron oxides make up between 0.02 to 0.07 % of the total surface area of the GAC particle. According to Marsden & House (2006), fine iron particles as well as products of the breakdown of grinding media are

commonly found as inorganic foulants. Similarly, Macrae et al. (1988) observed a grain largely composed of iron and manganese that was believed to originate from grinding media, as well as hematite introduced as inorganic foulant from the ore. Rogans (2017) reported hematite and goethite as adsorbed or in scale occluded colloids. In this study, iron oxides were found throughout all samples, possibly originating from the oxidation of iron-bearing sulfide minerals (e.g., pyrite, pyrrhotite) and subsequent precipitation. Additional hematization alteration of mineralized zones could increase the input of iron into the circuit (Pitre et al., 2023). The detection and classification of grains as "Fe > 90 wt.%" suggests that particles from the breakdown of grinding media or equipment wear were also present and adsorbed, occluded or trapped in the GAC at the LaRonde circuit.

*Others*

Apart from carbonates, sulfates, silicates and iron oxides, a wide variety of sulfides and titanium oxides was found contributing to the IF. These mineral phases likely originate directly from the ground ore, given the wide range of minerals and the blending of different ores at the LaRonde mill (Pitre et al., 2023). Macrae et al. (1988) as well as Smith et al. (1984) observed sulfide minerals at the external surfaces of the GAC. Similar observations were made during this study, showing sulfide minerals on external surfaces of the GAC particle as well as inside large macropores. Additionally, Macrae et al. (1988) noticed the presence of xenotime ($YPO_4$) and monazite ($(Ca,La,Th)PO_4$) on the surface of the carbon, attributing their origin to the ore being treated. While in this study, sulfides and titanium oxides are likely introduced from the ore, the technical report does not state any occurrence of phosphate minerals in the host rock of mineralized zones. However, during the preceding flotation of copper minerals, Aerophine – a dithiophosphinate collector reagent – is added to the system. It is assumed that using Aerophine enough phosphorus is introduced into the system and that mineral grains classified as "Apatite" actually represent phosphate precipitations.

### 5.1.2 Influence of Process Parameters on Fouling Characteristics

Apart from ore mineralogy, process parameters and changing chemical environments throughout the circuit largely influence the formation, destruction and properties of IF. The following chapter examines the effect of process conditions present at LaRonde on the IF characteristics observed in this study.

*CIP Adsorption Tanks*

Residence time of GAC inside a CIP adsorption tank ranged from 12 to 14 h, with lime additions of 0.91 kg/t ore. These conditions provide enough time and calcium for the formation and deposition of calcite, with the carbon surface acting as a catalyst and the alkaline pH (~10.5) stabilizing anions in solution (Rogans, 2017). Consequently, this study agrees that longer residence times in CIP adsorption tanks contribute to a cumulative build-up of IF, as presented by the increasing IF content over time. In addition to calcite, other inorganic species accumulated on the carbon, either through adsorption, precipitation, physical entrapment or occlusion by existing scale (van Vliet, 1991).

*Acid Wash*

AW conditions used at LaRonde are relatively mild compared to the literature, using 3 % HCl and a soaking time of 330 min. Nevertheless, AW removed the majority of IF, being most effective in the removal of sulfides, sulfates and carbonates, while iron oxide and especially titanium oxide removal rates were considerably lower. The removal of 92 % of calcite, as suggested by the SEM-AM, is in good agreement with calcite removal rates reported in the literature (Forson et al., 2018). The reaction proposed for the dissolution of calcite is presented in Eq. (8.

Although Rogans (2017) stated that calcium sulfate is difficult to remove using acid, the removal of gypsum was relatively successful in this study (88%). Iron oxides showed minor removal rates (27 %) as a result of AW. Smith et al. (1984) observed the removal of iron from carbon using 10 % HCl, while van Vliet (1991) reported that the use of hot dilute HCl (90 °C) removes large portions of iron and silica. Unfortunately, the temperature used for AW at LaRonde is unknown. Dissolution of iron oxides is likely due to protonation and surface complexation, which are enhanced by chloride ions forming Fe–Cl surface complexes that weaken iron–oxygen bonds (Sidhu et al., 1981).

No information was found in the literature on the removal of sulfide minerals from GAC during AW. However, it is reported that under the presence of an oxidizing agent such as $MnO_2$, cyclic redox actions and galvanic interactions can dissolve sulfide minerals. Considering the low amount of manganese present, it is assumed that sulfide minerals were simply flushed out of the carbon porosity by the acid solution and rinsing water. Similarly, quartz and silicates are believed to be mostly flushed out of the carbon porosity, as they represent highly insoluble species.

No substantial removal was observed for Ti oxides from the carbon. Under the AW conditions used, Ti oxides are more likely to precipitate as insoluble phases rather than dissolve (Lee & Yang, 2005; Mahmoud et al., 2004). Consequently, and considering their stable content, it is assumed that Ti oxides were also not flushed out during AW.

*Elution*

Following AW, rinsing water is used to flush away remaining impurities and acid from the GAC particles. During this process, the pH in the column is neutralized and the vessel is filled with NaOH to strip the adsorbed gold from the carbon under alkaline conditions.

Considering the high ionic strength of the PW used to rinse the GAC particles after AW, along with the changing pH, it is assumed that IF re-precipitated and began to accumulate again on the carbon. This could explain the observed increase in IF content at AC3.

IF phases that increased most during the transition from AC2 to AC3 include gypsum (8.7x), AgS-Cu<10% (8.7x) and Fe>90wt.% (4.2x). Additionally, ankerite and chalcopyrite contents increased by factors of 4 and 3, respectively. The major IF phases, i.e., calcite, iron oxides, silicates, Fe-O-Ca and quartz, increased by 1.6 to 2.2 times compared to AC2.

SEM-AM of sample AC3 revealed the presence of a fine-grained, homogeneous layer of iron oxides (Figure 23c–d), which was not observed in other samples. It is assumed that fine iron particles present in the PW adsorbed or precipitated onto the external surface of the GAC particles during the rinsing step as a result of the changing pH conditions.

*Thermal Regeneration*

TR is performed to remove accumulated OF from the GAC at elevated temperatures. At LaRonde, TR is conducted in a rotary kiln at temperatures between 650–750 °C.

Based on the mineralogical data from SEM-AM, the IF content decreased across all mineral phases during the transition from AC3 to AC4, with the total IF content dropping from 0.56 % to 0.13 %, respectively. Mineral phases that showed the largest decrease were pyrite, pyrrhotite and gypsum, each decreasing by 90–100%. This was followed by Fe-O-Ca, AgS-Cu<10%, AgS-Cu>10%, calcite, chalcocite, ankerite and quartz, which decreased by 80–88 %.

Several authors reported a reduction in ash content of the carbon due to the use of TR (Department of Education, Science and Training, Australia, 2005; Faulkner et al., 1987; Urbanic et al., 1985). At these temperatures, TR not only removes OF but can also result in the partial decomposition of IF, most notably calcium carbonate (Fisher & Dunn, 2000).

Accordingly, calcium carbonate decomposition starts at 600–700 °C, showing a significant weight loss at 700–750 °C (Urbanic et al., 1985).

The literature indicates that dehydration of gypsum starts at approximately 115 °C and that complete conversion to anhydrous calcium sulfate at 400 °C, explaining why gypsum was no longer detected by the SEM (Paulik et al., 1992). Similarly, it is believed that other mineral phases underwent thermal decomposition or transformation into different mineral forms, leading to their reduced detection by SEM. For instance, van Vliet (1991) reported the formation of refractory crystalline or sintered silicates on the carbon surface as a result of thermal regeneration, likely explaining the decrease in quartz and silicate content.

Faulkner et al. (1987) further highlighted the fact that the use of impure quench water can lead to renewed IF formation on GAC after TR. Interestingly, in this study, quenching of the thermally regenerated carbon did not result in a visible increase in IF content, despite the high ionic strength of the PW.

## 5.2 PW Composition

Elemental analysis of the PW revealed a large abundance of ionic species, especially sodium and sulfur. Elevated sodium contents are believed to originate from the use of caustic soda during the elution of aurocyanide from the GAC particles. In addition, high sulfur levels are presumed to be a result of the oxidation of sulfide minerals and the use of flotation reagents such as zinc sulfate ($ZnSO_4$) and copper sulfate ($CuSO_4$). Chloride and thiocyanate were the third and fourth most abundant species, likely resulting from the use of HCl during AW and the addition and degradation of cyanide in the CIP tanks, respectively.

The fact that the water sample was neither acidified nor analyzed immediately, but instead stored for several days, suggests that dissolved species may have precipitated prior to the chemical assay. This was visually confirmed by the presence of dark precipitates inside the PW sample container (Figure 27), which led to conclude that other dissolved species were present in the PW prior to precipitation. Based on predominance (Pourbaix) diagrams found in the literature, potential precipitates include iron (hydr)oxides and calcium phosphates, which would explain the low contents of Fe, Ca and P in final assay (Šimková, 2018; D. Wang et al., 2021).


Figure 26. Plastic bottle containing process water sampled from the quench water tank. The liquid clearly shows grey-black precipitations accumulating on the bottom of the container.

## 5.3 Reconciliation of Elemental Data

### 5.3.1 Theory on Reconciliation Discrepancy

All GAC samples obtained from the LaRonde circuit, except for the virgin carbon, were intensively washed using PW after sampling in order to remove residual pulp. It is supposed that during this procedure, dissolved species within the PW were deposited on the surface and within the porosity of the GAC particles. Since SEM-AM did not reveal sample contamination in terms of mineral grains across the samples, it is assumed that deposition occurred as ionic species or as finely crystalline phases below the detection limit of the SEM, being 1 µm at high magnification.

During the washing procedure with PW after sampling, GAC particles were still soaked, allowing all pores, even meso- and micropores, to be activated and accessible. This likely facilitated the intrusion of PW into the pore structure of carbon, leading to the deposition of dissolved species during the following drying phase. However, during the second washing step using demineralized water after drying overnight, carbon pores were deactivated. This presumably prevented the water to penetrate entirely into the GAC particle and thus limited the removal of the previously deposited phases.

As a result, ICP-OES, digesting and dissolving all material on and within the GAC particle, detected both IF mineral grains and species deposited from the PW. SEM-AM, however, only detected mineral particles above its detection limit, presumably missing the finely crystalline or ionic phases and resulting in the observed discrepancy. Moreover, for elements associated

with dominant IF minerals, e.g., calcium and iron, SEM captured their contribution properly and backcalculation reduced the elemental discrepancy for those elements.

### 5.3.2 Supporting Arguments

*Acid Wash Efficiency*

According to the ICP-OES data, AW at LaRonde removed ~0.2 % of calcium from the GAC, reducing its content from 1.68 % (AC1-T1) to 1.46 % (AC2). However, previous studies reported considerably greater calcium removal following AW, even under milder conditions. Accordingly, Smith et al. (1984) stated that AW with 5 % HCl reduced the calcium content from 4.70 % to 0.84 %. Similar observations were made by Davidson & Sole (2007), reducing the calcium content from 2.30 % to 0.12 %. Forson et al. (2018) reported 95 % Ca removal from GAC with initial calcium loadings below 2 % after 1 h of soaking with 3 % HCl.

Although AW at LaRonde is typically performed by soaking in 3 % HCl for 330 min, calcium content decreased only slightly as reported by ICP-OES. However, the proposed theory suggests not only the deposition of species after the second washing step but also the partial removal of calcite from the carbon particles. Thus, the calcium concentration prior to AW may have been higher and the extent of calcium removal during AW greater.

Overall, this supports the assertion that calcium, along with other species present in the PW, was both introduced to and partially removed from the carbon after sampling, due to decontamination and dissolution by the PW.

*Layered Calcite Distribution*

SEM imaging revealed distinct calcite distribution patterns in multiple GAC particles, showing an internal calcite-rich zone surrounded by a calcite-depleted outer zone. This pattern was seen across sampling points and is depicted in Figure 22. It is assumed that during the second washing step, demineralized water partially dissolved and removed calcite from the outer parts of the GAC particle. However, as the carbon pores were likely deactivated after drying, the water did not fully penetrate the GAC particles, resulting in the observed pattern. A thorough literature review revealed no previously reported observations of similar calcite distribution patterns inside GAC particles.

*Silicon as Reference Element*

XRF analysis not only confirmed ICP-OES-derived chemical assays but also provided the silicon content of GAC samples. In aqueous systems, silicon typically occurs as poorly soluble species, e.g. silica or silicates with a limited tendency to form dissolved ionic species. Based on these characteristics, it is assumed that major carbon contamination by silicon from the PW is unlikely. Hence, silicon represents a useful reference element for the investigation of the discrepancy between SEM-based backcalculation and chemical assay.

Comparison between SEM-based silicon backcalculation and corresponding XRF values can be seen in Figure 28. Backcalculation showed good agreement with XRF for the sampling points AC1-T1 and AC3 but was 2 to 3 times lower for AC1-T7, AC2 and AC4. Despite that, the overall Pearson correlation between both methods showed a strong correlation (r = 0.87), indicating that similar spatial trends of silicon were captured.

Given the overall low silicon content of the GAC samples and the XRF detection limit of 0.1 % for Si, it is likely that XRF was not able to accurately quantify silicon contents below this threshold. With the XRF detection limit explaining the discrepancies observed for AC1-T7, AC2 and AC4, the overall good agreement for silicon content supports the proposed theory.

*Element Contents in Literature*

To assess whether the SEM backcalculation and silicon content determined by XRF provided reasonable results, a comparison with published studies that quantified elemental contents on GAC particles will be presented in this chapter.

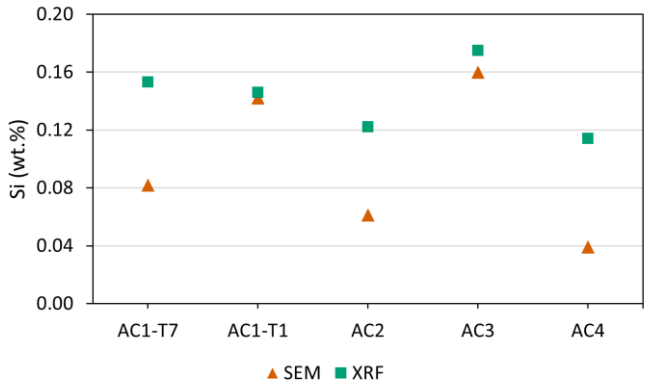


Figure 27. Comparison between SEM-based backcalculated and XRF-determined Si content of activated carbon from several sampling points. Abbreviations: SEM = scanning electron microscopy; XRF = X-ray fluorescence.

Davidson (1974) and Rogans (2017) reported calcium concentrations in the range of 0.5–3.0 %, being lower than the SEM-backcalculation of 4.1 % at AC1-T1 in this study. However, Davidson & Sole (2007) discussed the effects of calcium loadings as high as 6 %, indicating that backcalculated values may be plausible.

Davidson (1974) also investigated changes in elemental composition from original to loaded charcoal. A sharp decrease in sodium and potassium contents was observed, with sodium decreasing from 18,500 to 4,500 ppm and potassium from 10,400 to 1,900 ppm. A similar trend was noted in this study, albeit at lower contents, with sodium and potassium decreasing from 180 and 210 ppm in AC5 to 10–93 and 4–37 ppm, respectively, in the process carbon. For manganese, SEM-backcalculated values varied between 7–25 ppm, aligning with the 25 ppm observed by the author. That study also reported a silicon content of 0.03 % on loaded charcoal, which is moderately lower than the silicon content observed in this study, ranging between 0.11–0.18 %.

Regarding iron, Smith et al. (1984) reported loadings of up to 0.92 %, which is relatively close to the 0.73 % observed in this study for sample AC3. In the study by Davidson (1974), iron content did not change from the original to the loaded charcoal, with contents remaining at 0.15 %.

Overall, considering the significant influence of ore mineralogy and processing parameters on the elemental composition of IF on GAC, the variations between SEM-backcalculated values and those reported in the literature are plausible. This consistency further supports the reliability of the backcalculated values in this study.

*Virgin Carbon Composition after Washing*

In order to confirm whether PW introduced contamination into the GAC particles, virgin carbon was first washed with PW and then with demineralized water. XRF analysis of the washed virgin carbon revealed the presence of mostly K (0.47 %), silicon (0.27 %), Ca (0.16 %), S (0.14 %), Na (0.09 %) and Fe (0.09 %). Comparison of these results with the elemental composition of unwashed virgin carbon obtained using ICP-OES (Table 3) revealed that K, Ca, S and Na contents were considerably after washing, while iron content was notably lower. Although the elemental composition of the washed virgin carbon differed substantially from that of the process carbon, the considerable increase in K, Ca, S and Na strongly suggests that contamination by PW is likely. Additionally, the carbon pores of the process carbon were activated during washing with PW. It is presumed that the virgin carbon was sampled dry from

storage bags and washed immediately, which likely prevented activation of carbon pores and therefore less penetration and contamination by the PW.

### 5.3.3 Counterarguments

*Acid Washing Curve*

Although Forson et al. (2018) reported high calcium removal using 3 % HCl, Figure 29 from Marsden & House (2006) shows that under certain operational conditions, calcium removal may plateau at ~1.5 %. Accordingly, this is likely to happen using 3 % HCl, as is the case at LaRonde. Unfortunately, the diagram does not include the 330 min soaking time used at the plant. However, assuming that the curve continues plateauing, the observed ICP-OES calcium contents of the GAC samples might just reflect true limitations of the AW process rather than sample contamination by the PW.

### 5.3.4 Other Factors

*Unclassified Grains*

Unclassified grains represent those grains that could not be assigned to a designated mineral classification category as defined by the mineral classification rules. Due to their unknown nature and the resulting lack of mineral density required for the calculations, unclassified grains were excluded from the investigation. Although the classification rules were previously refined to reduce the number of unclassified grains, mineralogical data from SEM-AM showed that

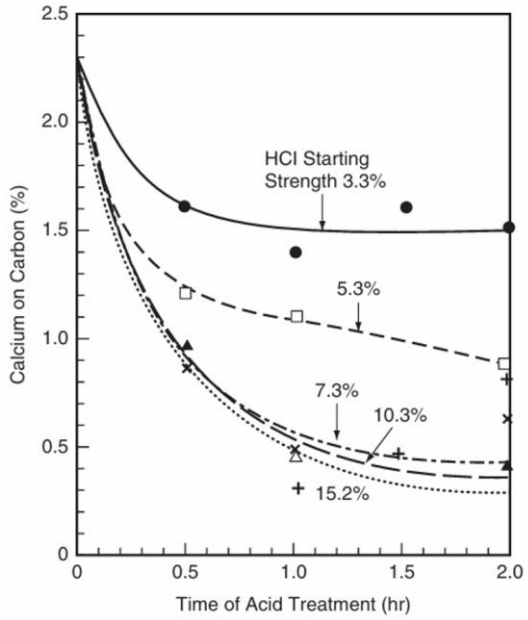


Figure 28. Residual calcium content on carbon according to HCl strength and duration of treatment. Source: Marsden & House (2006).

this fraction contributed between 10.0 % (AC1-T1) and 36.8 % (AC4) of the total analyzed grain area across all samples.

In order to investigate the nature of the unclassified grains, their average elemental composition was calculated. No matrix refinement was used for the calculation since element attribution was not feasible for the unclassified category.

Unclassified grains were primarily composed of Ca (43.4 %), Ag (17.27 %), O (8.5 %), Fe (7.9 %) and S (6.5 %). Given the high calcium content, it is assumed that the majority of unclassified grains were calcite and not classified as such due to e.g., insufficient oxygen content required for identification. On the other hand, calcium could also stem from a mineral not listed in the mineral categories or a non-mineral form, such as an amorphous coating. The presence of calcium as an amorphous-like coating was reported by Macrae et al. (1988). The silver content likely originated from the silver metallization of the PBs, as ~30 % of all analyzed grains showed some presence of silver – leading to the application of the matrix refinement in the first place. Based on the presence of iron and sulfur, the unclassified fraction may also include iron oxides, sulfides, gypsum, or other minerals not included in the classification scheme.

Accordingly, it is assumed that the exclusion of unclassified grains during SEM-based backcalculation underestimated calcium, as well as other elements, thereby further contributing to the reconciliation discrepancy in addition to the contamination introduced by the PW.

*Calculation Parameters*

Additional factors potentially contributing to the reconciliation discrepancy include the bulk densities of minerals, the estimation of the GAC particles surface area and the matrix refinement.

Calculating the average density of the entire IF requires knowledge of the individual mineral densities. In this study, densities were assigned to each mineral category, assuming that the minerals occur crystalline form and exhibit average densities as found at *WebMineral.com.* Furthermore, for grains categorized as mixels non-mineral phases, precise densities are difficult to determine and were therefore approximated.

Accurate estimation of the GAC particles' surface area is crucial in order to determine the IF content relative to the carbon. Outlining the entire carbon particle and applying the average bulk density of GAC is intended to approximate the pore distribution. However, this approach

relies on the assumption that the carbon particles actually exhibit the expected pore structure projected by the bulk density.

Finally, element contents derived from the EDS spectra were refined using the matrix refinement, which is based on a closed normalization. Accordingly, all elements contributing to the mineral composition are summed and each element is divided by this total. The matrix itself was constructed based on mineralogical information acquired from the WebMineral database as well as expertise from the academic supervisor. While this approach offers a mathematical consistent normalization and provides an approximation of the mineral composition, it may not accurately reflect the true stoichiometry of the minerals present.

*Sample Representativeness*

Lastly, the observed reconciliation discrepancy could also be a result of insufficient sample material analyzed by SEM-AM. Nevertheless, the variation in IF content across sampling points (Figure 21) aligns well with the expected trend of foulant accumulation over time and its partial removal during AW.

*Mineral Phase Dislodgement*

Investigation of the GAC surfaces using the SEM revealed few mineral accumulations with dislodged or missing parts, which likely hindered the detection of these IF grains during SEM acquisition. Based on EDS data, these accumulations were identified as calcite. It is assumed that parts of the calcite accumulations were removed from the GAC surface during polishing, leading to an underestimation of calcite during acquisition.

## 5.4 Effect of Inorganic Fouling on Gold Adsorption

The highest GAC activity was observed for carbon sampled from the first CIP adsorption tank, closely followed by carbon sampled after TR. In contrast, carbon from the final adsorption tank exhibited considerably lower activity, likely due to the progressive occupation of readily available adsorption sites by aurocyanide during the CIP process. Notably, AW did not appear to enhance gold adsorption efficiency, in fact, GAC from AC2 showed the lowest activity of all samples.

This observation contradicts findings in the literature, which suggests that IF, particularly calcium carbonate precipitations, accumulate within pores and hinder gold adsorption by blocking entrance ways for the pregnant solution (Macrae et al., 1988). Removal of such pore-

blocking mineral phases through AW is generally considered to restore carbon activity, however, this was not observed in this study.

Several studies reported that OF has detrimental effects on carbon activity by competing directly for gold adsorption sites and physically blocking access to the internal porosity (Faulkner et al., 1987; Fleming et al., 1984; Fleming & Nicol, 1984; La Brooy et al., 1986; Pleysier et al., 2008). Similar to the observed trend in SSA, the potential removal of parts of OF during elution likely contributed to the increase in carbon activity for GAC from AC3.

According to the literature, GAC from AC1-T1, being exposed to both OF and IF simultaneously, should exhibit the lowest activity. However, this was not supported by the data.

It is important to note that sampling was performed during a single operational cycle. Consequently, operational timing might have introduced variability, e.g., that after sampling from AC1-T1, the carbon remained in the slurry for an unknown period of time before being transferred into the AW column. During this time interval, gold adsorption continued, progressively saturating gold adsorption sites. This likely reduced the carbons activity further, contributing to the unexpectedly low activity observed in AC2.

## 5.5 Effects of Inorganic Fouling on Specific Surface Area

The SSA of the process carbon ranged from 334.1 to 557.5 $m^2 \cdot g^{-1}$. The observed SSA values were considerably lower than those reported in the literature for spent coconut shell GAC, which ranged from 790.0 to 1079.6 $m^2 \cdot g^{-1}$ (Cevallos Toledo et al., 2020; van Deventer & van der Merwe, 1994). For virgin carbon, SSA values between 921 and 1500 $m^2 \cdot g^{-1}$ have been documented, which was also higher than the 836.9 $m^2 \cdot g^{-1}$ measured for the virgin carbon used in this study (Choi, 2017; van Deventer & van der Merwe, 1994; Vegter et al., 1997). A possible explanation for this discrepancy could be the contamination of samples by PW. The deposition of finely crystalline phases may have clogged carbon micropores, thereby reducing BET adsorption capacity, especially considering that micropores can account for up to 95 % of the total porosity of GAC (Rogans, 2017).

Considering the large difference in SSA between process and virgin carbon, it can be assumed that carbon fouling considerably influenced the SSA of the GAC particles. This assumption is further supported by the observed decreasing trend in SSA across the sequential CIP adsorption tanks. Although IF was largely found clogging carbon pores, AW did not appear to affect the SSA. This could be attributed either to a predominant influence of OF in reducing the SSA,

potentially overshadowing the impact of IF, or to the possibility that IF has a minimal or negligible effect on the SSA of carbon particles.

The former assumption is supported by the increase in SSA observed after TR, which yielded the highest SSA among the process carbon samples. Additionally, a modest increase in SSA was observed between AC2 and AC3, which may be explained by the partial desorption of organic adsorbates, as suggested by van Vliet (1991).

Wang & Lu (1998) reported that AW led to the removal of inorganic constituents from GAC, increasing SSA and pore volume. However, using 2M HCl, the SSA increased only slightly from 972 to 1015 $m^2 \cdot g^{-1}$. Apart from this, no published studies were found that investigated the direct effects of IF and OF on the SSA of GAC.

## 5.6 Practical Applications

Considering the time required for the acquisition of a single PB, which varied between 20 to 40 h depending on the sampling point, the presented methodology is not suitable for real-time monitoring of GAC conditions. However, its value does not lie in addressing a malfunctioning system, considering that the LaRonde mill has been operating efficiently for many years. Rather, it lies in optimizing the AW process for site-specific conditions, as IF formation is strongly dependent on factors such as ore mineralogy, process parameters and operational design.

The application of SEM-AM provides the company with a powerful tool to evaluate the efficiency of AW conditions, potentially reducing time, reagent and water consumption as well as carbon wear. Whereas AW of GAC has traditionally been guided by empirical practices or literature recommendations, this methodology enables site-specific optimization by providing visual and quantitative insights into the fouling state of GAC particles.

Furthermore, given the limited literature available on the characterization of IF, the proposed methodology contributes to deepening the understanding of IF mechanisms throughout the processing circuit and their impact on gold recovery.

## 5.7 Improvements

Throughout the development of the proposed methodology, several improvements and modifications in sample preparation, as well as data acquisition and processing, were identified. These will be presented in the following chapter.

Most importantly, the washing of sampled carbon should be performed using demineralized or distilled water in order to eliminate any potential contamination introduced into the porosity. This would enable the verification of the presumed sample contamination observed in this study, as well as allow for more accurate data reconciliation with ICP-OES results. The sample preparation of PBs may be improved through gentler polishing, possibly reducing the amount of dislodged IF material and thereby enhancing the accuracy of backcalculation results.

The use of image analysis for the automated determination of the surface area of GAC particles was trialed for one sample and yielded good results. It is therefore recommended to use image analysis instead of manual segmentation, as it offers a more efficient and reproducible alternative.

In order to determine true inter-particle variability and establish a minimum number of GAC particles required for representative characterization of a carbon lot using the proposed theoretical approach on carbon heterogeneity, GAC particles embedded within PBs have to be analyzed individually. Performing SEM-AM on additional PBs, i.e., increasing the number of analyzed grains per sampling point represents another opportunity to assess the representativeness of GAC particles within PBs relative to the carbon lot. Additionally, any findings from the characterization of IF on GAC should be validated through multiple sampling campaigns to minimize sampling bias.

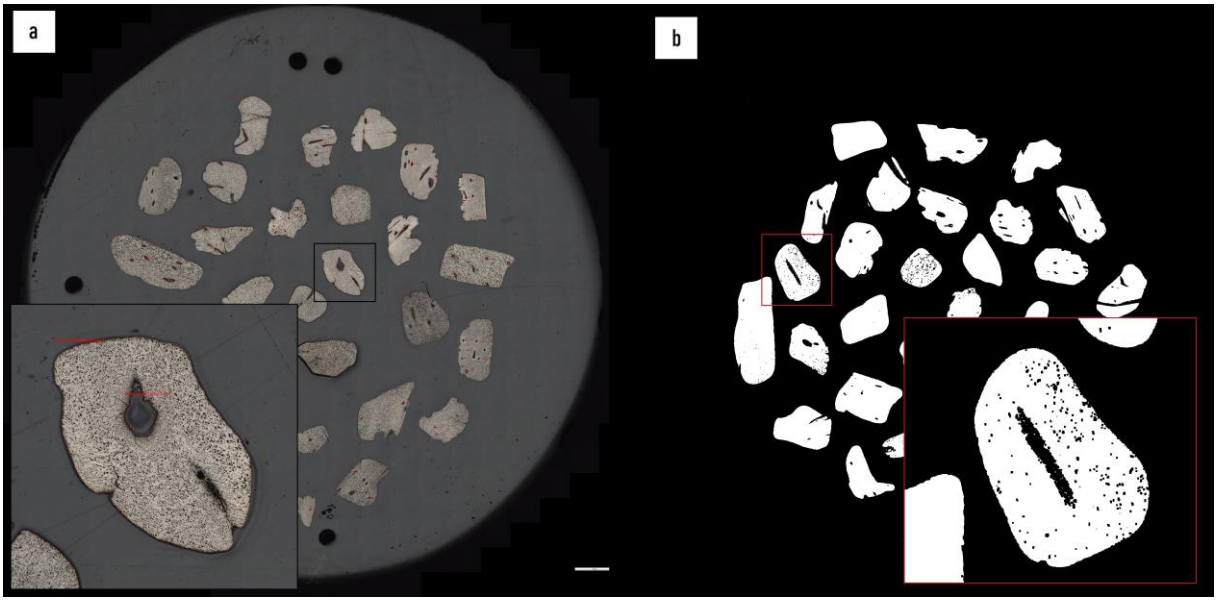


Figure 29. Surface area determination using: (a) manual polygonal segmentation; (b) binary masking and image analysis.

Mineralogical data obtained from SEM is only as reliable as the mineral classification rules used during acquisition. Integrating mineralogical information from deposit geology into the development of classification rules is crucial for reducing the number of unclassified grains and ensuring accurate data. Mineralogical insights from the deposit should also be used to refine the matrix used for the processing of mineralogical data sets from SEM. Moreover, investing time in the design of an appropriate image processing recipe prior to SEM-AM holds great potential for improving the differentiation of adjacent mineral phases, as well as distinguishing mineral phases from the carbon structure.

# 6. Conclusion

This study developed a robust methodology for the qualitative and quantitative characterization of IF on GAC using in gold recovery. A tailored protocol for PB preparation was established and PBs were successfully analyzed using SEM-AM. A comprehensive data processing workflow was presented, yielding reliable estimations of IF content across various points in the processing circuit. The variations in IF content observed in this study were effectively correlated with processing parameters and changing environmental conditions throughout the circuit. Additionally, a statistically sound approach was proposed to determine the minimum number of GAC particles required for statistically reliable characterization of the entire PB, enabling a significant reduction in analysis time and costs.

Data reconciliation was inconclusive, likely due to the contamination of GAC samples by PW. Potential causes and implications of this contamination were critically examined and supporting as well as opposing perspectives were presented. Apart from the methodology's direct practical applications for processing plants, several improvements were presented aiming to increase automation, analytical accuracy and efficiency.

Findings from literature suggest that high levels of IF, particularly calcite, may negatively impact carbon hardness (Macrae et al., 1988). Moreover, the discrepancies observed between carbon activity, IF removal trends and reported literature findings highlight the need for further investigations. The methodology developed in this study offers a novel approach for future research aimed at deepening the understanding of the effects of IF on carbon degradation and gold adsorption performance.

## 7. EIT Chapter

The transition from the Merrill-Crowe process to ADR circuits in the 1970s marked a major milestone in improving gold recovery. ADR circuits use, e.g., GAC to adsorb and recover gold from solution, an innovation that not only reduced capital and operating costs but introduced a gold processing route that is considerably more environmentally friendly (Kim et al., 2024).

Sustainability benefits of ADR circuits primarily include reduced chemical use by avoiding zinc dust and lead nitrate, minimized hazardous waste due to the elimination of zinc precipitate sludge and lower energy consumption as a result of lower operating temperatures. Furthermore, the gold recovery process in general is simplified, leading to a smaller plant footprint, and it utilizes a renewable and recyclable material for gold recovery – GAC.

While several types of activated carbon can be used for gold recovery, coconut shell-based GAC remains the most widely applied type (Faulkner et al., 1987). Compared to coal-based activated carbon, coconut shell GAC has a lower environmental impact. However, its production still has considerable drawbacks. On the one hand, it requires substantial amounts of electrical energy, while on the other hand, the pyrolysis step emits a series of gases and by-products, i.e. carbon dioxide and methane, carbon monoxide, volatile organic compounds as well as particulate matter. Considering that the energy mix of the main producing countries of coconut shell GAC, i.e., Indonesia, the Philippines and India, still rely heavily on hard coal, the environmental footprint of GAC production has to be considered (Arena et al., 2016; Saleem et al., 2025; Salunkhe et al., 2024).

Once applied by mining companies, GAC is regenerated and reused over many cycles, possibly more than 100 times, before being replaced with make-up carbon („Gold Recovery“, n.d.). At the LaRonde mill, 1 t new GAC is added to the circuit every week to cover up losses. Thus, GAC regeneration still requires the use of chemicals such as HCl or $HNO_3$ and consumes considerable energy amounts during thermal treatment in the rotary kiln.

To date, AW practices appear to be largely based on empirical rules and literature guidelines. Developing a method to quantitatively and visually assess the success of the regeneration process would close a gap in the current inability to accurately evaluate and optimize regeneration strategies.

In this study, such a methodology was developed, applied and assessed for its effectiveness. The approach enabled quantification and visualization of IF present on both external as well as internal surfaces of GAC particles. This allows processing plants to develop site-specific AW

protocols and fine-tune them in order to achieve optimal process conditions. Furthermore, the outcome of applying this methodology is the potential to reduce reagent and water consumption, shorter AW treatment time, decreased carbon degradation and minimized gold losses by ensuring that the GAC remains clean and active. Moreover, unnecessary AW cycles may be avoided, carbon make-up can be scheduled more precisely and general carbon consumption and thus operating costs can be reduced. This not only provides a more efficient process but also improves the environmental performance.

In summary, the methodology presented in this study not only contributes to the scientific understanding of IF on GAC but also offers a significant step forward in improving the efficiency and sustainability of gold recovery processes.

## References


Adams, M. D. (1989). *The chemistry of the carbon-in-pulp process* [University of the Witwatersrand]. http://hdl.handle.net/10539/15251

Ahmed, F. E., Young, B. D., & Bryson, A. W. (1992). Comparison and modelling of the adsorption kinetics of gold cyanide onto activated carbon and resin in a silica slurry. *Hydrometallurgy*, *30*(1), 257–275. https://doi.org/10.1016/0304-386X(92)90088-H

Arena, N., Lee, J., & Clift, R. (2016). Life Cycle Assessment of activated carbon production from coconut shells. *Journal of Cleaner Production*, *125*, 68–77. https://doi.org/10.1016/j.jclepro.2016.03.073

Blannin, R., Frenzel, M., Tuşa, L., Birtel, S., Ivăşcanu, P., Baker, T., & Gutzmer, J. (2021). Uncertainties in quantitative mineralogical studies using scanning electron microscope-based image analysis. *Minerals Engineering*, *167*, 106836. https://doi.org/10.1016/j.mineng.2021.106836

Bodländer, G. (1896). Die Chemie des Cyanidverfahrens. *Angewandte Chemie*, *9*(19), 583–587. https://doi.org/10.1002/ange.18960091903

Bouleghlimat, E., Davies, P. R., Davies, R. J., Howarth, R., Kulhavy, J., & Morgan, D. J. (2013). The effect of acid treatment on the surface chemistry and topography of graphite. *Carbon*, *61*, 124–133.

Budi, E., Nasbey, H., Yuniarti, B. D. P., Nurmayatri, Y., Fahdiana, J., & Budi, A. S. (2014). Pore structure of the activated coconut shell charcoal carbon. *AIP Conference Proceedings*, *1617*, 130–133. https://doi.org/10.1063/1.4897121

Cevallos Toledo, R. B., Aragón-Tobar, C. F., Gámez, S., & d. l. Torre, E. (2020). Reactivation Process of Activated Carbons: Effect on the Mechanical and Adsorptive Properties. *Molecules*, *25*(7), Article 7. https://doi.org/10.3390/molecules25071681

Choi, D. C., Ahmad Ghahreman, Yeonuk. (2017, Januar 1). *A Preliminary Comparison between a Granular Coconut Shell-Based Activated Carbon and Lewatit® AF 5 in the Application of Gold-Bearing Pyrite Oxidation in Acidic Ferric Sulphate Media*. OneMine. https://www.onetunnel.org/documents/a-preliminary-comparison-between-a-granular-coconut-shell-based-activated-carbon-and-lewatit-af-5-in-the-application-of-gold-bearing-pyrite-oxidation-in-acidic-ferric-sulphate-media

Cook, R., Crathorne, E. A., Monhemius, A. J., & Perry, D. L. (1989). An XPS study of the adsorption of gold (I) cyanide by carbons. *Hydrometallurgy*, *22*(1), 171–182. https://doi.org/10.1016/0304-386X(89)90048-0

Corti, C., & Holliday, R. (Hrsg.). (2009). *Gold: Science and Applications*. CRC Press. https://doi.org/10.1201/9781420065268

Creelman, R. A., & Ward, C. R. (1996). A scanning electron microscope method for automated, quantitative analysis of mineral matter in coal. *International Journal of Coal Geology*, *30*(3), 249–269. https://doi.org/10.1016/0166-5162(95)00043-7

Davidson, R. J. (1974). The mechanism of gold adsorption on activated charcoal. *Journal of the Southern African Institute of Mining and Metallurgy*, *75*(4), 67–76. https://doi.org/10.10520/AJA0038223X_513

Davidson, R. J., & Schmidt, C. G. (1986). A review of the AARL process for the elution of gold from activated carbon. *13th CMMI Congress Publications*, *Metallurgy*(4), 215–225.

Davidson, R. J., & Sole, M. J. (2007). The major role played by calcium in gold plant circuits. *Journal of the Southern African Institute of Mining and Metallurgy*, *107*, 463–468.

Davidson, R. J., & Tumility, J. A. (1985). *A Review of the AARL Process for the Elution of Gold from Activated Carbon*. Anglo American Research Laboratories.

Davidson, R. J., Veronese, V., & Nkosi, M. V. (1979). The use of activated carbon for the recovery of gold and silver from gold-plant solutions. *Journal of the Southern African Institute of Mining and Metallurgy*, *79*, 281–297.

de Andrade Lima, L. R. P. (2007). Dynamic simulation of the carbon-in-pulp and carbon-in-leach processes. *Brazilian Journal of Chemical Engineering*, *24*, 623–635. https://doi.org/10.1590/S0104-66322007000400014

Demiral, I., Samdan, C., & Demiral, H. (2021). Enrichment of the surface functional groups of activated carbon by modification method. *Surfaces and Interfaces*, *22*, 100873. https://doi.org/10.1016/j.surfin.2020.100873

Department of Education, Science and Training, Australia. (2005). *Metalliferous Mining – Processing: Elution & Carbon Reactivation Resource Book*. https://rsteyn.wordpress.com/wp-content/uploads/2010/07/elution-and-carbon-reactivation-basics.pdf

Elsner, L. (1846). Über das Verhalten verschiedener Metalle in einer wässrigen Lösung von Zyankalium. In *J. Prakt. Chem.* (S. 441–446).

Faulkner, W. D., Urbanic, J. E., & Ruckel, R. W. (1987). *Activated carbon for precious metal recovery*. https://p2infohouse.org/ref/33/32741.htm

Fisher, N. G., & Dunn, J. G. (2000). Identifying organic foulants on activated carbon from gold processing plants. *Minerals Engineering*, *13*(14), 1581–1588. https://doi.org/10.1016/S0892-6875(00)00141-2

Fleming, C. A., Mezei, A., Bourricaudy, E., Canizares, M., & Ashbury, M. (2011). Factors influencing the rate of gold cyanide leaching and adsorption on activated carbon, and their impact on the design of CIL and CIP circuits. *Minerals Engineering*, *24*(6), 484–494. https://doi.org/10.1016/j.mineng.2011.03.021

Fleming, C. A., & Nicol, M. (1984). The absorption of gold cyanide onto activated carbon. III. Factors influencing the rate of loading and the equilibrium capacity. *Journal of The South African Institute of Mining and Metallurgy*. https://www.semanticscholar.org/paper/The-absorption-of-gold-cyanide-onto-activated-III.-Fleming-Nicol/adc7e5f51445028c927880d3dc0479bbd58f9c5f

Fleming, C. A., Nicol, M. J., & Cromberge, G. (1984). The absorption of gold cyanide onto activated carbon. I. The kinetics of absorption from pulps. *Journal of the Southern African Institute of Mining and Metallurgy*, *84*(2), 50–54. https://doi.org/10.10520/AJA0038223X_1427

Forson, P., Adam, A.-S., & Ofori-Sarpong Akuffo, G. (2018). *Improving Acid Wash Efficiency of Loaded Activated Carbon in a Gold Desorption Circuit*.

Ganjoo, R., Sharma, S., Kumar, A., & Daouda, M. M. (2023). *Activated Carbon: Fundamentals, Classification, and Properties* (S. 1–22). https://doi.org/10.1039/BK9781839169861-00001

Ghasemi, S., Mohammadnejad, S., & Khalesi, M. R. (2018). A DFT study on the speciation of aqueous gold and copper cyanide complexes. *Computational and Theoretical Chemistry*, *1124*, 23–31. https://doi.org/10.1016/j.comptc.2017.12.004

Ghasemi, S., Mohammadnejad, S., & Khalesi, M. R. (2022). Role of Functional Groups in Selective Adsorption of Gold over Copper Cyano complexes by Activated Carbon: A DFT Study. *Journal of Mining and Environment*, *13*(3), 891–901. https://doi.org/10.22044/jme.2022.12125.2210

Gold Recovery. (n.d.). *Jacobi Group*. https://www.jacobi.net/gold-recovery/

Gönen, N., Körpe, E., Yıldırım, M. E., & Selengil, U. (2007). Leaching and CIL processes in gold recovery from refractory ore with thiourea solutions. *Minerals Engineering*, *20*(6), 559–565. https://doi.org/10.1016/j.mineng.2006.11.003

Han, S., Löhr, S. C., Abbott, A. N., Baldermann, A., Farkaš, J., McMahon, W., Milliken, K. L., Rafiei, M., Wheeler, C., & Owen, M. (2022). Earth system science applications of next-generation SEM-EDS automated mineral mapping. *Frontiers in Earth Science*, *10*. https://doi.org/10.3389/feart.2022.956912

Harriott, P., & Cheng, A. T.-Y. (1988). Kinetics of spent activated carbon regeneration. *AIChE Journal*, *34*(10), 1656–1662. https://doi.org/10.1002/aic.690341009

Heschel, W., & Klose, E. (1995). On the suitability of agricultural by-products for the manufacture of granular activated carbon. *Fuel*, *74*(12), 1786–1791. https://doi.org/10.1016/0016-2361(95)80009-7

Ibrado, A. S., & Fuerstenau, D. W. (1992). Effect of the structure of carbon adsorbents on the adsorption of gold cyanide. *Hydrometallurgy*, *30*(1), 243–256. https://doi.org/10.1016/0304-386X(92)90087-G

Ibrado, A. S., & Fuerstenau, D. W. (1995). Infrared and X-ray photoelectron spectroscopy studies on the adsorption of gold cyanide on activated carbon. *Minerals Engineering*, *8*(4), 441–458. https://doi.org/10.1016/0892-6875(95)00009-F

Ibragimova, P. I., Grebennikov, S. F., Gur'yanov, V. V., Fedyukevich, V. A., & Vorob'ev-Desyatovskii, N. V. (2014). Effect of the porous structure of activated carbon on the adsorption kinetics of gold(I) cyanide complex. *Russian Journal of Physical Chemistry A*, *88*(6), 1037–1041. https://doi.org/10.1134/S0036024414060156

Jia, Y. F., Steele, C. J., Hayward, I. P., & Thomas, K. M. (1998). Mechanism of adsorption of gold and silver species on activated carbons. *Carbon*, *36*(9), 1299–1308. https://doi.org/10.1016/S0008-6223(98)00091-8

Johnson, W. D. (1894). *Method of abstracting Gold and Silver from their solutions in Potassium Cyanides* (Patent No. 522,260). https://patents.google.com/patent/US522260

Jones, W. G., Klauber, C., & Linge, H. G. (1989). Fundamental Aspects Of Gold Cyanide Adsorption On Activated Carbon. *World Gold '89*, 278–281. https://onemine.org/documents/fundamental-aspects-of-gold-cyanide-adsorption-on-activated-carbon

Jordi, R. G., Young, B. D., & Bryson, A. W. (1991). Gold adsorption on activated carbon and the effect of suspended solids and dissolved silicon dioxide. *Taylor & Francis*, *102*(1), 127–147. https://doi.org/10.1080/00986449108910853

Juhola, A. J. (1973). *Regeneration of activated carbon*. The Water Research Association.

Kim, J., Kim, R., & Han, K. N. (2024). Advances in Hydrometallurgical Gold Recovery through Cementation, Adsorption, Ion Exchange and Solvent Extraction. *Minerals*, *14*(6), Article 6. https://doi.org/10.3390/min14060607

Klauber, C. (1991). X-ray photoelectron spectroscopic study of the adsorption mechanism of aurocyanide onto activated carbon. *Langmuir*, *7*(10), 2153–2159. https://doi.org/10.1021/la00058a030

La Brooy, S. R., Baw, A. R., Muir, D. M., Hosking, J. W., Hughes, H. C., & Parentich, A. (1986). Fouling of activated carbon by circuit organics. *Extractive Metallurgy of Gold, Volume 2*, 123–132.

Ladeira, A., Figueira, M. E. M., & Ciminelli, V. (1993). Characterization of activated carbons utilized in the gold industry: Physical and chemical properties, and kinetic study. *Minerals Engineering - MINER ENG*, *6*, 585–596. https://doi.org/10.1016/0892-6875(93)90113-2

Lagerge, S., Zajac, J., Partyka, S., & Groszek, A. J. (1999). Comparative Study on the Adsorption of Cyanide Gold Complexes onto Different Carbonaceous Samples: Measurement of the Reversibility of the Process and Assessment of the Active Surface Inferred by Flow Microcalorimetry. *Langmuir*, *15*(14), 4803–4811. https://doi.org/10.1021/la980243t

Le Roux, J. D. *, Bryson, A. W. ** &. Young B. D. **. (1991). A comparison of several kinetic models for the adsorption of gold cyanide onto activated carbon. *Journal of the Southern African Institute of Mining and Metallurgy*, *91*(3), 95–103. https://doi.org/10.10520/AJA0038223X_2031

Lee, J. H., & Yang, Y. S. (2005). Effect of HCl concentration and reaction time on the change in the crystalline state of TiO2 prepared from aqueous TiCl4 solution by precipitation. *Journal of the European Ceramic Society*, *25*(16), 3573–3578. https://doi.org/10.1016/j.jeurceramsoc.2004.09.024

Li, L., Quinlivan, P. A., & Knappe, D. R. U. (2002). Effects of activated carbon surface chemistry and pore structure on the adsorption of organic contaminants from aqueous solution. *Carbon*, *40*(12), 2085–2100. https://doi.org/10.1016/S0008-6223(02)00069-6

Lin, H. K., Hill, E. M., & Oleson, J. L. (2003). Recovering gold from carbon fines by a gold transfer process. *Mining, Metallurgy & Exploration*, *20*(1), 47–51. https://doi.org/10.1007/BF03403115

Macrae, C. M., Sparrow, G. J., & Woodcock, J. T. (1988). Gold, Calcite and Other Materials on Activated Carbons from CIP Plants. *Australasian Institute of Mining and Metallurgy Proceedings / Bulletin 293*, *Volume 6*, 121–128.

Mahmoud, M. H., Afifi, A. A. I., & Ibrahim, I. (2004). Reductive Leaching of Ilmenite Ore in Hydrochloric Acid for Preparation of Synthetic Rutile. *Hydrometallurgy*, *73*, 99–109. https://doi.org/10.1016/j.hydromet.2003.08.001

Marsden, J., & House, I. (2006). *The Chemistry of Gold Extraction* (Bd. 2). SME.

McDougall, G., Hancock, R. D., Wellington, O. L., Nicol, M. J., & Copperthwaite, R. G. (1981). *The mechanism of the adsorption of gold cyanide on activated carbon*. *1*(12), 15–17.

McDougall, G. J. (1991). The physical nature and manufacture of activated carbon. *Journal of the Southern African Institute of Mining and Metallurgy*, *91*(4), 109–120. https://doi.org/10.10520/AJA0038223X_2042

Mozammel, H. M., Masahiro, O., & Sc, B. (2002). Activated charcoal from coconut shell using ZnCl2 activation. *Biomass and Bioenergy*, *22*(5), 397–400. https://doi.org/10.1016/S0961-9534(02)00015-6

Nicol, M. J., Fleming, C. A., & Paul, R. L. (1987). The Extractive Metallurgy of Gold in South Africa. In *The Chemistry of the Extraction of Gold* (S. 831–905). South African Institute of Mining and Metallurgy,. https://researchportal.murdoch.edu.au/esploro/outputs/bookChapter/The-Extractive-Metallurgy-of-Gold-in/991005544654507891

Ofori-Sarpong, G., Tien, M., & Osseo-Asare, K. (2010). Myco-hydrometallurgy: Coal model for potential reduction of preg-robbing capacity of carbonaceous gold ores using the fungus, *Phanerochaete chrysosporium*. *Hydrometallurgy*, *102*(1), 66–72. https://doi.org/10.1016/j.hydromet.2010.02.007

Park, K.-H.-, Lee, C.-H., Ryu, S.-K., & Yang, X. (2007). Zeta-potentials of Oxygen and Nitrogen Enriched Activated Carbons for Removal of Copper Ion. *Carbon Letters*, *8*(4), 321–325.

Paulik, F., Paulik, J., & Arnold, M. (1992). Thermal decomposition of gypsum. *Thermochimica Acta*, *200*, 195–204. https://doi.org/10.1016/0040-6031(92)85115-C

Petersen, F. W., & van Deventer, J. S. J. (1991). The influence of pH, dissolved oxygen and organics on the adsorption of metal cyanides on activated carbon. *Chemical Engineering Science*, *46*(12), 3053–3065. https://doi.org/10.1016/0009-2509(91)85009-M

Pitre, D., Dagenais, V., Wilson, D., Bolduc, C., & Létourneau, Y. (2023). *NI 43-101 Technical Report, LaRonde Complex, Québec, Canada*. Agnico Eagle Mines Limited. https://minedocs.com/24/LaRonde-Complex-Agnico-TR-03242023.pdf

Pleysier, R., Dai, X., Wingate, C. J., & Jeffrey, M. I. (2008). Microtomography based identification of gold adsorption mechanisms, the measurement of activated carbon activity, and the effect of

frothers on gold adsorption. *Minerals Engineering*, *21*(6), 453–462. https://doi.org/10.1016/j.mineng.2007.12.007

Prodan, I. N., Koganovskii, A. M., & Kofanov, V. I. (1988). *Catalytic regeneration of activated carbon saturated with SAS, dye, and phenols*. Scopus.

Pszonka, J., & Schulz, B. (2022). SEM Automated Mineralogy applied for the quantification of mineral and textural sorting in submarine sediment gravity flows. *Gospodarka Surowcami Mineralnymi*, *38*, 105–131. https://doi.org/10.24425/gsm.2022.144094

Rahfeld, A., & Gutzmer, J. (2017). MLA-Based Detection of Organic Matter with Iodized Epoxy Resin—An Alternative to Carnauba. *Journal of Minerals and Materials Characterization and Engineering*, *05*, 198–208. https://doi.org/10.4236/jmmce.2017.54017

Rees, K. L., & van Deventer, J. S. J. (2000a). Preg-robbing phenomena in the cyanidation of sulphide gold ores. *Hydrometallurgy*, *58*(1), 61–80. https://doi.org/10.1016/S0304-386X(00)00131-6

Rees, K. L., & van Deventer, J. S. J. (2000b). The mechanism of enhanced gold extraction from ores in the presence of activated carbon. *Hydrometallurgy*, *58*(2), 151–167. https://doi.org/10.1016/S0304-386X(00)00130-4

Rogans, J. (2017). *Activated Carbon in Gold Recovery*. https://www.semanticscholar.org/paper/ACTIVATED-CARBON-IN-GOLD-RECOVERY-Rogans/e75fb8982d53beffb68c619e4be0ebe7036369f2

Salarirad, M. M., & Behnamfard, A. (2010). The effect of flotation reagents on cyanidation, loading capacity and sorption kinetics of gold onto activated carbon. *Hydrometallurgy*, *105*(1), 47–53. https://doi.org/10.1016/j.hydromet.2010.07.009

Salarirad, M. M., & Behnamfard, A. (2011). Fouling effect of different flotation and dewatering reagents on activated carbon and sorption kinetics of gold. *Hydrometallurgy*, *109*(1), 23–28. https://doi.org/10.1016/j.hydromet.2011.05.002

Saleem, J., Moghal, Z. K. B., Tahir, F., Al-Ansari, T., & McKay, G. (2025). Environmental Impacts and Adsorption Isotherms of Coconut Shell Activated Carbon: Effect of Acid Activation, Water, and Fuel. *C*, *11*(1), Article 1. https://doi.org/10.3390/c11010022

Salunkhe, S., Mohod, A., Khandetod, Y., Dhande, K., & Aware, S. (2024). Steam activated carbon production from coconut shell charcoal using open top gasifier as heat source. *International Journal of Agriculture and Food Science*, *6*(1), 20–26. https://doi.org/10.33545/2664844X.2024.v6.i1a.161

Schulz, B., Sandmann, D., & Gilbricht, S. (2020). SEM-Based Automated Mineralogy and Its Application in Geo- and Material Sciences. *Minerals*, *10*(11), Article 11. https://doi.org/10.3390/min10111004

Sidhu, P., Gilkes, R., CORNELL, R., Posner, M., & QUIRK, J. (1981). Dissolution of Iron Oxides and Oxyhydroxides in Hydrochloric and Perchloric Acids. *Clays and Clay Minerals - CLAYS CLAY MINER*, *29*, 269–276. https://doi.org/10.1346/CCMN.1981.0290404

Šimková, L. (2018). Influence of precipitation conditions on the synthesis of hydroxyapatite. *Ceramics - Silikaty*, *62*, 1–9. https://doi.org/10.13168/cs.2018.0019

Smith, I., Hinchcliffe, W., Hosking, J. W., & Muir, D. M. (1984). Fouling studies on C.I.P carbons and prospects for gold recovery using ion exchange resins. *Minerals Research Institute of WA*. https://www.mriwa.wa.gov.au/research-projects/project-portfolio/fouling-studies-on-c-i-p-carbons-and-prospects-for-gold-recovery-using-ion-exchange-resins/

Souza, C., Majuste, D., Dantas, M. S. S., & Ciminelli, V. S. T. (2014). Selective adsorption of gold over copper cyanocomplexes on activated carbon. *Hydrometallurgy*, *147–148*, 188–195. https://doi.org/10.1016/j.hydromet.2014.05.017

Stange, W. (1999). The process design of gold leaching and carbon-in-pulp circuits. *Journal of the Southern African Institute of Mining and Metallurgy*, *99*(1), 13–25. https://doi.org/10.10520/AJA0038223X_2609

*Tailings and Mine Waste: Bd. Proceedings of the Ninth International Conference on Tailings and Mine Waste, Fort Collins, Colorado, USA, 27-30 January 2002*. (2002). A.A. Balkema.

Trading Economics. (2025, Februar 17). *Gold—Price—Chart—Historical Data—News*. https://tradingeconomics.com/commodity/gold

Tsuchida, N., & Muir, D. M. (1986). Studies on role of oxygen in the adsorption of Au(CN)2−and Ag(CN)2−onto activated carbon. *Metallurgical Transactions B*, *17*(3), 529–533. https://doi.org/10.1007/BF02670219

Tu, Y., Han, P., Wei, L., Zhang, X., Yu, B., Qian, P., & Ye, S. (2019). Removal of cyanide adsorbed on pyrite by H2O2 oxidation under alkaline conditions. *Journal of Environmental Sciences*, *78*, 287–292. https://doi.org/10.1016/j.jes.2018.10.013

Unugul, T., & Nigiz, F. U. (2020). Preparation and Characterization an Active Carbon Adsorbent from Waste Mandarin Peel and Determination of Adsorption Behavior on Removal of Synthetic Dye Solutions. *Water, Air, & Soil Pollution*, *231*(11), 538. https://doi.org/10.1007/s11270-020-04903-5

Urbanic, J. E., Jula, R. J., & Faulkner, W. D. (1985). Regeneration of activated carbon used for recovery of gold. *Mining, Metallurgy & Exploration*, *2*(4), 193–198. https://doi.org/10.1007/BF03402618

van Deventer, J. S. J., & van der Merwe, P. F. (1993). The reversibility of adsorption of gold cyanide on activated carbon. *Metallurgical Transactions B*, *24*(3), 433–440. https://doi.org/10.1007/BF02666425

van Deventer, J. S. J., & van der Merwe, P. F. (1994). The mechanism of elution of gold cyanide from activated carbon. *Metallurgical and Materials Transactions B*, *25*(6), 829–838. https://doi.org/10.1007/BF02662765

van Vliet, B. M. (1982, September 6). *Comparative Efficacy of Extractive and Thermal Regeneration of Activated Carbon*. 14th IWSA International Conference, Zürich, Switzerland.

van Vliet, B. M. (1991). The regeneration of activated carbon. *Journal of the Southern African Institute of Mining and Metallurgy*, *91*(5), 159–167. https://doi.org/10.10520/AJA0038223X_2021

Vegter, N., Sandenbergh, R., & Botha, A. (1997). Concentration profiles of gold inside activated carbon during adsorption. *Journal of The South African Institute of Mining and Metallurgy*, *97*, 299–312.

Wang, D., Root, R. A., & Chorover, J. (2021). Biochar-templated surface precipitation and inner-sphere complexation effectively removes arsenic from acid mine drainage. *Environmental Science and Pollution Research*, *28*(33), 45519–45533. https://doi.org/10.1007/s11356-021-13869-8

Wang, L., & Lu, G. Q. (1998). Effects of acidic treatments on the pore and surface properties of Ni catalyst supported on activated carbon. *Carbon*, *36*(3), 283–292. https://doi.org/10.1016/S0008-6223(97)00187-5

World Gold Council. (2024, Juni 25). *Global mine production by country*. World Gold Council. https://www.gold.org/goldhub/data/gold-production-by-country

Xia, J., Marthi, R., Twinney, J., & Ghahreman, A. (2022). A review on adsorption mechanism of gold cyanide complex onto activation carbon. *Journal of Industrial and Engineering Chemistry*, *111*, 35–42. https://doi.org/10.1016/j.jiec.2022.04.014

Yamak, Z. F., Somppi, M., & Drozd, M. (2019). Economic evaluation of activated carbon for gold milling circuits. *CIM Journal*, *10*, 103–113. https://doi.org/10.15834/cimj.2019.5

Yin, C.-Y., Ng, M.-F., Saunders, M., Goh, B.-M., Senanayake, G., Sherwood, A., & Hampton, M. (2014). New Insights into the Adsorption of Aurocyanide Ion on Activated Carbon Surface: Electron Microscopy Analysis and Computational Studies Using Fullerene-like Models. *Langmuir*, *30*(26), 7703–7709. https://doi.org/10.1021/la501191h

Yin, X., Opara, A., Miller, J. D., & Du, H. (2011). Molecular dynamics simulations of metal–cyanide complexes: Fundamental considerations in gold hydrometallurgy. *Hydrometallurgy*, *106*(1), 64–70. https://doi.org/10.1016/j.hydromet.2010.12.004

# Appendix A

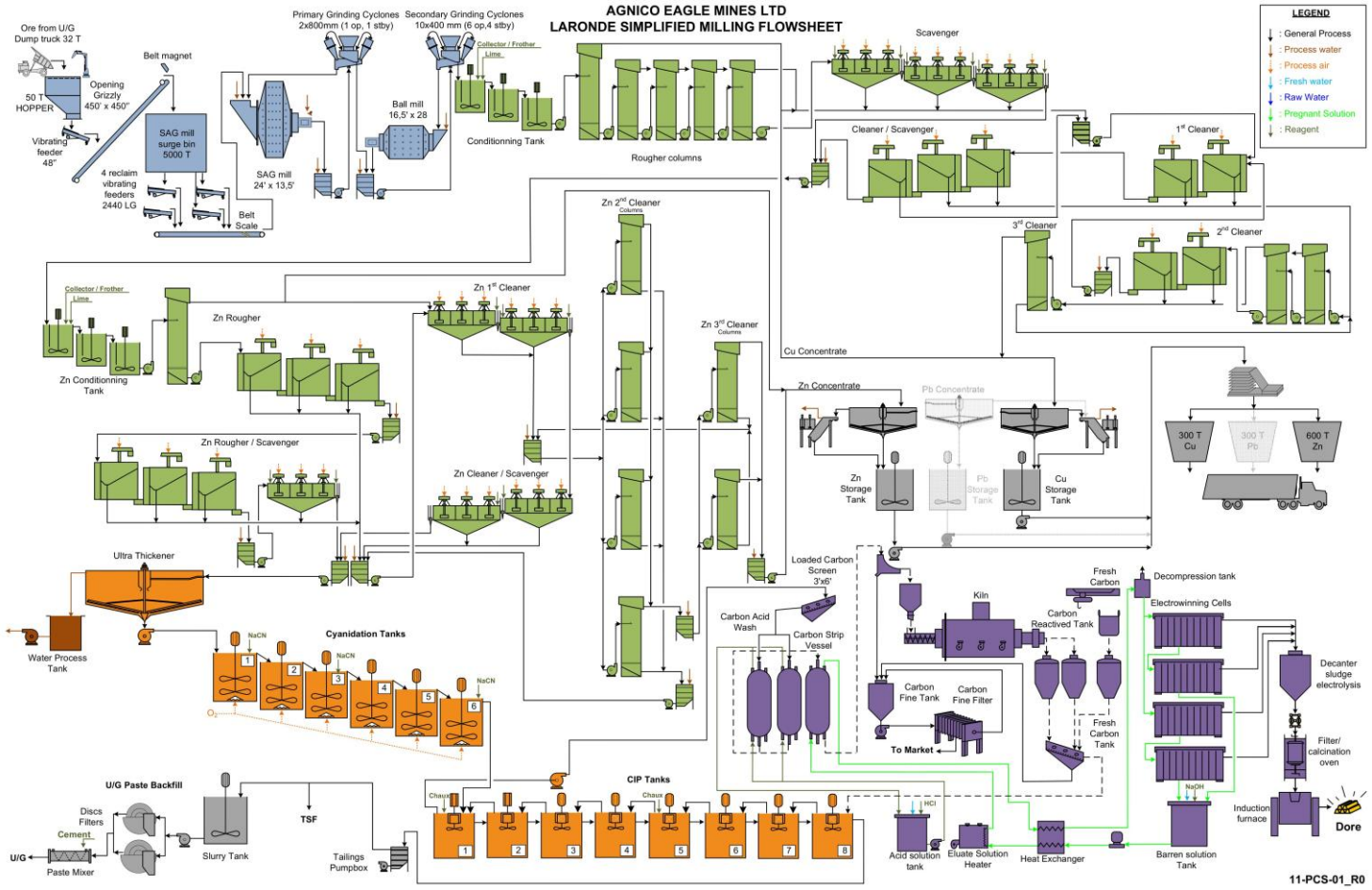


Figure 30. Simplified flowsheet of the LaRonde mill. Source: Pitre et al. (2023).

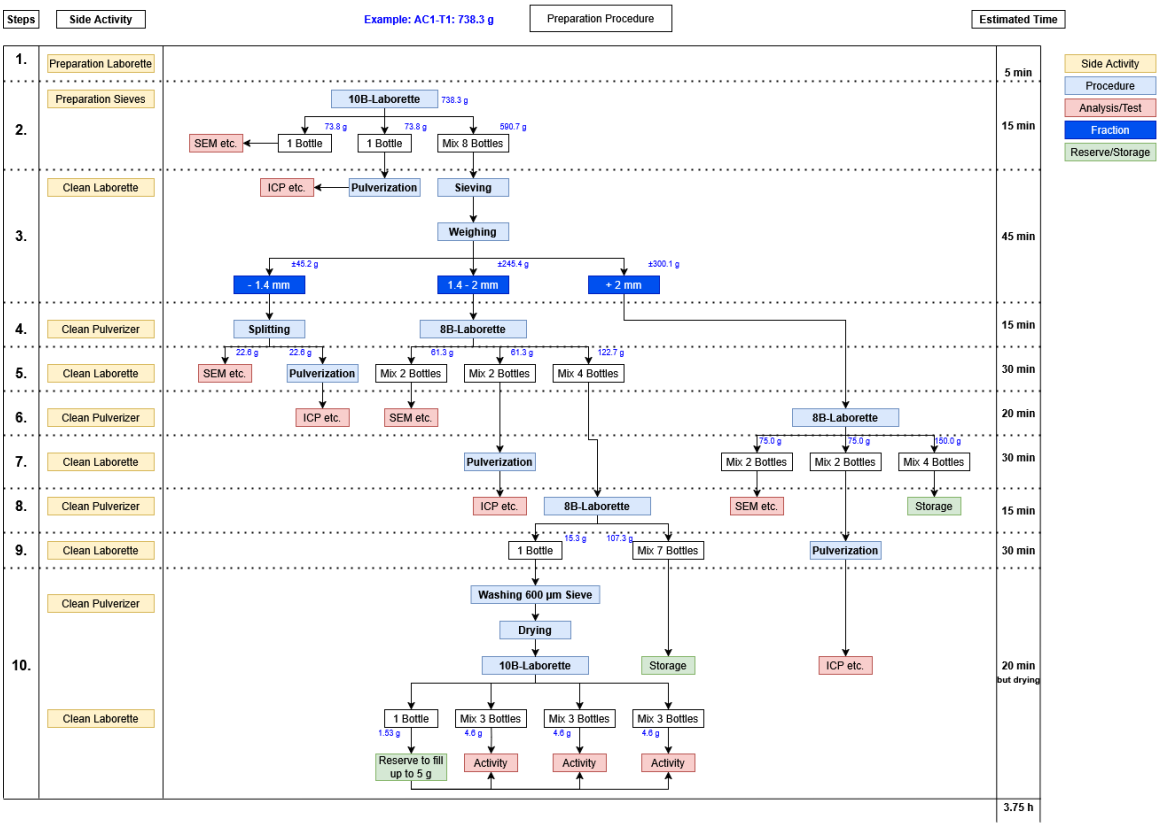


Figure 31. Sample preparation procedure with estimated weights for the sample AC1-T1.

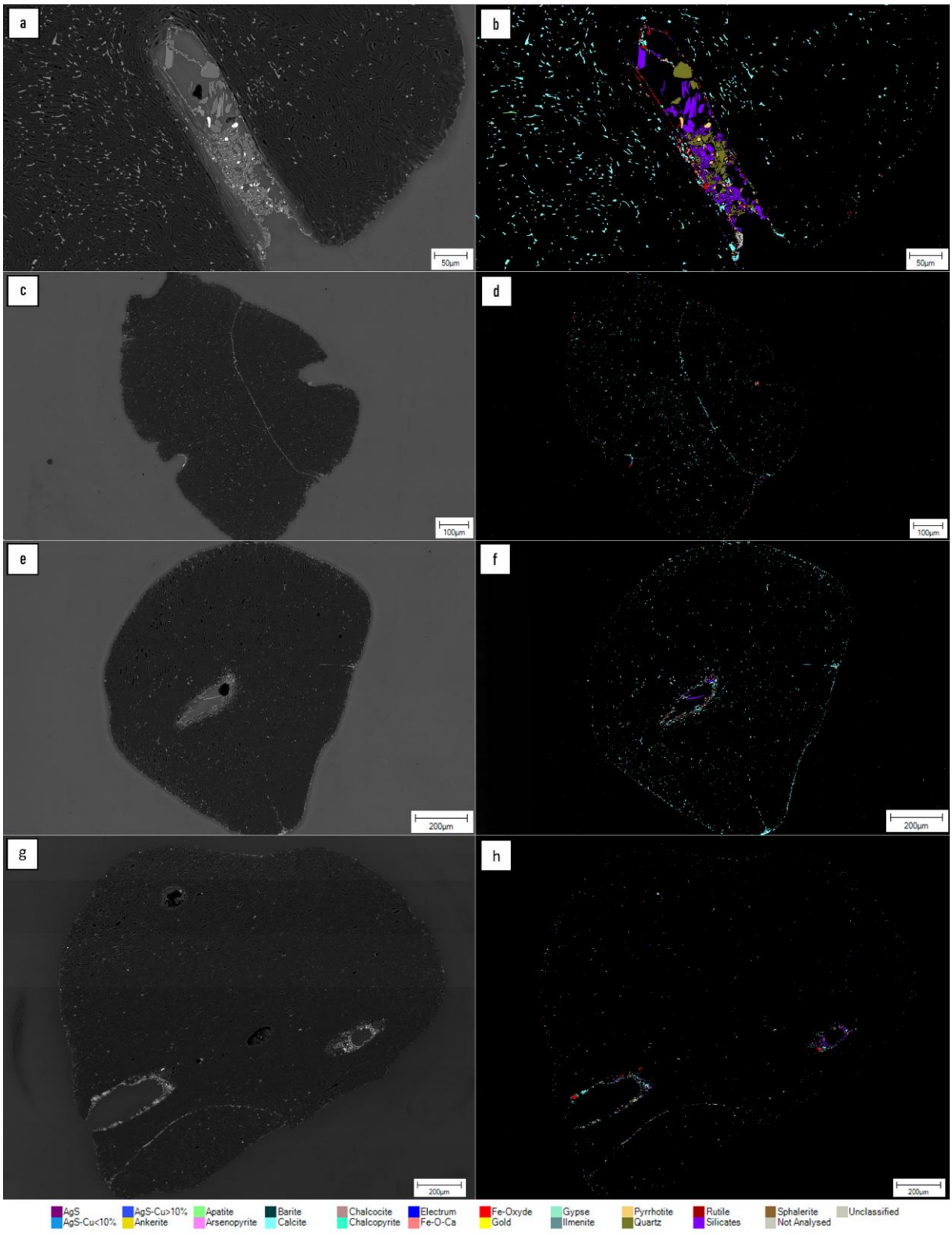


Figure 32. Backscattered electron and false-colour mineral classification images of different inorganic fouling types on carbon particles from sample AC1-T1, showing calcite: (a-b) as finely-crystalline grains filling out macropores type A (50 nm – 30 µm), (c-d) filling out cracks of carbon particles, (e-f) coating the external surface of carbon particles and (g-h) occluding other minerals particles.

# Appendix B

Table 7. Elemental composition of carbon samples obtained using inductively coupled plasma spectroscopy. Values represent the average content of duplicate measurements.

| Sample | Ag $g \cdot t^{-1}$ | Cu % | Zn % | Pb % | Fe % | Ni % | Co % | As % | Sb % | Ca % | Mg % | Al % | Ba % | Be % | Bi % | Cd % | Cr % |
|---|---|---|---|---|---|---|---|---|---|---|---|---|---|---|---|---|---|
| AC1-T1-F1-P | 3037.4 | 0.047 | 0.054 | 0.003 | 0.222 | 0.013 | < 0.0004 | 0.001 | 0.0002 | 1.72 | 0.038 | 0.037 | 0.001 | < 0.001 | < 0.003 | 0.001 | 0.010 |
| AC1-T1-F2-P | 2731.6 | 0.044 | 0.062 | 0.004 | 0.882 | 0.012 | < 0.0004 | 0.002 | 0.0004 | 2.35 | 0.092 | 0.156 | 0.002 | < 0.001 | < 0.003 | 0.001 | 0.043 |
| AC1-T1-F3-P | 2983.5 | 0.046 | 0.054 | 0.002 | 0.214 | 0.012 | < 0.0004 | 0.001 | < 0.0001 | 1.68 | 0.032 | 0.024 | < 0.001 | < 0.001 | < 0.003 | 0.001 | 0.015 |
| AC1-T1-F4-P | 2892.6 | 0.048 | 0.045 | 0.002 | 0.149 | 0.017 | < 0.0004 | 0.001 | < 0.0001 | 1.58 | 0.030 | 0.025 | < 0.001 | < 0.001 | < 0.003 | 0.001 | 0.003 |
| AC1-T3-F1-P | 2656.2 | 0.054 | 0.056 | 0.003 | 0.196 | 0.015 | < 0.0004 | 0.001 | < 0.0001 | 1.55 | 0.031 | 0.027 | < 0.001 | < 0.001 | < 0.003 | 0.001 | 0.009 |
| AC1-T3-F2-P | 2461.8 | 0.046 | 0.054 | 0.003 | 0.402 | 0.010 | < 0.0004 | 0.002 | 0.0003 | 1.72 | 0.054 | 0.079 | 0.001 | < 0.001 | < 0.003 | 0.001 | 0.017 |
| AC1-T3-F3-P | 2612.3 | 0.051 | 0.056 | 0.002 | 0.186 | 0.013 | < 0.0004 | 0.001 | 0.0003 | 1.59 | 0.028 | 0.022 | < 0.001 | < 0.001 | < 0.003 | 0.001 | 0.008 |
| AC1-T3-F4-P | 2747.0 | 0.061 | 0.058 | 0.002 | 0.209 | 0.021 | < 0.0004 | 0.001 | < 0.0001 | 1.46 | 0.030 | 0.024 | < 0.001 | < 0.001 | < 0.003 | 0.001 | 0.009 |
| AC1-T5-F1-P | 2150.2 | 0.051 | 0.057 | 0.003 | 0.251 | 0.014 | < 0.0004 | 0.002 | 0.0003 | 1.79 | 0.040 | 0.047 | 0.001 | < 0.001 | < 0.003 | 0.001 | 0.008 |
| AC1-T5-F2-P | 2187.3 | 0.043 | 0.054 | 0.003 | 0.366 | 0.011 | < 0.0004 | 0.003 | 0.0004 | 2.43 | 0.073 | 0.101 | 0.001 | < 0.001 | < 0.003 | 0.001 | 0.013 |
| AC1-T5-F3-P | 2106.3 | 0.049 | 0.054 | 0.003 | 0.176 | 0.011 | < 0.0004 | 0.001 | < 0.0001 | 1.55 | 0.029 | 0.025 | < 0.001 | < 0.001 | < 0.003 | 0.001 | 0.007 |
| AC1-T5-F4-P | 2152.8 | 0.061 | 0.059 | 0.003 | 0.177 | 0.020 | < 0.0004 | 0.001 | < 0.0001 | 1.48 | 0.028 | 0.027 | < 0.001 | < 0.001 | < 0.003 | 0.002 | 0.009 |
| AC1-T7-F1-P | 1454.1 | 0.071 | 0.066 | 0.002 | 0.211 | 0.016 | < 0.0004 | 0.001 | < 0.0001 | 1.54 | 0.030 | 0.027 | < 0.001 | < 0.001 | < 0.003 | 0.002 | 0.012 |
| AC1-T7-F2-P | 1679.4 | 0.057 | 0.062 | 0.003 | 0.276 | 0.012 | < 0.0004 | 0.002 | 0.0003 | 1.91 | 0.043 | 0.054 | 0.001 | < 0.001 | < 0.003 | 0.001 | 0.012 |
| AC1-T7-F3-P | 1407.3 | 0.069 | 0.066 | 0.002 | 0.213 | 0.013 | < 0.0004 | 0.001 | < 0.0001 | 1.46 | 0.024 | 0.019 | < 0.001 | < 0.001 | < 0.003 | 0.001 | 0.012 |
| AC1-T7-F4-P | 1377.0 | 0.080 | 0.069 | 0.003 | 0.204 | 0.020 | < 0.0004 | 0.001 | 0.0002 | 1.41 | 0.028 | 0.021 | < 0.001 | < 0.001 | < 0.003 | 0.002 | 0.008 |
| AC1-T8-F1-P | 1003.3 | 0.063 | 0.065 | 0.002 | 0.217 | 0.011 | < 0.0004 | 0.001 | < 0.0001 | 1.41 | 0.026 | 0.020 | < 0.001 | < 0.001 | < 0.003 | 0.001 | 0.014 |
| AC1-T8-F2-P | 934.6 | 0.063 | 0.074 | 0.003 | 0.743 | 0.011 | < 0.0004 | 0.001 | 0.0003 | 1.40 | 0.038 | 0.046 | 0.001 | < 0.001 | < 0.003 | 0.002 | 0.057 |
| AC1-T8-F3-P | 1022.1 | 0.060 | 0.064 | 0.002 | 0.261 | 0.009 | < 0.0004 | 0.001 | < 0.0001 | 1.40 | 0.025 | 0.017 | < 0.001 | < 0.001 | < 0.003 | 0.001 | 0.012 |
| AC1-T8-F4-P | 1030.8 | 0.067 | 0.066 | 0.002 | 0.206 | 0.013 | < 0.0004 | 0.001 | < 0.0001 | 1.40 | 0.026 | 0.020 | < 0.001 | < 0.001 | < 0.003 | 0.001 | 0.015 |
| AC2-F1-P | 3167.5 | 0.053 | 0.061 | 0.002 | 0.208 | 0.015 | < 0.0004 | 0.002 | < 0.0001 | 1.52 | 0.026 | 0.033 | < 0.001 | < 0.001 | < 0.003 | 0.001 | 0.005 |
| AC2-F2-P | 2876.9 | 0.044 | 0.064 | 0.003 | 0.479 | 0.012 | < 0.0004 | 0.002 | < 0.0001 | 1.93 | 0.058 | 0.093 | 0.001 | < 0.001 | < 0.003 | 0.001 | 0.011 |
| AC2-F3-P | 2974.5 | 0.033 | 0.050 | 0.002 | 0.217 | 0.008 | < 0.0004 | 0.001 | 0.0007 | 1.46 | 0.021 | 0.021 | 0.001 | < 0.001 | < 0.003 | 0.001 | 0.013 |
| AC2-F4-P | 3151.4 | 0.047 | 0.050 | 0.002 | 0.23 | 0.014 | < 0.0004 | 0.001 | < 0.0001 | 1.37 | 0.022 | 0.020 | < 0.001 | < 0.001 | < 0.003 | 0.001 | 0.016 |
| AC3-F1-P | 1063.1 | 0.016 | 0.048 | 0.004 | 0.592 | 0.007 | < 0.0004 | 0.001 | 0.0002 | 1.56 | 0.046 | 0.027 | < 0.001 | < 0.001 | < 0.003 | 0.001 | 0.048 |
| AC3-F2-P | 1100.4 | 0.017 | 0.061 | 0.004 | 1.11 | 0.004 | < 0.0004 | 0.001 | < 0.0001 | 1.98 | 0.079 | 0.069 | 0.001 | < 0.001 | < 0.003 | 0.001 | 0.032 |
| AC3-F3-P | 1105.6 | 0.014 | 0.048 | 0.003 | 0.283 | 0.003 | < 0.0004 | 0.001 | < 0.0001 | 1.49 | 0.041 | 0.022 | < 0.001 | < 0.001 | < 0.003 | 0.001 | 0.008 |
| AC3-F4-P | 1138.8 | 0.017 | 0.043 | 0.003 | 0.393 | 0.003 | < 0.0004 | 0.001 | < 0.0001 | 1.41 | 0.038 | 0.021 | < 0.001 | < 0.001 | < 0.003 | 0.001 | 0.021 |
| AC4-F1-P | 900.3 | 0.006 | 0.048 | 0.001 | 0.187 | 0.002 | < 0.0004 | 0.001 | < 0.0001 | 1.48 | 0.035 | 0.022 | < 0.001 | < 0.001 | < 0.003 | < 0.0008 | 0.007 |
| AC4-F2-P | 971.2 | 0.007 | 0.065 | 0.003 | 0.667 | 0.004 | < 0.0004 | 0.001 | 0.0001 | 1.62 | 0.069 | 0.048 | 0.001 | < 0.001 | < 0.003 | 0.001 | 0.014 |
| AC4-F3-P | 951.5 | 0.007 | 0.051 | 0.002 | 0.222 | 0.002 | < 0.0004 | < 0.0004 | 0.0002 | 1.37 | 0.030 | 0.017 | < 0.001 | < 0.001 | < 0.003 | 0.001 | 0.013 |
| AC4-F4-P | 898.1 | 0.007 | 0.045 | 0.001 | 0.177 | 0.002 | < 0.0004 | 0.001 | < 0.0001 | 1.37 | 0.032 | 0.018 | < 0.001 | < 0.001 | < 0.003 | < 0.0008 | 0.007 |
| AC5-F1-P | < 1.0 | 0.002 | < 0.001 | < 0.001 | 0.255 | 0.001 | < 0.0004 | < 0.0004 | 0.0003 | 0.04 | 0.038 | 0.012 | < 0.001 | < 0.001 | < 0.003 | < 0.0008 | 0.021 |

Table 8. Elemental composition of carbon samples obtained using inductively coupled plasma spectroscopy. Values represent the average content of duplicate measurements.

| Sample | K % | Mn % | Mo % | Na % | P % | S % | Sc % | Se ppm | Sn % | Sr % | Te % | Ti % | Tl % | V % | Y % | Zr % |
|---|---|---|---|---|---|---|---|---|---|---|---|---|---|---|---|---|
| AC1-T1-F1-P | 0.011 | 0.002 | < 0.001 | 0.364 | 0.112 | 0.508 | < 0.003 | 62.5 | 0.005 | 0.004 | < 0.0008 | < 0.003 | < 0.003 | < 0.003 | < 0.003 | < 0.003 |
| AC1-T1-F2-P | 0.019 | 0.006 | 0.002 | 0.498 | 0.098 | 0.964 | < 0.003 | 61.9 | 0.017 | 0.005 | 0.0015 | 0.007 | < 0.003 | < 0.003 | < 0.003 | < 0.003 |
| AC1-T1-F3-P | 0.011 | 0.001 | < 0.001 | 0.438 | 0.105 | 0.522 | < 0.003 | 59.4 | 0.006 | 0.004 | < 0.0008 | < 0.003 | < 0.003 | < 0.003 | < 0.003 | < 0.003 |
| AC1-T1-F4-P | 0.008 | 0.001 | < 0.001 | 0.269 | 0.122 | 0.378 | < 0.003 | 61.6 | < 0.003 | 0.003 | < 0.0008 | < 0.003 | < 0.003 | < 0.003 | < 0.003 | < 0.003 |
| AC1-T3-F1-P | 0.009 | 0.001 | < 0.001 | 0.366 | 0.113 | 0.512 | < 0.003 | 57.9 | 0.004 | 0.003 | < 0.0008 | < 0.003 | < 0.003 | < 0.003 | < 0.003 | < 0.003 |
| AC1-T3-F2-P | 0.015 | 0.003 | < 0.001 | 0.502 | 0.091 | 0.690 | < 0.003 | 55.4 | 0.007 | 0.004 | 0.0008 | 0.005 | < 0.003 | < 0.003 | < 0.003 | < 0.003 |
| AC1-T3-F3-P | 0.010 | 0.001 | < 0.001 | 0.431 | 0.107 | 0.541 | < 0.003 | 56.5 | 0.004 | 0.003 | < 0.0008 | < 0.003 | < 0.003 | < 0.003 | < 0.003 | < 0.003 |
| AC1-T3-F4-P | 0.008 | 0.001 | < 0.001 | 0.266 | 0.122 | 0.450 | < 0.003 | 56.9 | 0.004 | 0.003 | < 0.0008 | < 0.003 | < 0.003 | < 0.003 | < 0.003 | < 0.003 |
| AC1-T5-F1-P | 0.011 | 0.002 | < 0.001 | 0.418 | 0.106 | 0.584 | < 0.003 | 54.4 | 0.004 | 0.004 | 0.0008 | 0.003 | < 0.003 | < 0.003 | < 0.003 | < 0.003 |
| AC1-T5-F2-P | 0.015 | 0.004 | < 0.001 | 0.510 | 0.100 | 0.723 | < 0.003 | 68.8 | 0.005 | 0.005 | 0.0017 | 0.005 | < 0.003 | < 0.003 | < 0.003 | < 0.003 |
| AC1-T5-F3-P | 0.010 | 0.001 | < 0.001 | 0.453 | 0.104 | 0.543 | < 0.003 | 48.0 | 0.003 | 0.003 | < 0.0008 | < 0.003 | < 0.003 | < 0.003 | < 0.003 | < 0.003 |
| AC1-T5-F4-P | 0.007 | 0.001 | < 0.001 | 0.303 | 0.120 | 0.489 | < 0.003 | 45.0 | 0.004 | 0.003 | < 0.0008 | < 0.003 | < 0.003 | < 0.003 | < 0.003 | < 0.003 |
| AC1-T7-F1-P | 0.009 | 0.001 | < 0.001 | 0.412 | 0.109 | 0.607 | < 0.003 | 46.8 | 0.005 | 0.003 | < 0.0008 | < 0.003 | < 0.003 | < 0.003 | < 0.003 | < 0.003 |
| AC1-T7-F2-P | 0.013 | 0.002 | < 0.001 | 0.534 | 0.100 | 0.753 | < 0.003 | 56.7 | 0.004 | 0.004 | 0.0011 | 0.004 | < 0.003 | < 0.003 | < 0.003 | < 0.003 |
| AC1-T7-F3-P | 0.009 | 0.001 | < 0.001 | 0.465 | 0.104 | 0.634 | < 0.003 | 37.5 | 0.005 | 0.003 | < 0.0008 | < 0.003 | < 0.003 | < 0.003 | < 0.003 | < 0.003 |
| AC1-T7-F4-P | 0.007 | 0.001 | < 0.001 | 0.300 | 0.118 | 0.533 | < 0.003 | 36.9 | 0.003 | 0.003 | < 0.0008 | < 0.003 | < 0.003 | < 0.003 | < 0.003 | < 0.003 |
| AC1-T8-F1-P | 0.007 | 0.001 | < 0.001 | 0.424 | 0.105 | 0.575 | < 0.003 | 34.0 | 0.006 | 0.003 | < 0.0008 | < 0.003 | < 0.003 | < 0.003 | < 0.003 | < 0.003 |
| AC1-T8-F2-P | 0.009 | 0.004 | 0.002 | 0.573 | 0.092 | 0.789 | < 0.003 | 35.1 | 0.023 | 0.003 | < 0.0008 | 0.004 | < 0.003 | < 0.003 | < 0.003 | < 0.003 |
| AC1-T8-F3-P | 0.007 | 0.002 | < 0.001 | 0.506 | 0.098 | 0.612 | < 0.003 | 33.6 | 0.005 | 0.003 | < 0.0008 | 0.003 | < 0.003 | < 0.003 | < 0.003 | < 0.003 |
| AC1-T8-F4-P | 0.006 | 0.001 | < 0.001 | 0.330 | 0.113 | 0.519 | < 0.003 | 34.8 | 0.006 | 0.003 | < 0.0008 | < 0.003 | < 0.003 | < 0.003 | < 0.003 | < 0.003 |
| AC2-F1-P | 0.008 | 0.002 | < 0.001 | 0.368 | 0.118 | 0.608 | < 0.003 | 67.5 | < 0.003 | 0.003 | < 0.0008 | < 0.003 | < 0.003 | < 0.003 | < 0.003 | < 0.003 |
| AC2-F2-P | 0.012 | 0.004 | < 0.001 | 0.456 | 0.112 | 0.838 | < 0.003 | 72.0 | 0.005 | 0.004 | 0.0016 | 0.006 | < 0.003 | < 0.003 | < 0.003 | < 0.003 |
| AC2-F3-P | 0.007 | 0.001 | < 0.001 | 0.353 | 0.107 | 0.419 | < 0.003 | 52.1 | 0.006 | 0.003 | 0.0008 | < 0.003 | < 0.003 | < 0.003 | < 0.003 | < 0.003 |
| AC2-F4-P | 0.007 | 0.001 | < 0.001 | 0.289 | 0.117 | 0.385 | < 0.003 | 63.2 | 0.007 | 0.003 | < 0.0008 | < 0.003 | < 0.003 | < 0.003 | < 0.003 | < 0.003 |
| AC3-F1-P | 0.010 | 0.003 | 0.006 | 0.935 | 0.070 | 0.434 | < 0.003 | 30.8 | 0.019 | 0.004 | < 0.0008 | 0.003 | < 0.003 | < 0.003 | < 0.003 | < 0.003 |
| AC3-F2-P | 0.012 | 0.006 | 0.001 | 0.956 | 0.067 | 0.628 | < 0.003 | 35.0 | 0.012 | 0.005 | < 0.0008 | 0.006 | < 0.003 | < 0.003 | < 0.003 | < 0.003 |
| AC3-F3-P | 0.009 | 0.002 | < 0.001 | 0.953 | 0.068 | 0.418 | < 0.003 | 31.1 | 0.004 | 0.004 | < 0.0008 | 0.003 | < 0.003 | < 0.003 | < 0.003 | < 0.003 |
| AC3-F4-P | 0.010 | 0.002 | < 0.001 | 0.881 | 0.070 | 0.374 | < 0.003 | 28.2 | 0.009 | 0.004 | < 0.0008 | < 0.003 | < 0.003 | < 0.003 | < 0.003 | < 0.003 |
| AC4-F1-P | 0.008 | 0.001 | < 0.001 | 0.656 | 0.098 | 0.326 | < 0.003 | 26.2 | 0.003 | 0.003 | < 0.0008 | < 0.003 | < 0.003 | < 0.003 | < 0.003 | < 0.003 |
| AC4-F2-P | 0.010 | 0.005 | < 0.001 | 0.795 | 0.087 | 0.424 | < 0.003 | 32.1 | 0.006 | 0.004 | < 0.0008 | 0.006 | < 0.003 | < 0.003 | < 0.003 | < 0.003 |
| AC4-F3-P | 0.008 | 0.002 | < 0.001 | 0.701 | 0.093 | 0.344 | < 0.003 | 30.2 | 0.006 | 0.003 | < 0.0008 | 0.003 | < 0.003 | < 0.003 | < 0.003 | < 0.003 |
| AC4-F4-P | 0.007 | 0.001 | < 0.001 | 0.552 | 0.105 | 0.274 | < 0.003 | 28.5 | 0.003 | 0.003 | < 0.0008 | < 0.003 | < 0.003 | < 0.003 | < 0.003 | < 0.003 |
| AC5-F1-P | 0.021 | 0.002 | < 0.001 | 0.018 | 0.022 | 0.010 | < 0.003 | < 0.4 | 0.008 | < 0.003 | < 0.0008 | < 0.003 | < 0.003 | < 0.003 | < 0.003 | < 0.003 |

Table 9. Elemental contents of all samples determined by fire assay for Au and by C-S analyzer for total S. Au values represent the average content of triplicate measurements.

| Sample | Au $g \cdot t^{-1}$ | Total S % |
|---|---|---|
| AC1-T1-F1-P | 1310.0 | 0.56 |
| AC1-T1-F2-P | 1480.3 | 1.10 |
| AC1-T1-F3-P | 1279.2 | 0.55 |
| AC1-T1-F4-P | 1294.8 | 0.59 |
| AC1-T3-F1-P | 677.5 | 0.51 |
| AC1-T3-F2-P | 766.2 | 0.84 |
| AC1-T3-F3-P | 661.3 | 0.56 |
| AC1-T3-F4-P | 678.4 | 0.55 |
| AC1-T5-F1-P | 411.1 | 0.60 |
| AC1-T5-F2-P | 679.1 | 0.80 |
| AC1-T5-F3-P | 330.9 | 0.60 |
| AC1-T5-F4-P | 288.8 | 0.47 |
| AC1-T7-F1-P | 109.2 | 0.61 |
| AC1-T7-F2-P | 258.1 | 0.75 |
| AC1-T7-F3-P | 78.6 | 0.61 |
| AC1-T7-F4-P | 72.1 | 0.49 |
| AC1-T8-F1-P | 38.4 | 0.58 |
| AC1-T8-F2-P | 36.9 | 0.73 |
| AC1-T8-F3-P | 36.0 | 0.56 |
| AC1-T8-F4-P | 43.0 | 0.49 |
| AC2-F1-P | 1364.2 | 0.64 |
| AC2-F2-P | 1568.2 | 0.88 |
| AC2-F3-P | 1323.1 | 0.61 |
| AC2-F4-P | 1320.4 | 0.49 |
| AC3-F1-P | 64.2 | 0.31 |
| AC3-F2-P | 63.3 | 0.71 |
| AC3-F3-P | 68.7 | 0.41 |
| AC3-F4-P | 77.6 | 0.20 |
| AC4-F1-P | 38.2 | 0.57 |
| AC4-F2-P | 29.0 | 0.53 |
| AC4-F3-P | 37.3 | 0.55 |
| AC4-F4-P | 45.6 | 0.42 |
| AC5-F1-P | - | < 0.03 |

Table 10. Results of the chemical analysis obtained for the process water using inductively coupled plasma optical emission spectroscopy.

| Element/Species | Concentration ($mg \cdot l^{-1}$) |
|---|---|
| Na | 3500.00 |
| S | 1640.00 |
| Cl | 299.30 |
| SCN | 208.55 |
| Zn | 93.30 |
| S2O3 | 37.65 |
| K | 36.00 |
| NO3-N | 17.60 |
| NO2 | 5.07 |
| Cu | 4.02 |
| Se | 3.70 |
| Ca | 1.66 |
| P | 1.43 |
| Fe | 0.88 |
| As | 0.81 |
| Ni | 0.36 |
| Al | 0.24 |
| Mo | 0.16 |
| Mg | 0.11 |
| Ag | 0.05 |
| V | 0.05 |
| Sr | 0.02 |
| Cd | 0.01 |
| Mn | 0.01 |